Czech Technical University in Prague

Faculty of Electrical Engineering

HABILITATION THESIS

Spectroscopy of the optical absorption edge of solar cell materials

September 2017   Jakub Holovský

Abstract

The focus of this thesis is relatively narrowly defined as spectroscopy of the optical absorption edge of the actual or potential photovoltaic materials. This includes the spectroscopy methods and interpretation of results, the photovoltaic materials and their technological parameters and also the potential of certain photovoltaic technologies as a renewable source of energy.

The materials presented here are either absorbers: amorphous silicon (a-Si:H), microcrystalline silicon, organo-metalhalide perovskites ($CH_3NH_3PbI_3$) or materials for transparent electrodes: graphene, amorphous InZnO and amorphous ZnSnO. The physical effects studied are related to material preparation methods, ageing, exposure to light, and annealing.

The methods employed here for the absorption spectroscopy are photothermal deflection spectroscopy and photocurrent spectroscopy. The two methods are briefly explained and compared. Two main issues related to correct interpretation of these measurements are discussed: effect of surface states and the effects of light scattering.

The absorption spectrum in sub-bandgap region is measured to obtain mainly the slope of the absorption edge parametrized by Urbach energy. It is shown here, how theoretically and practically this parameter correlates with the maximum attainable efficiency of solar cell – if the material is used as absorber. If the material is used as transparent electrode, correlation with conductivity is found.

The effect of cost evolution in the photovoltaic industry is discussed with the consequence on the efficiency as a most critical parameter dictating the cost of energy. The competitiveness of the solar energy is reviewed for different levels of autonomy.

Keywords: *solar cells, photovoltaics, photocurrent spectroscopy, photothermal spectroscopy, Urbach energy, sub-bandgap absorption*

Contents

1 Introduction

1.1 Motivation

Looking at the Earth as a closed system, there are not as many sources of energy independent of the Sun. Only nuclear, geothermal and tidal are those few exceptions. Fossil fuels on the other hand such as coal or oil and gas represent stocks of sunlight energy transformed and accumulated millions of years in past. Biomass, hydro and wind power are renewable sources, but also represent mainly accumulated sunlight. Direct utilization of sunlight and its transformation into electricity by photovoltaics is very elegant and popular renewable energy source that is closely related to the subject of this thesis. It is fair to admit here that using sunlight had always came together with a kind of accumulation, because sunlight is unstable, intermittent source and therefore also photovoltaics should be also combined with either accumulation or another compensating solution, that however will not be discussed here.
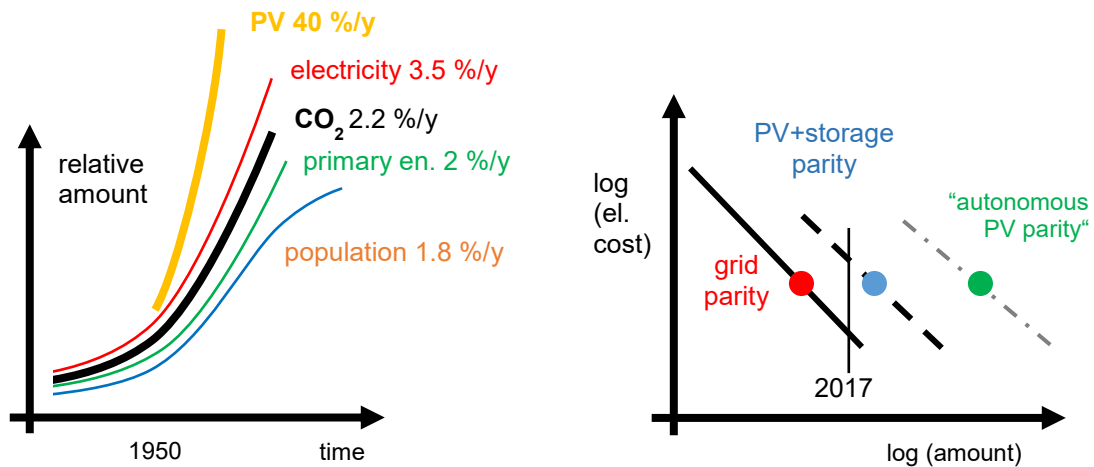

Figure 1: **Left**: schematic picture of increase of population, energies and CO_2 in atmosphere in recent history, percentage indicate trend in last years. **Right**: schematics of Swanson's law: Cost of PV energy halves every time the produced amount increases 10 fold. I assume that similar law works for system with storage and fully autonomous system. Parity indicates a point when cost of given technology is equal to the cost of electricity from the conventional grid.

Looking at the relative trends in population, primary energy consumption, CO_2 emissions, and electricity consumption we see growth at different speeds that are hard to follow for many technologies, see Fig. 1, left part. Photovoltaics (PV) mainly thanks to very fast and stable growth and not many fundamental restrictions, seems therefore to be a good candidate for energy source of future. That is mainly thanks to matureness of the production technology and easy and almost unlimited deployment of the photovoltaic systems. Photovoltaics has energy payback time 1-2 years and its greenhouse impact in equivalent to CO_2 is 10-30g/kWh (current energy mix in Europe has greenhouse gas equivalent around 500g/kWh), depending on location and technology (Alsema and de Wild-Scholten, 2007).

These are all usual arguments for political support of photovoltaics. Thanks to quite remarkably consensual and enormous support in past through so called feed-in tariff, photovoltaics has shifted very quickly along the so called Swanson's curve behind the spot – called "grid parity" – the point where the fabrication capacities allow prices competitive with conventional sources without any subsidies, see right part of Fig. 1. Today's energy from a roof-top system is 0.08 €/kWh (Fraunhofer ISE 2017). But as already stated, for a fair comparison with conventional sources, the combination with accumulation is necessary, which makes the system more expensive. Therefore system with accumulation may not be fully competitive at the moment, therefore a new phase of political support through single-shot subsidies (Nová zelená úsporám / New Green Savings Programme) is now being applied for systems with a kind of storage in order to accelerate the shift into another important point sometimes called 'PV+storage parity'. We can expect that photovoltaics may grow much faster after this point because using PV for households will become unrestricted way to save on electricity. Still, to be fully correct, the storage capability of such photovoltaic system with accumulation is designed and carefully sized only to minimize economical losses by unused photovoltaic energy, but it does not yet have any ambition to provide autonomy of such system. It means that the intermittent nature of sunlight is compensated by accumulation only partly, mainly only on a daily cycle. To compensate instability effects of winter or a row or cloudy days, another (backup) energy source will always be necessary in combination with PV.

In past, the solar cells and consequently the PV modules were most expensive components of the PV systems, therefore the efforts were focused to cut down costs of the solar cells. That was the time when hydrogenated amorphous silicon (a-Si:H)

was very popular material. But as the technology has matured and as the fabrication capacities has grown, since 2012 the costs of the PV modules are below 50% of the whole system, at least in Germany (Fraunhofer ISE PV report 2017). Today's cost of Chinese crystalline silicon module is 0.45 €/Wp (PVXCHANGE 2017) (For very rough assessment of the cost of energy, one can assume that in Central Europe 1 Wp of PV produces 20 kWh of energy during its lifetime.) There is less room now for reducing energy cost just by reducing cost of PV cell. Instead, better way of reducing cost of electricity is to increase efficiency of the solar cell as the main component determining the efficiency of the whole system. The path to high efficiency solar cells starts obviously with high quality materials. Characterization of solar cell materials, that is the topic of this thesis, is therefore very important.

1.2 Overview of today's technology status

Table 1: non-concentrator (potentially) industrially relevant photovoltaic technologies of 2017

full name	abbrev.	cell record (%)	module record (%)	annual prod. (GWp)	technological challenges
monocrystalline silicon	mono-Si	26.6	24.4	20.2	expensive ingot fabrication
multicrystalline silicon	multi-Si	21.9	19.9	57.5	grain boundaries passivation
cadmium telluride	CdTe	22.1	18.6	3.1	toxicity
chalkopyrite	CIGS	22.3	19.2	1.3	scarcity of indium
amorphous/microcrystalline	a-Si:H	14.0	10.9	0.5	Stabler-Wronski degradation
gallium arsenide (also "III-V")	GaAs	28.8			expensive Ge substrate
organo-metalhalide perovskite	$CH_3NH_3PbI_3$	22.1			stability in air
organic photovoltaics	OPV	11.5			stability in air
quantum dot solar cells	PbS QD	13.4			*not yet mature*
kesterites	CZTS	12.6			*not yet mature*

Although the absolute record of 46% solar to electricity conversion was achieved in 2014 by four-junction III-V solar cell with 508 times concentrated sunlight (Dimroth et al., 2016), we will not concentrate on these type of well established, but very special technologies. Instead, we will give our attention to technologies that are industrially relevant or those that might have this potential for future. As explained in previous section, the efficiency of solar cell is becoming very important for cost of energy. This has led to very tight competition in efficiencies of

the solar cells and their technologies, see Tab. 1. The actual best cell efficiencies (NREL 2017) are given there, for the technologies already industrially relevant the annual production together with the best module efficiency are also given (Fraunhofer ISE 2017). These technologies all have different challenges that are also briefly listed in Table 1, but that are not in focus of this thesis. This thesis will mostly focus on the fundamental properties of the absorber material – the core of every solar cell.
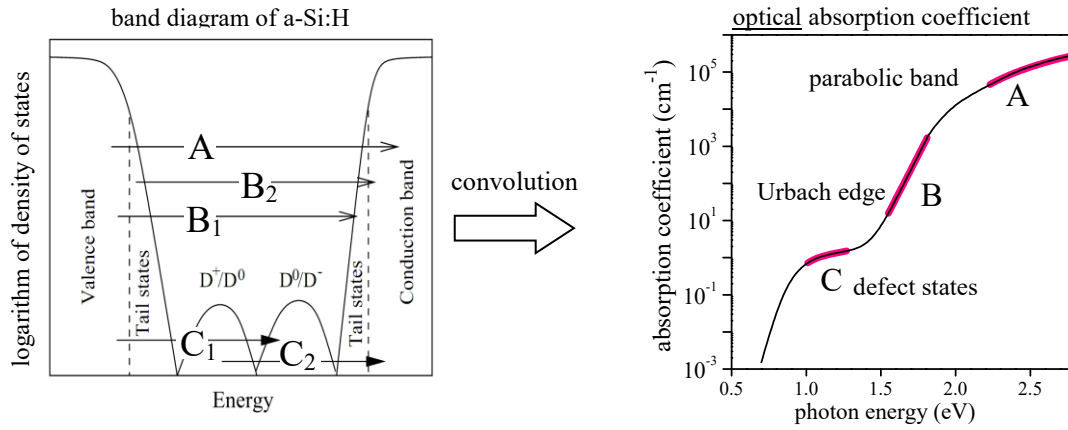

Figure 2: **Left**: band structure of density of electronic states of amorphous silicon. **Right**: optical absorption coefficient curve with indicated regions attributed to different electron transitions. In the simplest case of direct semiconductor and constant matrix element this curve is obtained as a convolution of the density of filled and empty states.

Interestingly, there are two groups of technologies separated by a considerable gap in efficiency (no record efficiency found in the range 14.0% - 21.9%). There must be a more fundamental reasons behind this separation than just a technology matureness. For example technology of a-Si:H used to be very well developed few years ago. On the other hand the technology of $CH_3NH_3PbI_3$ emerged only 8 years ago and quickly jumped over this gap (Yang et al., 2017). The reason for this lies in the properties of the absorber material. The absorber material is responsible for transformation of light into electron-hole pair and to maintain this disequilibrium sufficiently long to allow electron and hole to be guided into external circuit. The time necessary for electron-hole pair to recombine (return to equilibrium) depends on availability of the particles – photons and phonons – that can accept (by being created) the energy released during the recombination. Because absorber is usually at room temperature ($\vartheta=300K$), it is very easy to dissipate energy of 25meV ($k\vartheta=25meV$, $k=1.38064852 \times 10^{-23}$ Joule/Kelvin is Boltzmann constant).

If the material has a forbidden band where no states exist, so called bandgap, e.g. of energy E_g=1eV then the dissipation of energy into photon of the same energy is much less probable because in the photon distribution of black body at room temperature there is orders of magnitude less photons at 1eV then at 25meV. If there are no other defects such as grain boundaries, then the recombination strongly depends on the energy levels inside the bandgap. Ideal material would have perfectly sharp edges (valence edge and conduction edge) of the bandgap and no states inside the bandgap. Such material would have very low recombination given by thermodynamic limit and theoretical efficiency would be up to 33% (Shockley and Queisser, 1961). Real materials feature, partly due to defects and disorder, so called band tails decreasing exponentially toward middle of the bandgap, see Fig 2, left side. Additionally, they may have defect states inside the bandgap too.

The shape of the band tails can be observed in the shape of optical absorption coefficient $\alpha(E)$ spectrum, see Fig 2, right side. Absorptance A, i.e. the ratio of absorbed and incident intensity, of a layer of material with thickness d can be approximately expressed as equation (1) that again strongly follows the shape of absorption coefficient $\alpha(E)$ for low values of product αd. Because absorption and recombination has to be in equilibrium, the limit of radiative recombination can be calculated according to equation (2) by integrating optical absorptance spectrum $A(E)$ with spectrum of blackbody (3) at the cell's temperature ϑ (Jean et al., 2017; Vandewal et al., 2009). Other symbols have following meaning: c=299 792 458 m/s is the speed of light, q=1.602×10^{-19} Coulombs is the electron charge and J_0 is saturation current.

$$A(E) \approx 1 - e^{-\alpha(E)d} \xrightarrow[\alpha(E)d \ll 1]{} \alpha(E)d \qquad (1)$$

$$J_0 = q\int A(E) \cdot \Phi_{blackbody}(E) \ dE \qquad (2)$$

$$\Phi_{blackbody}(E) = \frac{2\pi}{h^3 c^2} E^2 \exp\left(1 - \frac{E}{k\vartheta}\right) \qquad (3)$$

The link to the solar cell operation is through the photovoltaic diode equation (4). Recombination in solar cell is attributed to the forward diode current given by the second term that has negative contribution. Other terms have following meaning: J_{ph} is photogenerated current, V is voltage on terminals, n is ideality factor, ρ_s is parasitic serial resistivity, and ρ_{sh} is parasitic shunt resistivity. The saturation current

J_0 is strong function of a material bandgap, i.e. the position of the absorption threshold, but apart from that it should be ideally as low as possible. For example for the best crystalline silicon solar cells it is in the range of $10 fA/cm^2$. The photogenerated current J_{ph} is similarly expressed as the integral of the absorptance and spectrum of sunlight (5) for which standardized spectrum labelled $AM1.5$ is used. Therefore it is also a strong function of the bandgap. Maximum voltage extracted from solar cell is open-circuit voltage V_{OC} given by equation (6) and happens when no load is connected to the cell and follows from equation (4) when $J=0$. For the best crystalline silicon cell giving photocurrent 40 mA/cm^2 the V_{OC} is as high as 725 mV. The equation (6) depends only on the ratio of J_{ph}/J_0. Because J_0 drops faster than J_{ph} when bandgap shifts toward higher energies the materials with higher bandgap have higher V_{OC}.

$$J = J_{ph} - J_0 \left(\exp^{\frac{V+J\rho_S}{nk\vartheta/q}} - 1 \right) - \frac{V+J\rho_S}{\rho_{sh}} \tag{4}$$

$$J_{ph} = q \int A(E) \cdot AM1.5(E) \ dE \tag{5}$$

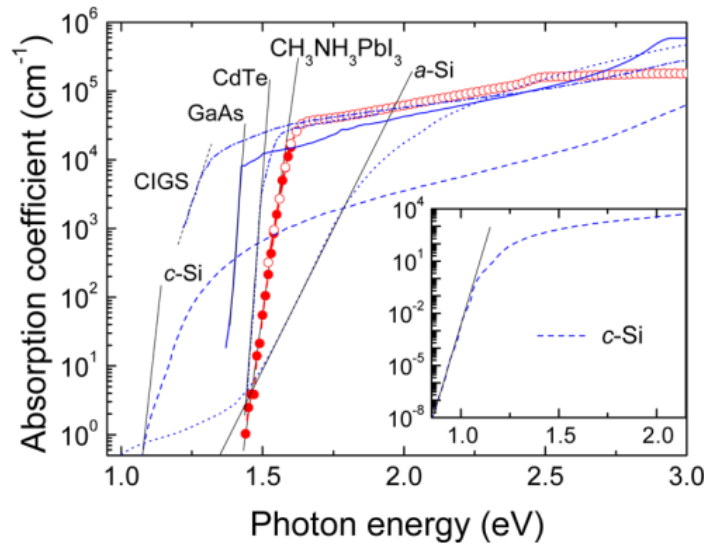$$V_{OC} = \frac{k\vartheta}{q} \ln \left(\frac{J_{ph}}{J_0} + 1 \right) \tag{6}$$

Figure 3. Absorption coefficient of different absorber materials used in PV technology. Straight lines indicate exponential part of absorption edge. The figure is taken from author's publication (De Wolf et al., 2014).

We can see that both parameters dictating theoretical limit of solar cell efficiency – photogenerated current and open-circuit voltage – depend mainly on the absorption threshold (bandgap) of the absorption coefficient. Optimum bandgap values E_g for single junction solar cell lies in the range from 1.1eV to 1.4eV (Shockley and Queisser, 1961) but other values might be advantageous for multi-junction solar cells. Absorption coefficients of the most important photovoltaic absorber materials are shown in Fig. 3. All the materials except crystalline silicon feature absorption coefficient higher than 10^4cm^{-1} above the absorption threshold thanks to so called direct bandgap. Crystalline silicon is a material with so called indirect bandgap that requires occurrence of phonon during photon absorption and therefore absorption is at least 20 times weaker than in materials with direct bandgap. Silicon solar cells can only be efficient due to sufficient thickness of the absorber. All the other materials absorb enough light within thickness of 1μm thickness [1μm=1/(10^4cm^{-1})] allowing for thin-film technology.
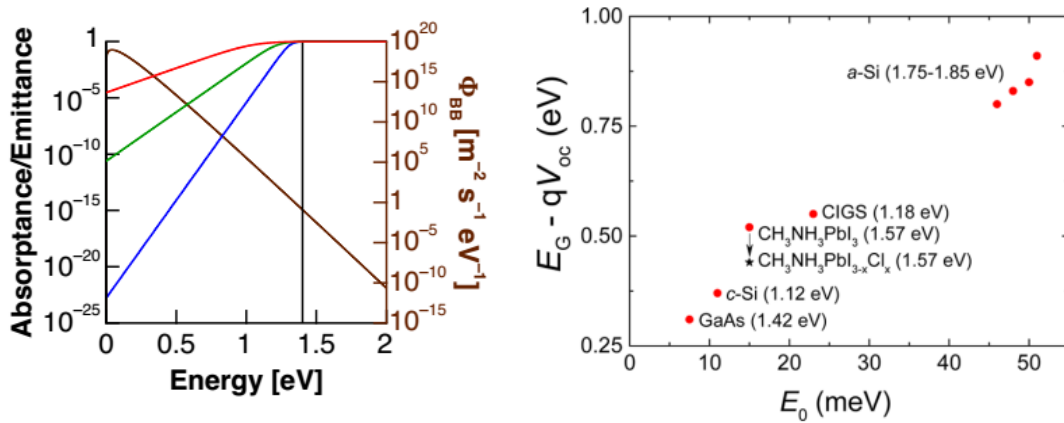

Figure 4. **Left**: Red, green and blue lines show absorptance in the case of E_U=100meV, 50meV and 25 meV respectively and brown line show spectrum of blackbody radiation. **Right**: Voltage deficit as a function of Urbach energy for the best laboratory devices. Figures taken from author's publication (De Wolf et al., 2014; Jean et al., 2017).

Below the absorption threshold, the absorption coefficient fall exponentially. This empirical rule is called Urbach rule (Urbach, 1953) and Urbach energy E_0 defines that exponent as follows (Street, 1991):

$$\alpha(E) \propto \exp\left(\frac{E}{E_0}\right) \tag{7}$$

The result of equation (2) and then also equation (6) is then also dependent on the Urbach energy, i.e. on the slope (bandtail) of the absorption edge, see Fig 4, left part. To distinguish between effect of bandgap and the effect of bandtail (or Urbach energy) so called voltage deficit is defined as E_g/q-V_{OC}. The voltage deficit is important figure of merit of PV materials and we can see in the right part of Fig. 5 that it strongly correlates with Urbach energy. It can be seen that the technology of a-Si:H is most to the right on the Urbach energy axis explaining its low efficiencies given in Tab 1.

The shape of the sub-bandgap absorption have been recognized as important parameter for evaluating many semiconductor materials, not only because the Urbach energy, but also because defect absorption can be sometimes evaluated too. The methods of measurement of sub-bandgap absorption are therefore important. The topic of this habilitation thesis is especially focused on sub-bandgap absorption in photovoltaic materials, its experimental measurement, correct evaluation and scientific interpretation. Both published and unpublished work within this field are included. Work that is outside this field is not included.

2 Methods of low absorption spectroscopy

In the section 1 the importance of the shape of sub-bandgap optical absorption was pointed out. All Fig. 2, 3, and 4 (only left part) show absorption coefficient or absorptance in logarithmic scale. It means that it is necessary to determine it over a very large dynamic range. Reflectance R, i.e. the ratio of reflected and incident intensity is only weakly dependent on absorption coefficient. Then the absorptance A, or transmittance T, i.e. ratio of transmitted and incident intensity can be used. Note that in both cases it is not possible to measure accurately when the amount (T or A) is saturated. Which means that A or T should be measured when they are considerably smaller than 1. Often in chemistry transmittance is used to determine so called absorbance Abs according to equation (8). Absorbance is little similar to absorption coefficient α because there is also logarithmic relation between them, see equation (9). But using the same approach of measuring transmittance will not work very well. With a standard sensitivity of measuring T down to 0.01%, i.e. four orders of magnitude of dynamic range one would obtain absorption coefficient

only with around one order of magnitude dynamic range. Moreover this requires making the layer of the material quite thick. Conversely, it is more advantageous to make the layer of the material thin, so that the absorptance A is weak and the equation (1) holds (first order of Taylor expansion). Then, by measuring absorptance with four orders of magnitude can give around same orders of magnitude range of absorption coefficient.

$$Abs = -\log T = -0.43 \ln T \tag{8}$$

$$T \approx (1-R) \exp(-\alpha d) \tag{9}$$

After proving that low absorptance measurement is more useful than low transmittance we have to discuss possible method. Typically, absorptance would be measured indirectly as a complement of transmittance T and reflectance R into unity, see equation (10), but due to the effect of saturation of T for low A this method would give accurate absorptance not below 1%. It means that some direct methods must be used. In following, two of them will be described.

$$A = 1 - T - R \tag{10}$$

2.1 Photothermal deflection spectroscopy
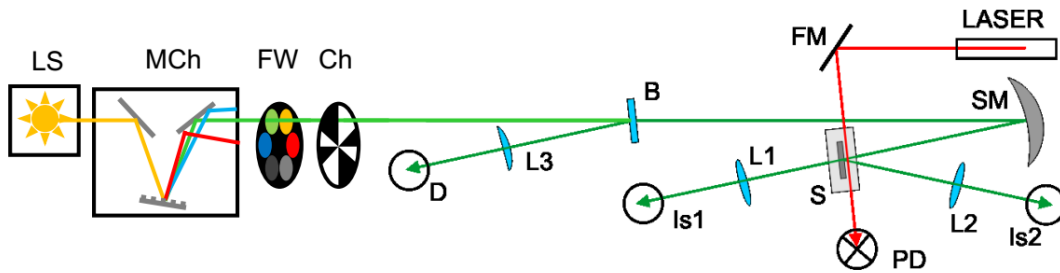
Figure 5: Schematic layout of photothermal deflection spectroscopy apparatus. LS – light source, MCh – monochromator, FW – filter wheel, Ch – chopper, B – beamsplitter, L1,L2,L3 – lenses, Is1, Is2, D – detectors for transmittance, reflectance and background, FM, SM – flat and spherical mirrors, PD – position detector, S – sample inside cuvette, immersed in FC72 liquid

Photothermal deflection spectroscopy (PDS) is a direct method allowing absorptance measurement of thin films on non-absorbing substrates. It was first used for a-Si:H absorbers (Jackson and Amer, 1982). It's principle (Boccara et al., 1980) is as follows: Sample is immersed in liquid that has strong dependence of refractive

index on temperature. Light absorbed in sample is assumed to be entirely transformed into heat that is transferred into the surrounding liquid. Usually Fluorinert FC72 is used. In past, hazardous CCl_4 was used too. Temperature gradient and consequently refractive index gradient is formed around the sample. Laser that is passing closely to the sample is deflected by this gradient and the deflection is registered by position detector, see Fig. 5.

It is assumed that laser deflection is proportional to the absorptance, but the proportionality constant is never known accurately because it depends on individual adjustment of each sample. Therefore it is advantageous to equip the setup also by measurement of transmittance T and reflectance R and to calculate absorptance absolutely in region of high absorptance according to equation (10) and to adjust the PDS result accordingly. Sensitivity of PDS is going down to 0.01%, for example allowing to reach level of absorption coefficient $1 cm^{-1}$ for layer of $1 \mu m$ thickness.
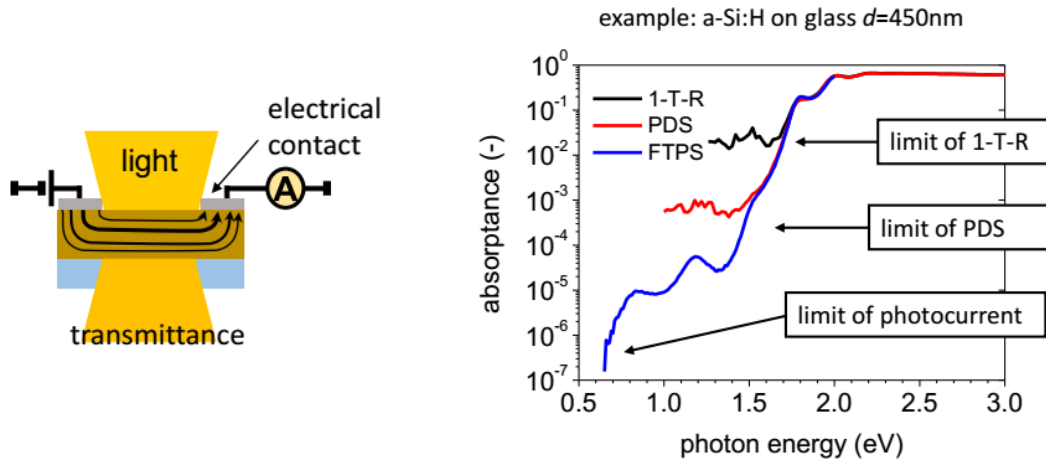

Figure 6**: Left**: Coplanar contacts of a thin film in the photocurrent method. Transmittance is often also measured. **Right**: Comparison of sensitivity of measurement $1 - T - R$, PDS and photocurrent.

$$\alpha \cong \frac{1}{d} \ln \left(0.5 \left\{ (1 - R_{12})(1 + A/T) + \sqrt{(1 - R_{12})^2 (1 + A/T)^2 + 4R_{12}} \right\} \right) \qquad (11)$$

Relation between absorption coefficient and absorptance is complicated, mainly due to the effect of interference maxima in whole sub-bandgap region, see Fig. 6. Rigorous equations cannot be inverted to easily express absorption coefficient from absorptance. Fortunately, approximate equation (11) was derived (Ritter and Weiser, 1986) because at the same time it was shown that the ratio A/T for thin film

has strongly reduced interference maxima. Term R_{12} express reflectance of the back surface of the sample - please refer to equations (15). Analogically, ratio $A/(T+A)=A/(1-R)$ has reduced interference maxima too (Hishikawa et al., 1991). That is why it is useful to measure also transmittance or reflectance together with the absorptance. Because usually, refractive index n is unknown, it has to be fitted together with the evaluation of absorption coefficient. According to (Born and Wolf, 1998, p. 95) the refraction index below the absorption edge can be approximately described by Cauchy formula (12) that has only two parameters n_{C0} and n_{C1}. The thickness d (and sometimes also absolute scaling of A) might neither be known. In such case the usual practice is following: We take first guess of n_{C0}, n_{C1}, d (and absolute scaling factor for A) and we use formula (11) to calculate absorption coefficient. From that, transmittance of the sample can be rigorously calculated by usual Fresnel equations (13) and this is compared to measure transmittance. Iteratively parameters are varied to get the best agreement.

$$n(\lambda) = n_{C0} + n_{C1} / \lambda(\mu m)^2 \tag{12}$$

$$r_{01} = \frac{N_0 - N_1}{N_0 + N_1} \qquad t_{01} = \frac{2N_1}{N_0 + N_1} \quad \text{where} \quad N = n + i\frac{\alpha\lambda}{4\pi} \tag{13}$$

$$r_{02} = \frac{r_{01} + r_{12}e^{2i\beta}}{1 - r_{10}r_{12}e^{2i\beta}} \qquad t_{02} = \frac{t_{01}t_{12}e^{i\beta}}{1 - r_{10}r_{12}e^{2i\beta}} \quad \text{where} \quad \beta = 2\pi N d / \lambda \tag{14}$$

$$T_{kl} = \left|t_{kl}\right|^2 \frac{n_l}{n_k} \text{ (if } k, l \text{ are non-absorbing media)} \qquad R_{kl} = \left|r_{kl}\right|^2 \tag{15}$$

In the equations above r_{01} labels ratio of reflected electric field and incident electric field at the interface between 0-th and 1-st medium. N stands for complex refractive index and i is imaginary unit. Analogically, t_{01} labels ratio of transmitted electric field. Symbols r_{02} and, t_{02} label ratio of reflected and transmitted electric field between 0-th and 2-nd medium while the 1-st medium represents the layer with thickness d.

2.2 Photocurrent spectroscopy

To increase sensitivity below the 0.01% threshold, for example to measure defect density in a-Si:H for layers thinner than 1μm, photocurrent method can be used, see Fig 6. Another advantage of photocurrent is the possibility to measure

layers on absorbing substrates because only the absorbed photons contributing to electrical conductivity are accounted.
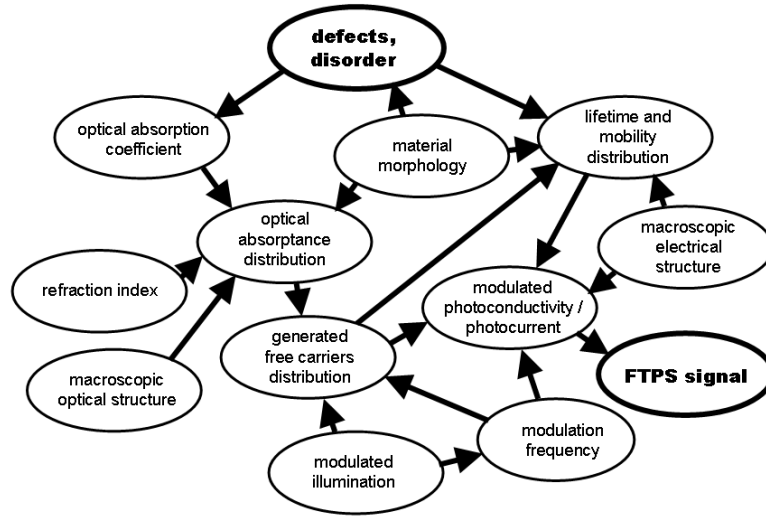

Figure 7: Diagram showing most of the possible effects interfering into photocurrent (FTPS) spectroscopy. More details in (Holovský, 2011)

Unfortunately, photocurrent is very complex process where many other physical, especially electrical effects interfere (Holovský, 2011), see Fig 7. Materials like conductors or insulators cannot be measured at all. When the material is semiconductor, the main factor influencing photoconductivity is the product of carrier mobility μ and lifetime τ. To maintain this product constant the approach of constant photocurrent method (CPM) (Vaněček et al., 1981) was suggested. By varying the intensity and keeping the photocurrent constant, the level of carrier concentration is also believed to be constant. Alternatively, dual beam photocurrent (DBP) method applies large constant light bias with much higher intensity than the modulated monochromatic light so that carrier concentration is fixed by the level of constant intensity. Drawback of this method is that the spectra depend on level of illumination (Morgado, 2001). Later, Fourier-transform photocurrent spectroscopy (FTPS) was introduced by using commercial Fourier-transform infrared (FTIR) spectrophotometer mainly to speed up the measurement (Jongbloets et al., 1979; Tomm et al., 1997; Vanecek and Poruba, 2002). In this method all the wavelengths are measured at the same moment so that the generated photocurrent is also kept at

the same level. The problem of FTPS method is quite high modulation frequency of few kHz (Holovský et al., 2008).

2.3 Comparison of methods

Due to different physical conditions, the methods may give different results. For example, in Fig 2 the transition C_1 is not accounted in photocurrent spectroscopy of a-Si:H because the mobility of holes is around 20 times smaller than for electrons in this material. But in PDS both C_1 and C_2 transitions are accounted. To evaluate defect states in a-Si:H by CPM, the value of absorption coefficient at 1.2 eV is taken and multiplied by value around $2.4\text{-}5\times10^{16}\text{cm}^{-2}$ to obtain defect concentration. For using PDS data the value is divided by 2 (Wyrsch et al., 1991) because PDS is twice more sensitive to the defect absorption.
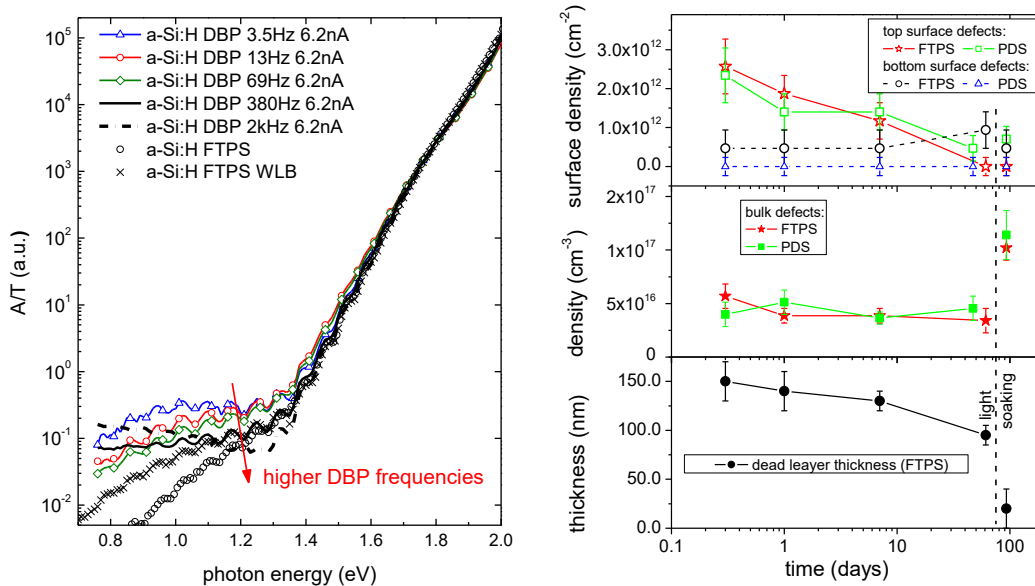
Figure 8: Left: Comparison of A/T obtained by FTPS with light bias (LB) and DBP measured at different frequencies on a layer of 2 μm thick a-Si:H layer on glass. Drastic changes in Urbach slope and in region of defect density around 1.2 eV are evident. **Right**: Evolution of bulk and surface defects in time on a 360 nm thick a-Si:H layer on glass, obtained by FTPS and PDS separately.

Another difference is caused by the non-uniform lifetime distribution across the sample. Surface defects cause lower lifetime in surface layers, called dead layer. We analysed that carriers generated in such sub-surface layer contribute to photocurrent with 4 times reduced efficiency (Holovský et al., 2012). It means that

PDS method, where effect of mobility has no role is four times sensitive to absorption in surface defects. In right part of Fig. 8 we show analysis where these correction factors (2 for bulk defects and 4 for surface defects) were used to correct the photocurrent measurement in order to obtain equivalent results as from the PDS method.

Modulation frequency has another strong effect on the subbandgap absorption measured by FTPS, CPM or DBP (Holovský et al., 2008), see Fig 8, left part. The drop of defect related absorption can be partly attributed to strong frequency dependence of transitions C_1. These effects are consistent with findings of other authors (Main et al., 2004; Sládek and Thèye, 1994), but still not fully understood.

3 Effects of surface layers

Typically in the case of layers of a-Si:H on glass, the defect density is much larger close to the surfaces. If the layer is not thick enough absorptance on the surface defects may mask the evaluation of defect density inside the layer. However, presence of surface defects manifest as non-vanishing interferences in A/T ratio because the rule of interference maxima reduction in A/T is not valid when more complex structure is present such as in the case of additional surface defective layer. Moreover, this effect depends on direction of the light incidence. Measuring for both directions then gives the opportunity to evaluate the amount of surface defects in the layer (Holovský et al., 2012). We have seen that surface defects evolve during the time, see right part of Fig. 8. Surface defects have to be optically simulated as additional surface layer, which normally brings more unknown parameters to the evaluation. To reduce the number of unknown parameters we elaborated further so called thin-film limit (Brendel, 1991; Weber et al., 2014) and we derived simplified equations (16 – 18) (Holovský and Ballif, 2014) for transmittance T_{TFL}, absorptance A_{TFL} and reflectance R_{TFL} of a layer with thickness approaching zero.

$$T_{\text{TFL}} = \frac{4 n_0 n_2}{\left(n_0 + n_2 + \alpha d n \right)^2} \tag{16}$$

$$A_{\text{TFL}} = \frac{4 \alpha d n n_0}{\left(n_0 + n_2 + \alpha d n \right)^2} \tag{17}$$

$$R_{\text{TFL}} = \frac{\left(n_0 - n_2 - \alpha dn\right)^2}{\left(n_0 + n_2 + \alpha dn\right)^2} \tag{18}$$

Symbols n_0, n and n_2 denote refractive index of medium in front of the layer, layer itself, and medium behind the layer, respectively. Most importantly, we should notice that all the properties T_{TFL}, A_{TFL} and R_{TFL} of the ultrathin layer are only functions of product αdn. It means that in the thin film limit the knowledge of absorption coefficient α, thickness d and refractive index n is replaced by knowledge of only one number αdn. The equations (16 – 18) allow us to reduce unknown parameters for simulating the effect of surface layer and they are also simple enough to allow direct evaluation of surface defects if the measurement of absorptance is performed twice for light incident from both sides of the sample (Holovský and Ballif, 2014).

Validity of the equations (16 – 18) was tested by comparison with rigorous calculations for a range of absorption coefficient, for thickness of either 1 nm or 10 nm and refractive index n=2.52. This refractive index was chosen to test validity of thin-film limit for graphene (Holovský et al., 2015). We have also shown that within the thin-film limit the optical losses due to absorptance in graphene scale with surrounding refractive index, which does not happen for layers with usual thicknesses of 100 nm. This is important consideration for possible application of graphene as a transparent electrode.
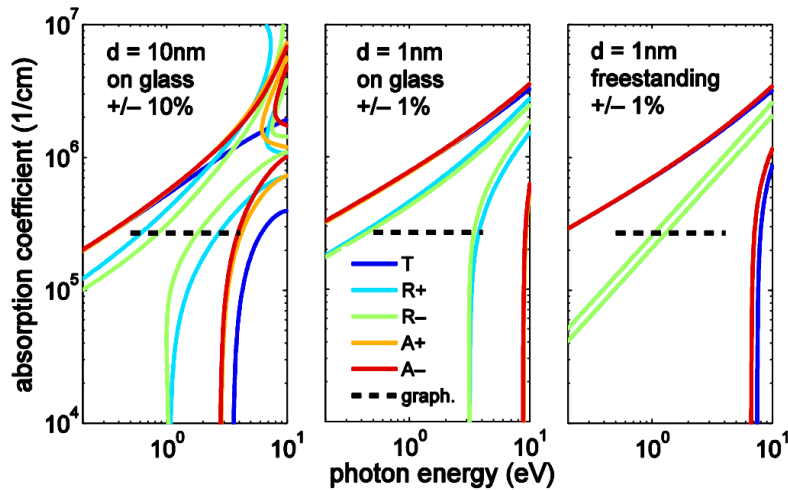
Figure 9: Lines represent contours between which the TFL differ from rigorous calculation less than 10% or 1% relatively. R+, A+, refer to incidence from layer side, conversely R–, A–, refer to glass side. Note the difference between freestanding layer and layer on glass. Dashed line between 0.5eV and 4eV indicates the theoretical absorption coefficient of graphene α_{graphene}=271562 cm^{-1}.

4　Effects of light scattering

Light scattering happens when either surface of the layer is rough or when the material is not optically homogeneous, e.g. due to addition of some nanoparticles. These strategies are often used in thin film solar cells to increase light absorption. One of the popular approaches to increasing light absorption is introducing so called plasmonic nanoparticles. These nanoparticles are metallic and their free electrons may collectively oscillate which may amplify the electric field and also scatter light (Green and Pillai, 2012). However, one of the two main problems of such approach is that metals are in principle very strongly absorbing. For perfectly smooth metal surface, reflectance is high in air due to high absorption coefficient and therefore high complex refractive index. But this is not true when metal is incorporated in semiconductor in form of nanoparticles.
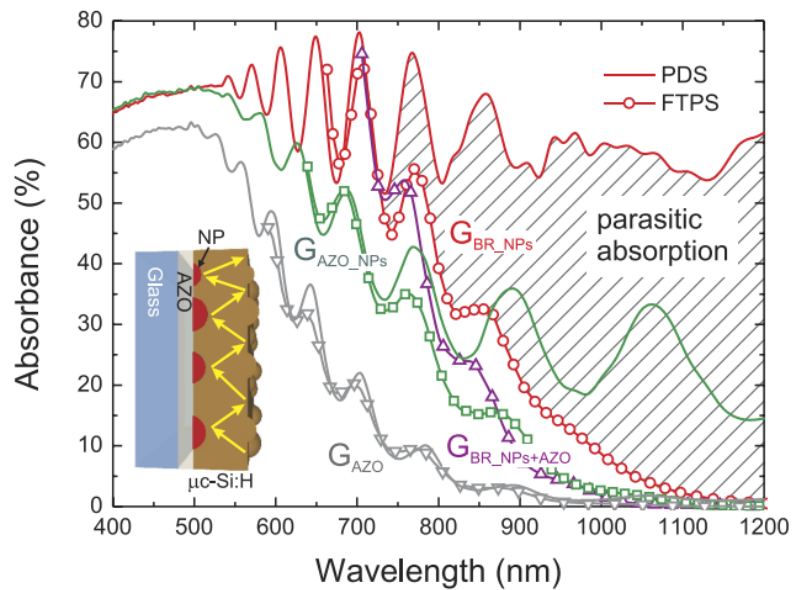
Figure 10: Total (PDS) and useful (FTPS) absorption spectra of 0.9 μm thick microcrystalline films deposited on different substrates: AZO stands for Al doped ZnO, NPs stands for silver nanoparticles, and BR stands for smooth silver layer. Inset shows the case of AZO_NPs. The marked area is the difference between the PDS and FTPS spectra, which represents the parasitic absorption of the silver nanoparticles and partly also the silver layer.

To evaluate scattering properties and related absorption losses in microcrystalline silicon we used combination of PDS and FTPS measurement

(Morawiec et al., 2016), see Fig. 10. While PDS measures all absorbed light including parasitic absorption of metal nanoparticles, FTPS measures only the light absorbed in the microcrystalline silicon and contributing to photo-generation. When the substrate is conductive, such as in the case of Al doped ZnO or silver layer, FTPS cannot be used in the arrangement of coplanar contacts as in left part of Fig. 6. Instead a sandwich configuration is used, in which the sample arrangement resembles solar cell (Holovský et al., 2010; Morawiec et al., 2016).

Mathematical evaluation and correction of scattering is extremely difficult. In the case of scattering many preceding equations, namely (1), (11) and (14) remain valid only for a small portion of light beam that is not scattered. According to approximate theory of scalar scattering (Beckmann and Spizzichino, 1963) the Fresnel coefficients are reduced by s-factors, equations (19), (20). The s-factors express how the amplitude of non-scattered light is reduced. The reduction of non-scattered field depends on refraction indices n_i, wavelength λ, incident angle φ, and root mean square roughness σ_{RMS}. While the portion of non-scattered light can be treated as before, another part of the calculation has to be added to treat the scattered light. Then either a Monte-Carlo ray tracing (Krč et al., 2004; Schulte et al., 2011; Springer et al., 2004), or matrix approach (Lanz et al., 2011; Leblanc et al., 1994; Santbergen and van Zolingen, 2008) is used to treat the scattered light. Scalar scatering theory is correct for morphology that has the correlation distance smaller than wavelength of light. On the other hand, scattering on large morphological features can be treated by geometrical optics. Scattering on medium size features is the most difficult and requires most advanced techniques based on direct solving of Maxwell equations (Bittkau et al., 2011; Čampa et al., 2010; Haase and Stiebig, 2006; Klapetek et al., 2010; Naqavi et al., 2010).

$$r_{ij} \to r_{ij}s_{ij}^{R} \qquad s_{ij}^{R} = \exp\left[-\frac{1}{2}\left(\frac{4\pi n_i \sigma_{RMS}\cos\varphi_i}{\lambda}\right)^2\right] \qquad (19)$$

$$t_{ij} \to t_{ij}s_{ij}^{T} \qquad s_{ij}^{T} = \exp\left[-\frac{1}{2}\left(\frac{2\pi(n_i - n_j)\sigma_{RMS}\cos\varphi_i}{\lambda}\right)^2\right] \qquad (20)$$

We have used Monte-Carlo ray tracing instrument called CELL (Springer et al., 2004), based on the equation (19 – 20), to evaluate absorption coefficient of a-Si:H grown on different and also differently rough absorbing and conductive

substrates. Similarly as in the previous case of metal nanoparticles (Fig. 10) this experiment required photocurrent method in sandwich configuration. We have shown that quality and the bandgap of this material may depend on the surface morphology considerably (Holovský et al., 2010).
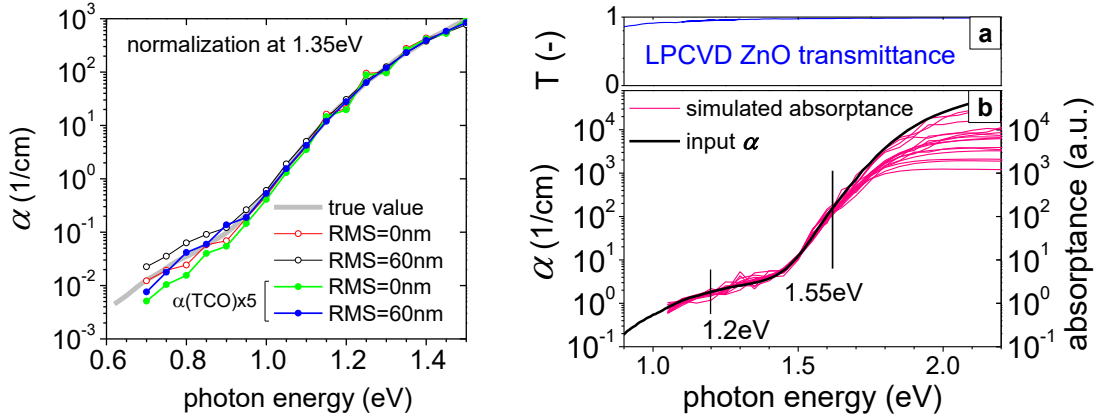
Figure 11: Simulation of absorptance in i-layer for different values of σ_{RMS}, absorber thickness or different absorption coefficients of ZnO ("TCO"). **Left**: Absorptance spectra of microcrystalline silicon normalized to 245cm^{-1} at 1.35eV. **Right**: a) ZnO transmittance b) Absorptance spectra of a-Si:H solar cell rescaled to best fit the absorption coefficient between 1.2 and 1.55 eV. Absorber thickness varied from 120 to 1000 nm and σ_{RMS} of interfaces varied from 0 to 100 nm.

Any kind of scattering simulations, not only that it is difficult, it always requires a lot of additional parameters, such as the root mean square roughness σ_{RMS} or angular distribution function that can neither be easily and accurately determined. If the material is incorporated in a solar cell, additionally the effect of absorptance in transparent electrode is accounted. For evaluation of sub-bandgap absorption, however, it is not always necessary to simulate all these effects, because below certain level of absorptiance the enhancement due to the light scattering tends to saturate. Simulation of different cases is shown in Fig 11. In the case of microcrystalline silicon we know that the absorption coefficient – normalized to crystalline phase (Python, 2009) – should pass through a point 245cm^{-1} at 1.35eV. Below this reference point the shape of absorptance should not be significantly influenced by the scattering. Similar behaviour is observed for a-Si:H below 1.55 eV, but in the case of a-Si:H there is not such unique reference point, because the bandgap of this material changes according to its hydrogen content. Alternatively, if

no reference point exists, the same material can sometimes be grown in a form of a smooth layer on glass and measured by PDS and accurately evaluated in medium – high absorption range. Then the photocurrent measurement can be measured in low absorption range and stitched to the PDS measurement at carefully chosen point. We have applied this in the case of microcrystalline silicon grown by two different speeds giving different defect density but also different level of crystallinity (Strobel et al., 2015).

5 Organo-metalhalide perovskites

The organo-metalhalide perovskite material became quickly famous thanks to exceptionally high quality of solution-processed absorber material for solar cells, allowing unprecedented fast progress in their conversion efficiencies up to today's 22.1% (Yang et al., 2017). This efficiency is possible due to very high voltage (over 1.1 V) compared to the bandgap of 1.57 V, giving the voltage deficit E_g/q-V_{OC} only 0.47 V. According to trend in right part of the Fig. 4, this suggests very low Urbach energy. We have for the first time measured Urbach energy of the $CH_3NH_3PbI_3$ by PDS and FTPS method, obtaining value as low as 15 meV (De Wolf et al., 2014).

The organic-inorganic halide perovskites is a broad class of materials consisting of negatively charged lattice that is formed by one divalent metal atom like Pb (Brivio et al., 2013; Burschka et al., 2013) and three halogen atoms X_3 (X=I, Cl or Br) and is filled by organic cation, usually $CH_3NH_3^+$ (Brivio et al., 2013; Frost et al., 2014). In the so called two-step process (Burschka et al., 2013) the perovskite layers are fabricated by dipping PbI_2 coated glass into a solution of CH_3NH_3I while the $CH_3NH_3PbI_3$ perovskite is immediately formed. The resulting layers are instable in ambient humidity, tending to decompose back into PbI_2 (Frost et al., 2014; Noh et al., 2013). Therefore, the actual film may often consist of two phases of pure perovskite and PbI_2. This consideration was the key we used to explain effects observed in absorptance (De Wolf et al., 2014) and Raman spectroscopy (Ledinský et al., 2015) simply as a summation of the respective components. In the photocurrent spectra, however, very simple summation of respective components does not work. The residual PbI_2 phase has lower conductivity than the $CH_3NH_3PbI_3$ phase, therefore the light absorbed in PbI_2 phase should be considered as lost from

the photocurrent point of view.
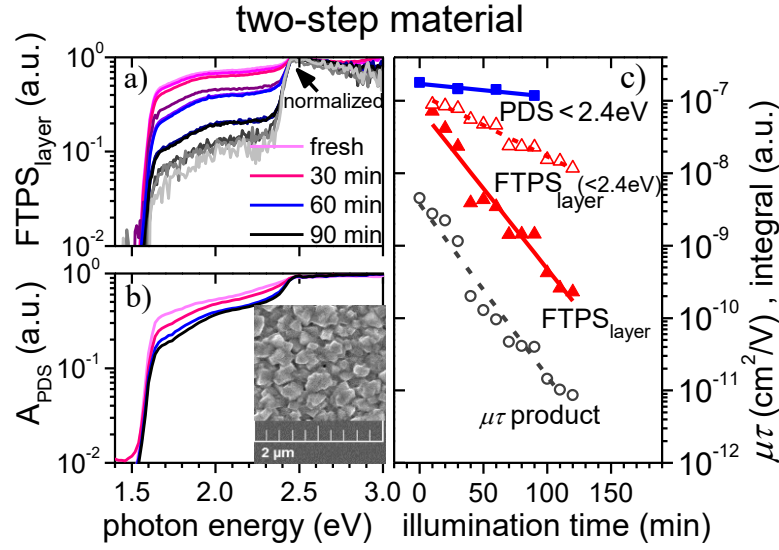
Figure 12. Evolution of spectra of **a)** normalized *FTPS* and **b)** absorptance measured by PDS A_{PDS}. Interestingly, the step around 2.4 eV in the photocurrent is much larger than in the PDS. Panel **c)** shows the effective $\mu \times \tau$ product together with integral values as a function of the illumination time. Label "< 2.4eV" means that the integral value below 2.4eV was taken from the spectra normalized at 2.5eV. The inset in panel b) shows a scanning electron microscopy image of the fresh perovskite film.

One would expect that above the absorption edge of PbI_2 a drop in photocurrent spectrum will occur because light absorbed there would not contribute. The opposite is observed, see Fig. 12 panel a), after the absorption threshold of PbI_2 phase, the photocurrent increases. To explain this behaviour we suggest a charge transfer mechanism that allows mainly holes to escape from PbI_2 into $CH_3NH_3PbI_3$ while electrons remain in PbI_2. This significantly prolongs the lifetime of such hole so that eventually they contribute to the photocurrent more than the holes generated in $CH_3NH_3PbI_3$ phase. Generally, FTPS signal measured on layer $FTPS_{layer}$ is proportional to product of absorptance A, lifetime t and mobility μ, while mobility is a sum of mobility of holes μ^h and electrons μ^e. For the two phase system we describe it by more complex equation (21) where $CH_3NH_3PbI_3$ and PbI_2 are labeled as 1 and 2, respectively.

$$FTPS_{layer} \propto \sum_{i=1,2} \sum_{j=1,2} A_i (\tau_{ji} \mu_j^e X_{ij}^e + \tau_{ij} \mu_j^h X_{ij}^h) \quad \& \quad \sum_{i=1,2} A_i = A_{PDS} \qquad (21)$$

In this equation the parameter X_{ij} expresses the charge transfer of given carrier

(*e* refers to electrons, *h* refers to holes) from material *i* to material *j*. The carrier lifetime τ_{ij} represents the case when electron is in material *i* and hole is in material *j*. Obviously, separating electrons from holes leads to much higher lifetimes τ_{ij} for which $i \neq j$ ($\tau_{21} \gg \tau_{11}$). If we make assumption of only very low lifetime of electron-hole pairs generated in PbI$_2$ ($\tau_{22} \approx 0$) and that the only effective charge transfer is the one of holes from PbI$_2$ into CH$_3$NH$_3$PbI$_3$ ($X_{22}^h < 1$, $X_{21}^h > 0$ while $X_{11}^e, X_{11}^h, X_{22}^e \approx 1$ and $X_{12}^e, X_{12}^h, X_{21}^e \approx 0$), see Fig .13, then the spectra and trends in Fig. 12 can be explained (Holovský et al., 2017).
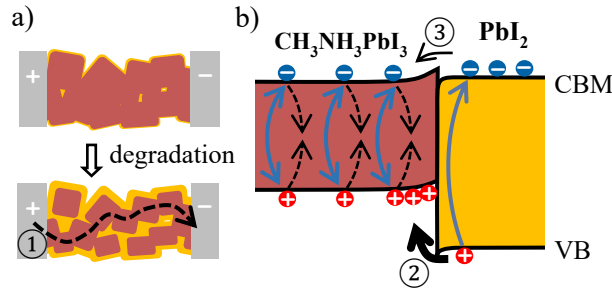

Figure 13. Model of the CH$_3$NH$_3$/PbI$_2$ interface. CBM and VBM refer to conduction band minimum and valence band maximum, respectively. The PbI$_2$ phase restricts the current flow to only a narrow path ①. Holes generated in the PbI$_2$ are injected into the CH$_3$NH$_3$PbI$_3$ (process ②). Consequent charging and band bending combined with thermal excitation also allow electron injection (process ③).

6 Transparent conductive oxides

Transparent conductive oxides are used as front conductive electrodes in solar cells. To provide sufficient conductivity, either high carrier concentration or high carrier mobility is necessary. But higher conductivity causes higher optical losses due to free-carrier absorptance. Because the carrier mobility has weaker effect on the free-carrier absorption than carrier concentration, it is useful to increase carrier conductivity rather than carrier concentration. Because the conductivity is limited by grain boundaries in the polycrystalline materials, amorphous materials for example hydrogenated amorphous In$_2$O$_3$ (Koida et al., 2007), InZnO (Morales-Masis et al., 2015) or ZnSnO (Rucavado et al., 2017) are intensively investigated. Urbach energy may vary considerably in amorphous materials according to their level of disorder due to structural defects like oxygen vacancies. We applied sub-bandgap absorption

spectroscopy of amorphous InZnO to study the effect of adding small amount of oxygen into argon gas during the sputtering from target with composition 90 wt% In_2O_3 and 10 wt% ZnO.
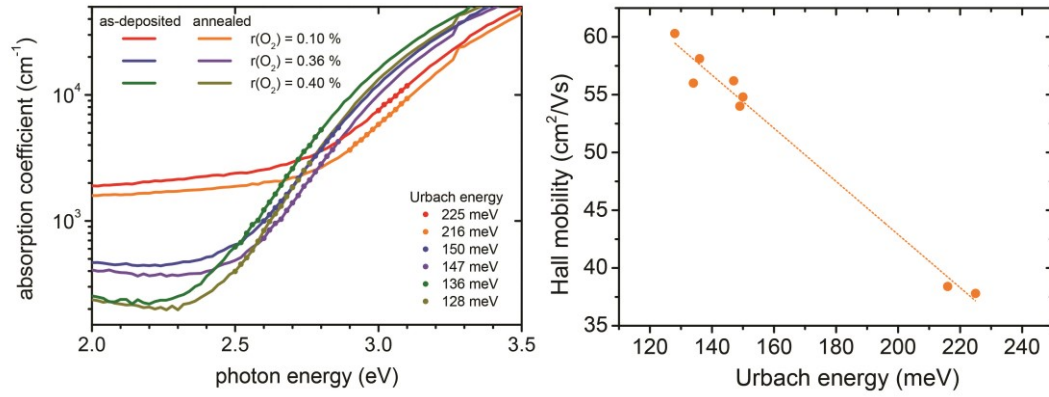
Figure 14: Left Absorption edge of amorphous IZO thin films prepared with three different oxygen contents, before and after annealing. The symbols indicate the slope used to extract Urbach energy. **Right** Correlation between Hall mobility and Urbach energy.

Urbach energy was evaluated from absorption coefficient extracted from PDS measurement. Annealing in air at 190 °C for 20 min was applied, leading to improvement of material order and therefore reduction of Urbach energy. Electron mobility was measured by Hall measurement and strong correlation with Urbach energy was obtained, see Fig. 14. (Morales-Masis et al., 2015).

Similar study was conducted with the amorphous ZnSnO material where the annealing was conducted under different atmosphere: air, nitrogen and hydrogen (Rucavado et al., 2017). Annealing temperature was 150°C, when only slight changes were observed and 500°C, when significant changes were observed. Annealing in nitrogen has only a slightly beneficial effect. Annealing in air, due to the presence of oxygen has a strong beneficial effect of passivation oxygen vacancies. On the other hand, annealing in hydrogen has a reduction effect that induces more defects.

7 Conclusions

In this thesis I summarized the work done in the narrow field of optical spectroscopy of absorption edge of the photovoltaic materials. This concerned the spectroscopy methods, the interpretation of results, properties of the studied photovoltaic materials and also brief motivation to the photovoltaic technology as a potential clean energy source.

The competitiveness of the solar energy now depends only on the ability to consume the produced energy. In the case of large mismatch between generation and consumption profile, expensive accumulation is necessary that may weaken its competitiveness. Otherwise in the case of favourable matching the cost of solar energy is below the cost of energy from the grid. This is mainly thanks to larger fabrication capacities and economy of scale that pushed down cost of solar cells. Further cost reduction will be possible solely by increasing conversion efficiency.

Ultimately, conversion efficiency is limited by the properties of absorber semiconductor material. Theoretically, 33% efficiency of single solar cell is possible with ideally sharp optical absorption edge of the semiconductor. This theoretical limit is reduced already by the simple fact that some residual absorption exist also below the absorption edge. This is the sub-bandgap absorption and sensitive absorption spectroscopy methods can measure this.

The two methods of sub-bandgap absorption spectroscopy discussed are photothermal deflection spectroscopy and photocurrent spectroscopy. The comparison of the two methods is also discussed here. The main advantage of the photocurrent is the sensitivity that can be three orders of magnitude larger. Disadvantage of the photocurrent is that there are many additional parameters that interfere into the measurement (Holovský, 2011), such as different mobility of electrons and holes. Photocurrent signal may also suffer from frequency dependence that is especially important issue for the case of Fourier-transform implementation of the method where high modulation frequencies are used (Holovský et al., 2008).

Photocurrent and photothermal deflection spectroscopy have each different sensitivity to bulk and also surface defects (Holovský et al., 2012). Measurements can in principle be corrected for parasitic contribution of surface defects if a simplified formalism of thin-film limit is used (Holovský and Ballif, 2014).

In general, the combination of the two measurement can be beneficial, for example accurate evaluation of absorption coefficient by photothermal method in medium-to-high absorption range on a layer on glass combined with evaluation in low absorption part by photocurrent (Strobel et al., 2015). This might be the way of treating layers with light scattering. Combination of photothermal and photocurrent spectroscopy can also be used to evaluate useful and parasitic absorption in solar cells using plasmonic particles (Morawiec et al., 2016). Photocurrent in the sandwich configuration can be used also in the case of absorbing and conductive substrates, such as aluminium (Holovský et al., 2010).

The materials studied in past by the two methods were mostly amorphous silicon (a-Si:H) and microcrystalline silicon for which the two methods give equivalent results if proper corrections are applied. Recently also organo-metalhalide perovskites ($CH_3NH_3PbI_3$) were analysed in order to demonstrate very sharp absorption edge (De Wolf et al., 2014) or to study material decomposition. When the material decomposes accompanied by creation of PbI_2 inclusions, photocurrent and photoconductivity may give quite different results. This difference was explained by charge transfer of holes from PbI_2 into $CH_3NH_3PbI_3$ (Holovský et al., 2017).

Apart from photovoltaic absorber materials, materials for transparent conductive windows can also be studied by photothermal spectroscopy. We have studied the validity of thin-film limit on the measureable properties of graphene and found that evaluation of potential beneficial effects of graphene requires different approach than in the case of macroscopic layers. Parasitic absorption of graphene might be significantly reduced when incorporated into medium of high refractive index (Holovský et al., 2015). Conductivity and transparency is the most important properties of the transparent conductive windows. We have studied sub-bandgap absorption also of amorphous InZnO and amorphous ZnSnO window materials and found correlation with its conductivity (Morales-Masis et al., 2015) and some technological parameters (Rucavado et al., 2017). That gave another proof of importance of the sub-bandgap absorption spectroscopy for the photovoltaic technology.

Acknowledgment

Bibliography

Journals:

J. Holovský, S. De Wolf, J. Werner, Z. Remeš, M. Müller, N. Neykova, M. Ledinský, L. Černá, P. Hrzina, P. Löper, B. Niesen, C. Ballif, *Photocurrent Spectroscopy of Perovskite Layers and Solar Cells: A Sensitive Probe of Material Degradation* J. Phys. Chem. Lett. 8 (2017) 838 - 843.

E. Rucavado, Q. Jeangros, D. F. Urban, J. Holovský, Z. Remes, M. Duchamp, F. Landucci, R. E. Dunin-Borkowski, W. Körner, C. Elsässer, A. Hessler-Wyser, M. Morales-Masis, C. Ballif, *Enhancing the optoelectronic properties of amorphous zinc tin oxide by subgap defect passivation: A theoretical and experimental demonstration,* Phys. Rev. B 95 (2017) 245204(1) - 245204(10).

M. Varga, T. Ižák, V. Vretenár, H. Kozak, J. Holovský, A. Artemenko, M. Hulman, V. Skákalová, D.S. Lee, A. Kromka, *Diamond/carbon nanotube composites: Raman, FTIR and XPS spectroscopic studies*, Carbon 111 (2017) 54 - 61.

O. Cibulka, C. Vorkötter, A. Purkrt, J. Holovský, J. Benedikt, K. Herynková, *Comparison of Silicon Nanocrystals Prepared by Two Fundamentally Different Methods*, Nanoscale Res. Lett. 11 (2016) 445 - 445.

S. Morawiec, J. Holovský, M. J. Mendes, M. Müller, K. Ganzerová, A. Vetushka, M. Ledinský, F. Priolo, A. Fejfar, I. Crupi, *Experimental quantification of useful and parasitic absorption of light in plasmon-enhanced thin silicon films for solar cells application*, Sci. Rep. 6 (2016) 22481(1) - 22481(10).

J. Holovský, S. Nicolay, S. De Wolf, C. Ballif, *Effect of the thin-film limit on the measurable optical properties of graphene*, Sci. Rep. 5 (2015) 15684 (1) - 15684 (6).

J. Holovský, S. De Wolf, P. Jiříček, Ch. Ballif, *Attenuated total reflectance Fourier-transform infrared spectroscopic investigation of silicon heterojunction solar cells*, Rev. Sci. Instrum. 86 (2015) 073108-1 - 073108-6.

D. Y. Kim, E. Guijt, F. T. Si, R. Santbergen, J. Holovský, O. Isabella, R. van Swaaij, M. Zeman, *Fabrication of double- and triple-junction solar cells with hydrogenated amorphous silicon oxide (a-SiOx:H) top cell*, Sol. Energ. Mat. Sol. C. 141 (2015) 148 - 153.

M. Ledinský, P. Löper, B. Niesen, J. Holovský, S.-J. Moon, J. Yum, S. De Wolf, A. Fejfar, C. Ballif, *Raman Spectroscopy of Organic–Inorganic Halide Perovskites*, J. Phys. Chem. Lett. 6 (2015) 401 - 406.

P. A. Losio, O. Caglar, J. S. Cashmore, J. E. Hötzel, S. Ristau, J. Holovský, Z. Remeš, I. Sinicco, *Light management in large area thin-film silicon solar modules*,Sol. Energ. Mat. Sol. C. 143 (2015) 375 - 385.

M. Morales-Masis, M. S. De Nicolas, J. Holovský, S. De Wolf, C. Ballif, *Low-Temperature High-Mobility Amorphous IZO for Silicon Heterojunction Solar Cells*, IEEE J. Photovoltaics 5 (2015) 1340 - 1347.

C. Strobel, B. Leszczynska, U. Merkel, J. Kuske, D. D. Fischer, M. Albert, J. Holovský, S. Michard, J. W. Bartha, *High efficiency high rate microcrystalline silicon thin-film solar cells deposited at plasma excitation frequencies larger than 100 MHz*, Sol. Energ. Mat. Sol. C. 143 (2015) 347 - 353.

S. De Wolf, J. Holovsky, S.-J. Moon, P. Löper, B. Niesen, M. Ledinsky, F.-J. Haug, J.-H. Yum, C. Ballif, *Organometallic Halide Perovskites: Sharp Optical*

Absorption Edge and Its Relation to Photovoltaic Performance, J. Phys. Chem. Lett. 5 (2014) 1035 - 1039.

J. Holovský, C. Ballif, *Thin-film limit formalism applied to surface defect absorption*, Opt. Express 22 (2014) 31466 - 31472.

E. El Mhamdi, J. Holovsky, B. Demaurex, C. Ballif, S. De Wolf, *Is light-induced degradation of a-Si:H/c-Si interfaces reversible?*, Appl. Phys. Lett. 104 (2014) 2521081 - 2521084.

P. Loper; B. Niesen, Soo-Jin Moon, S. Martin de Nicolas, J. Holovský, Z. Remeš, M. Ledinský, F.-J. Haug, Jun-Ho Yum, S. De Wolf, C. Ballif, *Organic–Inorganic Halide Perovskites: Perspectives for Silicon-Based Tandem Solar Cells*, IEEE J. Photovoltaics 4 (2014) 1545 - 1551.

Š. Potocký, J. Holovský, Z. Remeš, M. Müller, J. Kočka, A. Kromka, *Si-related color centers in nanocrystalline diamond thin films,* phys. status solidi b 251 (2014) 2603 - 2606.

Neda Neykova, Karel Hruška, Jakub Holovský, Zdeněk Remeš, Milan Vaněček, *Arrays of ZnO nanocolumns for 3-dimensional very thin amorphous and microcrystalline silicon solar cells*, Thin Solid Films 543 (2013) 110 - 113.

G. Bugnon, G. Parascandolo, T. Söderström, P. Cuony, M. Despeisse, S. Hänni, J. Holovský, F. Meillaud, C. Ballif, *A New View of Microcrystalline Silicon: The Role of Plasma Processing in Achieving a Dense and Stable Absorber Material for Photovoltaic Applications*, Adv. Funct. Mater. 22 (2012) 3665 - 3671.

J. Holovský, M. Bonnet-Eymard, M. Boccard, M. Despeisse, C. Ballif, *Variable light biasing method to measure component I-V characteristics of multi-junction solar cells*, Sol. Energ. Mat. Sol. C. 103 (2012) 128 - 133.

J. Holovský, M. Bonnet-Eymard, G. Bugnon, P. Cuony, M. Despeisse, C. Ballif, *Measurement of the open circuit voltage of individual sub-cells in a dual-junction solar cell*, IEEE J. Photovoltaics 2 (2012) 164 - 168.

J. Holovský, M. Schmid, M. Stückelberger, M. Despeisse, C. Ballif, A. Poruba, M. Vaněček, *Time evolution of surface defect states in hydrogenated amorphous silicon studied by photothermal and photocurrent spectroscopy and optical simulation*, J. Non-Cryst. Solids 358 (2012) 2035 - 2038.

A. Descoeudres, L. Barraud, S. De Wolf, B. Strahm, D. Lachenal, C. Guérin, Z. C. Holman, F. Zicarelli, B. Demaurex, J. Seif, J. Holovský, C. Ballif, *Improved amorphous/crystalline silicon interface passivation by hydrogen plasma treatment*, Appl. Phys. Lett. 99 (2011) 123605(1) - 123506(3).

M. Vaněček, O. Babchenko, A. Purkrt, J. Holovsky, N. Neykova, A. Poruba, Z. Remeš, J. Meier, U. Kroll, *Nanostructured three-dimensional thin film silicon solar cells with very high efficiency potential*, Appl. Phys. Lett. 98 (2011) 163503-1 - 163503-3.

J. Červenka, M. Ledinský, H. Stuchlíková, J. Stuchlík, Z. Výborný, J. Holovský, K. Hruška, A. Fejfar, J. Kočka, *Ultrasharp Si nanowires produced by plasma-enhanced chemical vapor deposition*, Phys. Status Solidi-Rapid Res. Lett. 4 (2010) 37 - 39.

J. Holovský, U. Dagkaldiran, Z. Remeš, A. Purkrt, T. Ižák, A. Poruba, and M. Vaněček, *Fourier transform photocurrent measurement of thin silicon films on rough, conductive and opaque substrate*, phys. status solidi a 207 (2010) 578 - 581.

Z. Remeš, J. Holovský, A. Purkrt, T. Ižák, A. Poruba, M. Vaněček, Ü. Dagkaldiran, H. M. Yates, P. Evans, D. W. Sheel, *Optical absorption losses in metal layers used in thin film solar cells*, phys. status solidi a 207 (2010) 2170 - 2173.

J. Holovský, A. Poruba, A. Purkrt, Z. Remeš, M. Vaněček, *Comparison of photocurrent spectra measured by FTPS and CPM for amorphous silicon layers and solar cells*, J. Non-Cryst. Solids 354 (2008) 2167 - 2170.

A. Poruba, J. Holovský, A. Purkrt, M. Vaněček, *Advanced optical characterization of disordered semiconductors by Fourier transform photocurrent spectroscopy*, J. Non-Cryst. Solids 354 (2008) 2421 - 2425.

In press:

F. Ventosinos, J. Klusáček, T. Finsterle, F.-J. Haug, J. Holovský, *Shunt Quenching and Concept of Independent Global Shunt in Multijunction Solar Cells*, Accepted to IEEE Journal of Photovoltiacs. (2017).

J. Jean, T. S. Mahony, D. Bozyigit, M. Sponseller, J. Holovský, M. G. Bawendi, V. Bulović, *Radiative Efficiency Limit with Band Tailing Exceeds 30% for Quantum Dot Solar Cells*, Submitted to Energy & Environmental Science (2017).

Chapter in a book:

Jakub Holovský, *Fourier Transform Photocurrent Spectroscopy on Non-Crystalline Semiconductors, Fourier Transforms* - New Analytical Approaches and FTIR Strategies, Goran Nikolic (Ed.), ISBN: 978-953-307-232-6, InTech, (2011) Available at: http://www.intechopen.com/articles/show/title/fourier-transform-photocurrent-spectroscopy-on-non-crystalline-semiconductors

Conference proceedings:

N. Abolmasov, H. Woo, R. Planques,J. Holovský, E. V. Johnson, A. Purkrt, P. Roca i Cabarrocas, *Substrate and p-layer effects on polymorphous silicon solar cells* EPJ Photovoltaics 5 (2014) Topical issue of Photovoltaic Technical Conference 2013, p 55206

J. Holovský, Z. Remeš, S. De Wolf, C. Ballif, *Surface and ultrathin-layer absorptance spectroscopy for solar cells*, Energy Procedia 60, Proceeding of E-MRS Spring Meeting 2014 Symposium Y, Lille, France (2014) 57 – 62

N. Neykova, Z. Remeš, J. Holovský, A. Purkrt, K. Hruška, M. Vaněček, J. Meier, U. Kroll, *ZnO nanostructures (columns, cones, rods) for highly efficient thin film silicon solar cells* E-MRS 2011 Spring Meeting, Nice, France, 9-13 May 2011

M. Vaněček, N. Neykova, O. Babchenko, A. Purkrt, A. Poruba, Z. Remeš, J. Holovský, K. Hruška, J. Meier, U. Kroll, *New 3-dimensional nanostructured thin film silicon solar cells,* Proceedings of the 25th EU-PVSEC/ 5th WCPEC, 6-10 September 2010 Valencia, Spain, pp. 2763-2766, ISBN: 3-936338-26-4.

M. Vaněček, A. Poruba, Z. Remeš, J. Holovský, A. Purkrt, O. Babchenko, K. Hruška, J. Meier, U. Kroll, *Five Roads towards Increased Optical Absorption and High Stable Efficiency for Thin Film Silicon Solar Cells ,* Proceedings of the 24th EU-PVSEC, 21-25 September 2009, Hamburg, Germany, pp. 2286 - 2289, ISBN: 3-936338-25-6

J. Holovský, M. Vaněček , *Non-destructive technique to measurement and separation of I-V curves of monolithic multi-junction solar cells ,* Proceedings of the 24th EU-PVSEC, 21-25. September 2009, Hamburg, Germany, pp. 2757-9, ISBN 3-936338-25-6

M. Vaneček, A. Poruba, Z. Remes, J. Holovský, A. Purkrt, O. Babchenko, K. Hruška, J. Meier, U. Kroll, *Five roads towards increased optical absorption and high stable efficiency for thin film silicon solar cells ,* Proceedings of the 24th EU-PVSEC, 21-25. September 2009, Hamburg, Germany, pp. 2286-9, ISBN 3-936338-25-6

J. Holovský, A. Purkrt, A. Poruba, Z. Remeš, M. Vaněček, D. Semerel, A. Borreman, E. Hamers,F. Finger, U. Dagkaldiran, H. Yates, *Comprehensive study of single amorphous and tandem micromorph solar cells and modules on flexible aluminum superstrate prepared in roll-to-roll process,* Proceedings of the 23rd EU-PVSEC, 1-5 September 2008, Valencia, Spain, pp. 2309-2312, ISBN: 3-936338-24-8

A. Poruba, P. Klapetek, J. Holovský, A. Purkrt, M. Vaněček , *Experimental limits of light capture in thin film silicon devices ,* Materials Research Society Symposium Proceedings 1101, pp. 143-154

J. Holovský, A. Poruba, J. Bailat, M. Vaněček, *Separation of signals from amorphous and microcrystalline part of a tandem thin film silicon solar cell in Fourier transform photocurrent spectroscopy,* Proceedings of the 22nd EU-PVSEC, Milan, Italy, 3-7 September 2007, pp. 1851-1854, ISBN: 3-936338-22-1

J. Holovský, A. Poruba, J. Bailat, M. Vaněček, *Separation of signals from amorphous and microcrystalline part of a tandem thin film silicon solar cell in Fourier Transform Photocurrent Spectroscopy,* Proceeding of NUMOS, Gent, Belgium, 28-30 March 2007, pp. 249-255, ISBN: 978-90-382-1109-1

J. Holovsky, A. Poruba, J. Toušek, J. Toušková, R. Bařinka, M. Vaněček, *Fast detection of surface recombination velocity and diffusion length for non-symmetrical c-Si structures,* Proceedings of the 21st EU-PVSEC, Dresden, Germany, 4-8 September 2006, pp. 1408-1411, ISBN: 3-936338-20-5

A. Poruba, L. Hoďáková, A. Purkrt, J. Holovský, M. Vaněček, *Fast Quantum Efficiency Measurement and Characterization of Different Thin Film Solar Cells by Fourier Transform Photocurrent Spectroscopy* Conference Record of the 2006 IEEE 4th WCPEC, IEEE, 2006, pp.1525-1528. ISBN: 1-4244-0017-1

References

Alsema, E.A., de Wild-Scholten, M.J., 2007. Reduction of the envoronmental impact in crystaline silicon manufacturing production., in: Proceedings of the 22nd EU-PVSEC. Milano.

Beckmann, P., Spizzichino, A., 1963. Scattering of Electromagnetic Waves from Rough Surfaces. Pergamon, London.

Bittkau, K., Schulte, M., Klein, M., Beckers, T., Carius, R., 2011. Modeling of light scattering properties from surface profile in thin-film solar cells by Fourier transform techniques. Thin Solid Films 519, 6538–6543. doi:10.1016/j.tsf.2011.04.122

Boccara, A.C., Fournier, D., Badoz, J., 1980. Thermo-optical spectroscopy: Detection by the ''mirage effect''. Applied Physics Letters 36, 130. doi:10.1063/1.91395

Born, M., Wolf, E., 1998. Principles of optics (Sixth edition). Cambridge University Press.

Brendel, R., 1991. The concept of effective film thickness for the determination of bond concentrations from IR spectra of weakly absorbing thin films on silicon. Journal of Applied Physics 69, 7395–7399. doi:10.1063/1.347552

Brivio, F., Walker, A.B., Walsh, A., 2013. Structural and electronic properties of hybrid perovskites for high-efficiency thin-film photovoltaics from first-principles. APL Materials 1, 42111. doi:10.1063/1.4824147

Burschka, J., Pellet, N., Moon, S.-J., Humphry-Baker, R., Gao, P., Nazeeruddin, M.K., Grätzel, M., 2013. Sequential deposition as a route to high-performance perovskite-sensitized solar cells. Nature 499, 316–319. doi:10.1038/nature12340

Čampa, A., Isabella, O., van Erven, R., Peeters, P., Borg, H., Krč, J., Topič, M., Zeman, M., 2010. Optimal design of periodic surface texture for thin-film a-Si:H solar cells. Progress in Photovoltaics: Research and Applications 18, 160–167. doi:10.1002/pip.940

De Wolf, S., Holovsky, J., Moon, S.-J., Löper, P., Niesen, B., Ledinsky, M., Haug, F.-J., Yum, J.-H., Ballif, C., 2014. Organometallic Halide Perovskites: Sharp Optical Absorption Edge and Its Relation to Photovoltaic Performance. The Journal of Physical Chemistry Letters 5, 1035–1039. doi:10.1021/jz500279b

Dimroth, F., Tibbits, T.N.D., Niemeyer, M., Predan, F., Beutel, P., Karcher, C., Oliva, E., Siefer, G., Lackner, D., Fus-Kailuweit, P., Bett, A.W., Krause, R., Drazek, C., Guiot, E., Wasselin, J., Tauzin, A., Signamarcheix, T., 2016. Four-Junction Wafer-Bonded Concentrator Solar Cells. IEEE Journal of Photovoltaics 6, 343–349. doi:10.1109/JPHOTOV.2015.2501729

Fraunhofer ISE 2017, 'Photovoltaics-Report.pdf' [Online]. Available: https://www.ise.fraunhofer.de/content/dam/ise/de/documents/publications/studies/Photovoltaics-Report.pdf [Accessed: 07-Sep-2017]

Frost, J.M., Butler, K.T., Brivio, F., Hendon, C.H., van Schilfgaarde, M., Walsh, A., 2014. Atomistic Origins of High-Performance in Hybrid Halide Perovskite Solar Cells. Nano Letters 14, 2584–2590. doi:10.1021/nl500390f

Green, M.A., Pillai, S., 2012. Harnessing plasmonics for solar cells. Nature Photonics 6, 130–132. doi:10.1038/nphoton.2012.30

Haase, C., Stiebig, H., 2006. Optical properties of thin-film silicon solar cells with grating couplers. Progress in Photovoltaics: Research and Applications 14, 629–641. doi:10.1002/pip.694

Hishikawa, Y., Nakamura, N., Tsuda, S., Nakano, S., Kishi, Y., Kuwano, Y., 1991. Interference-Free Determination of the Optical Absorption Coefficient and the Optical Gap of Amorphous Silicon Thin Films. Japanese Journal of Applied Physics 30, 1008–1014. doi:10.1143/JJAP.30.1008

Holovský, J., 2011. Fourier Transform Photocurrent Spectroscopy on Non-Crystalline Semiconductors, in: Fourier Transforms - New Analytical Approaches and FTIR Strategies. InTech Publishing, pp. 257–282.

Holovský, J., Ballif, C., 2014. Thin-film limit formalism applied to surface defect absorption. Optics Express 22, 31466. doi:10.1364/OE.22.031466

Holovský, J., Dagkaldiran, Ü., Remeš, Z., Purkrt, A., Ižák, T., Poruba, A., Vaněček, M., 2010. Fourier transform photocurrent measurement of thin silicon films on rough, conductive and opaque substrates. physica status solidi (a) 207, 578–581. doi:10.1002/pssa.200982890

Holovský, J., De Wolf, S., Werner, J., Remeš, Z., Müller, M., Neykova, N., Ledinský, M., Černá, L., Hrzina, P., Löper, P., Niesen, B., Ballif, C., 2017. Photocurrent Spectroscopy of Perovskite Layers and Solar Cells: A Sensitive Probe of Material Degradation. The Journal of Physical Chemistry Letters 8, 838–843. doi:10.1021/acs.jpclett.6b02854

Holovský, J., Nicolay, S., De Wolf, S., Ballif, C., 2015. Effect of the thin-film limit on the measurable optical properties of graphene. Scientific Reports 5, 15684. doi:10.1038/srep15684

Holovský, J., Poruba, A., Purkrt, A., Remeš, Z., Vaněček, M., 2008. Comparison of photocurrent spectra measured by FTPS and CPM for amorphous silicon layers and solar cells. Journal of Non-Crystalline Solids 354, 2167–2170. doi:10.1016/j.jnoncrysol.2007.09.106

Holovský, J., Schmid, M., Stuckelberger, M., Despeisse, M., Ballif, C., Poruba, A., Vaněček, M., 2012. Time evolution of surface defect states in hydrogenated amorphous silicon studied by photothermal and photocurrent spectroscopy and optical simulation. Submitted to Journal of Non-Crystalline Solids.

Jackson, W., Amer, N., 1982. Direct measurement of gap-state absorption in hydrogenated amorphous silicon by photothermal deflection spectroscopy. Physical Review B 25, 5559–5562. doi:10.1103/PhysRevB.25.5559

Jean, J., Mahony, T.S., Bozyigit, D., Sponseller, M., Holovský, J., Bawendi, M.G., Bulović, V., 2017. Radiative Efficiency Limit with Band Tailing Exceeds 30% for Quantum Dot Solar Cells. submitted.

Jongbloets, H., Stoelinga, J., van de Steeg, M., Wyder, P., 1979. Temperature dependence of the photothermal conductivity of high-purity germanium containing very low concentrations of Al, B, and P. Physical Review B 20, 3328–3332. doi:10.1103/PhysRevB.20.3328

Klapetek, P., Valtr, M., Poruba, A., Nečas, D., Ohlídal, M., 2010. Rough surface scattering simulations using graphics cards. Applied Surface Science 256, 5640–5643. doi:10.1016/j.apsusc.2010.03.028

Koida, T., Fujiwara, H., Kondo, M., 2007. Hydrogen-doped In_2O_3 as High-mobility Transparent Conductive Oxide. Japanese Journal of Applied Physics 46, L685–L687. doi:10.1143/JJAP.46.L685

Krč, J., Zeman, M., Smole, F., Topič, M., 2004. Optical modelling of thin-film silicon solar cells deposited on textured substrates. Thin Solid Films 451–452, 298–302. doi:10.1016/j.tsf.2003.11.030

Lanz, T., Ruhstaller, B., Battaglia, C., Ballif, C., 2011. Extended light scattering model incorporating coherence for thin-film silicon solar cells. Journal of Applied Physics 110, 33111. doi:10.1063/1.3622328

Leblanc, F., Perrin, J., Schmitt, J., 1994. Numerical modeling of the optical properties of hydrogenated amorphous-silicon-based p-i-n solar cells deposited on rough transparent conducting oxide substrates. Journal of Applied Physics 75, 1074. doi:10.1063/1.356489

Ledinský, M., Löper, P., Niesen, B., Holovský, J., Moon, S.-J., Yum, J.-H., De Wolf, S., Fejfar, A., Ballif, C., 2015. Raman Spectroscopy of Organic–Inorganic Halide Perovskites. The Journal of Physical Chemistry Letters 6, 401–406. doi:10.1021/jz5026323

Main, C., Reynolds, S., Zrinščak, I., Mergaza, A., 2004. Comparison of AC and DC constant photocurrent methods for determination of defect densities. Journal of Non-Crystalline Solids 338–340, 228–231. doi:10.1016/j.jnoncrysol.2004.02.059

Morales-Masis, M., Martin De Nicolas, S., Holovsky, J., De Wolf, S., Ballif, C., 2015. Low-Temperature High-Mobility Amorphous IZO for Silicon Heterojunction Solar Cells. IEEE Journal of Photovoltaics 1340–1347. doi:10.1109/JPHOTOV.2015.2450993

Morawiec, S., Holovský, J., Mendes, M.J., Müller, M., Ganzerová, K., Vetushka, A., Ledinský, M., Priolo, F., Fejfar, A., Crupi, I., 2016. Experimental quantification of useful and parasitic absorption of light in plasmon-enhanced thin silicon films for solar cells application. Scientific Reports 6, 22481. doi:10.1038/srep22481

Morgado, E., 2001. Defect-related photoinduced absorption in amorphous silicon. Physica B: Condensed Matter 308–310, 174–177. doi:10.1016/S0921-4526(01)00685-8

Naqavi, A., Söderström, K., Haug, F.-J., Paeder, V., Scharf, T., Herzig, H.P., Ballif, C., 2010. Understanding of photocurrent enhancement in real thin film solar cells: towards optimal one-dimensional gratings. Optics Express 19, 128. doi:10.1364/OE.19.000128

Noh, J.H., Im, S.H., Heo, J.H., Mandal, T.N., Seok, S.I., 2013. Chemical Management for Colorful, Efficient, and Stable Inorganic–Organic Hybrid Nanostructured Solar Cells. Nano Letters 130321112645008. doi:10.1021/nl400349b

NREL 2017, 'efficiency-chart.png' [Online]. Available: https://www.nrel.gov/pv/assets/images/efficiency-chart.png [Accessed: 07-Sep-2017]

PVXCHANGE 2017, Price Index [Online]. Available: http://www.pvxchange.com/priceindex/Default.aspx?langTag=en-GB [Accessed: 07-Sep-2017]

Python, M., 2009. Microcrystalline silicon solar cells: growth and defects (PhD thesis). Université de Neuchâtel, Neuchâtel.

Ritter, D., Weiser, K., 1986. Suppression of interference fringes in absorption measurements on thin films. Optics Communications 57, 336–338. doi:10.1016/0030-4018(86)90270-1

Rucavado, E., Jeangros, Q., Urban, D.F., Holovský, J., Remes, Z., Duchamp, M., Landucci, F., Dunin-Borkowski, R.E., Körner, W., Elsässer, C., Hessler-Wyser, A., Morales-Masis, M., Ballif, C., 2017. Enhancing the optoelectronic properties of amorphous zinc tin oxide by subgap defect passivation: A theoretical and experimental demonstration. Physical Review B 95. doi:10.1103/PhysRevB.95.245204

Santbergen, R., van Zolingen, R.J.C., 2008. The absorption factor of crystalline silicon PV cells: A numerical and experimental study. Solar Energy Materials and Solar Cells 92, 432–444. doi:10.1016/j.solmat.2007.10.005

Schulte, M., Bittkau, K., Pieters, B.E., Jorke, S., Stiebig, H., Hüpkes, J., Rau, U., 2011. Ray tracing for the optics at nano-textured ZnO-air and ZnO-silicon interfaces. Progress in Photovoltaics: Research and Applications 19, 724–732. doi:10.1002/pip.1097

Shockley, W., Queisser, H.J., 1961. Detailed Balance Limit of Efficiency of p-n Junction Solar Cells. Journal of Applied Physics 32, 510–519. doi:10.1063/1.1736034

Sládek, P., Thèye, M.L., 1994. Analysis of the AC-DC discrepancies in CPM experiments on hydrogenated amorphous silicon. Solid State Communications 89, 199–203. doi:10.1016/0038-1098(94)90682-3

Springer, J., Poruba, A., Vanecek, M., 2004. Improved three-dimensional optical model for thin-film silicon solar cells. Journal of Applied Physics 96, 5329. doi:10.1063/1.1784555

Street, R.A., 1991. Hydrogenated amorphous silicon. Cambridge University Press.

Strobel, C., Leszczynska, B., Merkel, U., Kuske, J., Fischer, D.D., Albert, M., Holovský, J., Michard, S., Bartha, J.W., 2015. High efficiency high rate microcrystalline silicon thin-film solar cells deposited at plasma excitation frequencies larger than 100MHz. Solar Energy Materials and Solar Cells 143, 347–353. doi:10.1016/j.solmat.2015.07.014

Tomm, J.W., Jaeger, A., Bärwolff, A., Elsaesser, T., Gerhardt, A., Donecker, J., 1997. Aging properties of high power laser diode arrays analyzed by Fourier-transform photocurrent measurements. Applied Physics Letters 71, 2233. doi:10.1063/1.120066

Urbach, F., 1953. The Long-Wavelength Edge of Photographic Sensitivity and of the Electronic Absorption of Solids. Physical Review 92, 1324–1324. doi:10.1103/PhysRev.92.1324

Vandewal, K., Tvingstedt, K., Gadisa, A., Inganäs, O., Manca, J.V., 2009. On the origin of the open-circuit voltage of polymer–fullerene solar cells. Nature Materials 8, 904–909. doi:10.1038/nmat2548

Vaněček, M., Kočka, M., Stuchlík, J., Tříska, J., 1981. Direct measurement of the gap states and band tail absorption by constant photocurrent method in amorphous silicon. Solid State Communications 39, 1199–1202. doi:10.1016/0038-1098(81)91113-3

Vanecek, M., Poruba, A., 2002. Fourier-transform photocurrent spectroscopy of microcrystalline silicon for solar cells. Applied Physics Letters 80, 719–721. doi:10.1063/1.1446207

Weber, J.W., Bol, A.A., van de Sanden, M.C.M., 2014. An improved thin film approximation to accurately determine the optical conductivity of graphene from infrared transmittance. Applied Physics Letters 105, 13105. doi:10.1063/1.4889852

Wyrsch, N., Finger, F., Mcmahon, T., Vanecek, M., 1991. How to reach more precise interpretation of subgap absorption spectra in terms of deep defect density in a-Si:H. Journal of Non-Crystalline Solids 137–138, 347–350. doi:10.1016/S0022-3093(05)80127-9

Yang, W.S., Park, B.-W., Jung, E.H., Jeon, N.J., Kim, Y.C., Lee, D.U., Shin, S.S., Seo, J., Kim, E.K., Noh, J.H., Seok, S.I., 2017. Iodide management in formamidinium-lead-halide–based perovskite layers for efficient solar cells. Science 356, 1376–1379. doi:10.1126/science.aan2301

Comparison of photocurrent spectra measured by FTPS and CPM for amorphous silicon layers and solar cells

J. Holovský[a], A. Poruba[a,b], A. Purkrt[a], Z. Remeš [a], and M. Vaněček[a]

[a] *Institute of Physics, Academy of Sciences of the Czech Republic, Cukrovarnická 10, 162 53 Prague 6, Czech Republic*
[b] *Solartec s.r.o., Televizní 2618, 756 61 Rožnov pod Radhoštěm, Czech Republic*

Abstract

Fourier Transform Photocurrent Spectroscopy (FTPS) has been recently introduced as a fast and highly sensitive method for the evaluation of the optical absorption coefficient of photoconductive thin films such as microcrystalline silicon layers. This contribution represents the first study of FTPS utilization for amorphous silicon layers and cells. FTPS spectra are compared with results of Constant Photocurrent Method (CPM) and Dual Beam Photoconductivity (DBP) measured at different chopping frequencies. We will concentrate to highlight the appropriate measuring conditions and evaluation procedures for correct data interpretation. Moreover, we will present our novel approach for the interference free determination of absorption coefficients of thin films grown on transparent substrates which is mainly important for very thin layers where broad interference fringes do not allow correct evaluation of parameters such as a slope of the Urbach tail and the defect density.

1. Introduction

The thin film silicon technology is now already mastered and it is becoming one of the most promising branches in present photovoltaic industry. Fast quality monitoring of an absorber layer seems to be an important requirement for industry to keep the high yield and speed of technology process. Recently we have introduced a fast and highly sensitive method for the evaluation of the optical absorption coefficient of photoconductive thin films such as microcrystalline silicon layers [1] and later also for the quality assessment of thin film silicon solar cells [2]. High accuracy and reproducibility of this method, Fourier Transform Photocurrent Spectroscopy (FTPS), has also been demonstrated by interpreting the measured FTPS spectra of solar cells (single or tandem) as the external quantum efficiency data [3].

From a historical view, the Constant Photocurrent Method (CPM) was introduced 25 years ago especially for the optical characterization of thin films of amorphous hydrogenated silicon where the lifetime has to be fixed during the spectroscopic measurement at the constant value. This condition cannot be guaranteed for the FTPS measurement where the "whole" photocurrent spectrum is calculated by Fourier transform from time domain photocurrent signal scanned under time changing light spectrum by Michelson's interferometer.

In this contribution we will show how the FTPS, CPM and DBP (Dual Beam Photoconductivity) spectra differ as well as the conditions under which they reach similar values of deep defect density and Urbach slope in amorphous silicon layers and cells. Moreover, we will present our novel approach for the interference free determination of sub-gap absorption coefficient which is important for very thin layers where slow, broad interference fringes do not allow direct correct evaluation of parameters such as a slope of the Urbach tail or the defect density.

2. Experimental

Fourier Transform Photocurrent Spectroscopy (FTPS) utilizes Fourier

Transform InfraRed (FTIR) spectrometer with the facility to connect an external detector. The measured sample, i.e., a photoconductive film or solar cell can be illuminated by FTIR beam either in the spectrometer sample compartment or outside the spectrometer using the option of the "external light beam output" (this is necessary for large samples or PV modules). In our case, a thin film or solar cell connected into an electrical circuit with current preamplifier (and eventually with a bias-voltage source) serves as the external detector. FTPS single beam signal is limited by the dynamic range of A/D converter. To overcome this problem and reach the final dynamic range of 6 to 8 orders of magnitude, we divide the spectral range to particular measurements with various optical filters. We use different sets of optical filters (long pass or band pass) for the diagnostics of various materials. Thus, the final FTPS spectrum is usually assembled from two or three partly overlapping parts where different optical filters were used. More details about this method as well as the description of the experimental set-up can be found in [4].

Finally, the measured and evaluated FTPS spectra are compared with the results of CPM and DBP where different chopping frequencies were used for the measurement.

We have applied three photocurrent methods mentioned above to characterize two amorphous silicon thin films and two solar cells, where all silicon films were produced by RF or VHF PE CVD from a silane – hydrogen mixture. All results of thin films on glass substrates are plotted not as the absorptance A, but by our new approach for the interference free determination of optical absorption coefficient as the A/T ratio.

There are two possibilities how to receive this quantity. In the first one a sample can be placed in an "open" holder in the spectrometer sample compartment and we can detect photocurrent spectrum of the sample and, by inner thermoelectrically cooled DTGS (deuterated triglicide sulphate) detector, also the signal proportional to the spectrometer baseline multiplied by the sample transmittance. Measurement without the sample (by the same detector) gives the baseline itself.

The other set-up utilizes another piece of the same film as the optical filter placed very close to the measured sample itself. By the

measurement of the FTPS signal with and without this filter, we can obtain both A and T. Fig. 1 shows the absorptance A fixed to the units of absorption coefficient (squares), the transmittance T (circles), the "AT" product as the result of FTPS measured with another piece of the same sample used as an optical filter (triangles) and the calculated, interference free A/T ratio (in relative units - stars) from which (after setting it to the absolute scale) one can determine the spectral dependence of the absorption coefficient α by Ritter-Weiser formula [5]. Both A/T and α quantities have the same shape in the low absorption range where $\alpha.d < 1$.
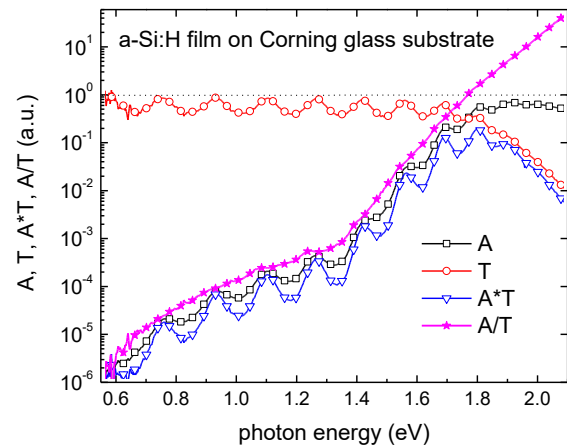
Fig.1 Various spectra of the a-Si:H thin film measured and evaluated using interference free FTPS set-up, absorptance A as a standard FTPS result (squares), "AT" product when FTPS is measured with another piece of the same sample as an optical filter (triangles) and from these spectra calculated transmittance T (circles) and quantity A/T (stars).

3. Experimental results

All FTPS data presented in this section represent final photocurrent spectra where each curve has been assembled from two or three parts measured with different optical filters and after all other corrections mentioned above and in [6]. FTPS spectra measured at standard conditions and under the white light bias (from a halogen lamp) are compared with results of the standard and white light biased CPM and also with data of DBP scanned at different frequencies. In all light biased experiments we kept the bias light intensity constant, so that the DC photocurrent in layers was about 3 orders of magnitude higher than the dark current.

3.1. FTPS characterization of a-Si:H thin films

Measurements were done for two a-Si:H films grown on low-alkaline non-absorbing substrate. The thickness of the first layer was around 2 μm while the second sample is only 300 nm thin. Photocurrent was measured in a coplanar geometry (gap 1 x 6 mm) with pasted colloidal graphite electrodes and with applied DC voltage of 80-200 V.

Fig.2 shows the comparison of photocurrent spectra measured by FTPS and CPM under similar conditions (with and without white light bias) for the thicker a-Si:H sample.
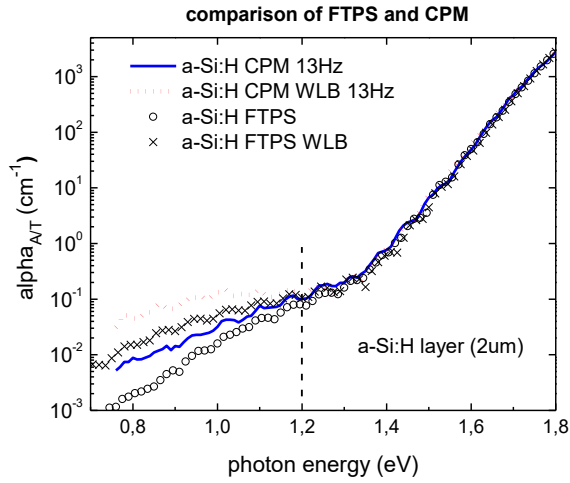
Fig.2 Comparison of photocurrent spectra of 2 μm thick a-Si:H sample measured with and without white light bias (WLB) by FTPS and CPM.

Although the FTPS spectra do not match precisely the CPM results (measured at chopping frequency 13 Hz) at otherwise similar
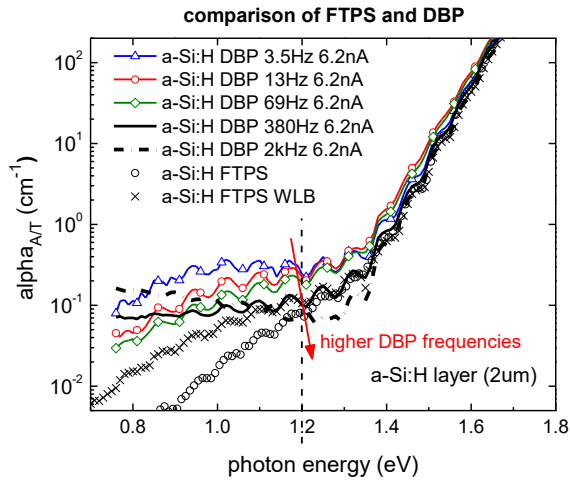
Fig.3 Comparison of photocurrent spectra of 2 μm thick a-Si:H sample measured by FTPS with and without white light bias (WLB) and DBP results measured at 5 different frequencies.

conditions (with or without the white light bias) we observe (quite expectable) changes in the defect related absorption range due to the shift of demarcation levels and thus the change of defect occupation with light bias. There is one more difference in FTPS and CPM. While CPM is measured at constant chopping frequency (here 13 Hz), Fourier frequency is about 2-3 kHz in the defect connected region. Therefore in Fig.3 we compare the same FTPS spectra with DBP results measured at various chopping frequencies.

Fig.4 shows the comparison of FTPS and CPM photocurrent spectra (again with and without white light bias) for the thinner a-Si:H sample. We can observe very similar behavior of spectra as in Fig.2.
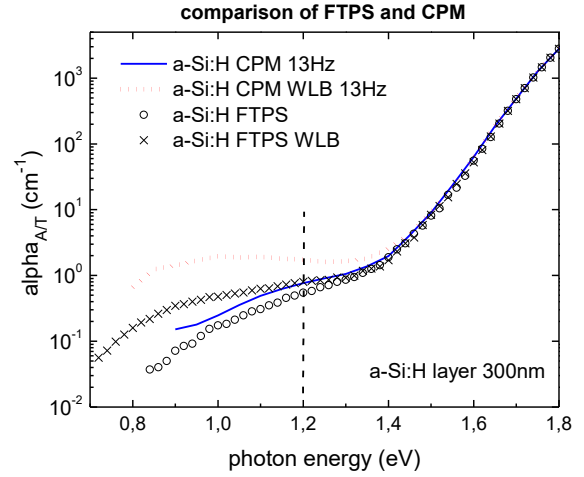

Fig.4 Comparison of photocurrent spectra of 300 nm thin a-Si:H sample measured with and without white light bias (WLB) by FTPS and CPM.

3.2. FTPS characterization of a-Si:H solar cells

We measured optical properties of two a-Si:H solar cells again by FTPS, CPM and DBP. Both cells are nearly of the same thickness about 300 nm and also measured data are very similar. Moreover, there is nearly no difference in spectra when samples are light biased compared to the standard measuring conditions (deviation is within 10% which also represents precision of the photocurrent methods.) Therefore, we present data of one cell only. Fig.5 shows the comparison of standard CPM and FTPS spectra with DBP results measured at three different frequencies. In this case, a small discrepancy between CPM and FTPS results can be well explained as the frequency

dependence because the DBP signal increases in the defect connected region for higher chopping frequencies. The "apparent" α is influenced by light trapping due to rough TCO and by lower transparency of TCO in the infrared; for a quantitative analysis look at [5].
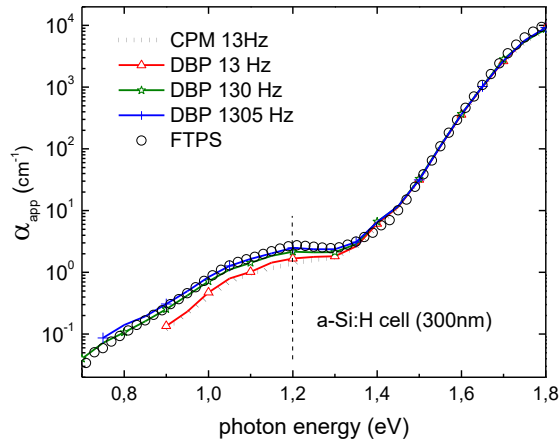
Fig.5 Comparison of FTPS and CPM spectra with DBP results measured at three various chopping frequencies for a single junction a-Si:H cell.

4. Discussion

Comparison of FTPS and CPM results for a-Si:H layers and cells has been done. While FTPS spectra underestimate CPM results (in the defect connected absorption range) in case of layers by a factor of two, we observe just opposite behavior for the amorphous silicon solar cells. An experiment with changing chopping frequency in DBP can explain the discrepancy in case of sandwich structures but not for coplanar geometry measurement, where at higher frequencies we observe the change of the phase shift of the signal in the defect related region.

The phenomena observed in a-Si:H thin film CPM and FTPS spectra are in good agreement with [7] where results of DC and AC CPM (measured at various chopping frequencies) are compared and differences explained on the basis of theoretical modeling.

In case of p-i-n structures, there should be a dominant effect of the internal electric field that varies the position of quasi - Fermi levels and defect state occupation over the cell thickness. Nearly no difference between standard and light biased photocurrent spectra supports this idea.

5. Conclusions

Results of Fourier transform photocurrent spectroscopy, FTPS, were presented for amorphous silicon thin films and solar cells and spectra were compared with CPM and DBP results. Although all photocurrent spectra do not match precisely in the whole measured range, agreement in the exponential region and at 1.2 eV (used for the defect density determination) is quite good. We conclude that FTPS can be used for the fast and reliable quantitative assessment of amorphous silicon active PV layers, both in the thin film and solar cell configuration.

References

[1] M. Vanecek, A. Poruba, Applied Physics Letters 80 (2002) 719.

[2] A. Poruba, M. Vaněček, J. Meier, A. Shah, Journal of Non-Crystalline Solids 299-302 (2002) 536-540.

[3] L. Hodakova, A. Poruba, R. Kravets, M. Vanecek, Journal of Non-Crystalline Solids 352 (2006) 1221-1224.

[4] A. Poruba, R. Bařinka, P. Čech, R. Kravets, L. Hoďáková, M. Vanecek, A. Fejfar, in:, 20th EU-PVSEC, Barcelona, 2005, pp. 240-243.

[5] D. Ritter, K. Weiser, Optics Communications 57 (1986) 336-338.

[6] M. Vanecek, A. Poruba, Thin Solid Films 515 (2007) 7499-7503.

[7] C. Main, S. Reynolds, I. Zrinščak, A. Mergaza, Journal of Non-Crystalline Solids 338-340 (2004) 228-231.

SCIENTIFIC REPORTS

Effect of the thin-film limit on the measurable optical properties of graphene

Jakub Holovský[1,2], Sylvain Nicolay[3], Stefaan De Wolf[3] & Christophe Ballif[3]

The fundamental sheet conductance of graphene can be directly related to the product of its absorption coefficient, thickness and refractive index. The same can be done for graphene's fundamental opacity if the so-called thin-film limit is considered. Here, we test mathematically and experimentally the validity of this limit on graphene, as well as on thin metal and semiconductor layers. Notably, within this limit, *all* measurable properties depend only on the *product* of the absorption coefficient, thickness, and refractive index. As a direct consequence, the absorptance of graphene depends on the refractive indices of the surrounding media. This explains the difficulty in determining separately the optical constants of graphene and their widely varying values found in literature so far. Finally, our results allow an accurate estimation of the potential optical losses or gains when graphene is used for various optoelectronic applications.

The discovery of free-standing graphene[1] opened the fascinating field of two-dimensional material physics[2-5]. Since then, graphene's transparency and exceptionally high carrier mobility have promised to revolutionize the field of thin-film optoelectronics[6-10]. Concerning the optical properties of graphene, the so-called thin-film limit (TFL) or thin-film approximation, obtained by taking the zero-thickness limit in classical formulae for the optical absorptance A, reflectance R and transmittance T, is frequently discussed[3,4,11-14]. Apart from graphene, the TFL has found applications in a variety of characterization methods, including differential reflectance spectrometry[15] and infrared spectroscopy[16,17], as well as in polarimetry of very thin layers[18] and low absorptance spectroscopy[19]. In contrast to ultrathin atomic layers, their thicker counterparts requiring classical Fresnel formulae will be hereafter called macroscopically-thin layers. The remarkable consequences of the TFL appear if the layer is optically parameterized by its absorption coefficient a, thickness d and refractive index n[15,16,18,19]: (i) The measurable optical properties A, R and T do not depend on the parameters a, d or n individually, but only on their product adn. (ii) There is no dependency on the wavelength either, except through the dependencies of the parameters themselves. This explains why in the case of graphene—the thin film *par excellence*—considerable disagreement exists over the measured individual optical parameters[20-24], and why there is some freedom in choice of assumed parameters, e.g. taking the diameter of valence orbitals or spacing of atomic planes in graphite as the thickness of graphene $d_{graphene} = 0.335$ nm[22,23,25-27], or equaling its refractive index to that of graphite $n_{graphite} = 2.52$[21,22,25]. Actually, as argued by Chabal[17], for an atomic monolayer, the thickness d and dielectric function ε lose their usual physical meaning and must rather be defined as tensors, relating to each other as $(\vec{\varepsilon} - 1) \cdot \vec{d} = 4\pi N\vec{\rho}$. Here, the only parameters with physical meaning are N and $\vec{\rho}$, which are the dipole density and the vector of polarizability, respectively. Similarly, as shown already by Drude, the optical properties of an ultrathin film depend only on integral values of its dielectric function over the film thickness[28]. It was pointed out by Bruna and Borini[21]

[1]Institute of Physics of the Academy of Sciences of the Czech Republic, Cukrovarnická 10, 162 00 Praha, Czech Republic. [2]CTU in Prague, Faculty of Electrical Engineering, Technická 2, 166 27 Prague, Czech Republic. [3]École Polytechnique Fédérale de Lausanne (EPFL), Institute of Microengineering (IMT), Photovoltaics and Thin-Film Electronics Laboratory, Maladière 71, CH-2000 Neuchâtel, Switzerland. Correspondence and requests for materials should be addressed to J.H. (email: holovsky@fzu.cz)

that reflectance measurements of graphene can be—under some approximations—reproduced with an arbitrarily pre-defined value of constant refractive index.

The graphene's *adn* product has been related to the fundamental sheet conductance $G_{graphene} \cong e^2/4\hbar$ (*e* being the electron charge and $\hbar$ the reduced Planck constant)[3] by using the relation $2nk = \text{Im}(\varepsilon/\varepsilon_0) = \sigma/\varepsilon_0\omega$, where $\sigma = G/d$ is the conductance, ω the angular frequency, ε_0 the vacuum permittivity and $k = a\lambda/4\pi$ the extinction coefficient:

$$adn = G/\varepsilon_0 c \qquad (1)$$

where *c* is the speed of light in vacuum. For graphene we obtain:

$$(adn)_{graphene} \cong e^2/4\varepsilon_0\hbar c = 0.0229253 \qquad (2)$$

To analyze the effect of the TFL on graphene we take equations recently derived[19], based on the conservation of energy, the continuity of the parallel components of an electric field across the layer, and the assumptions of a low-absorption medium ($k << n$) and a small thickness ($ad << 1$, $dn << \lambda$). For perpendicular incidence, the following equations hold for absorptance A_{TFL}, reflectance R_{TFL} and transmittance T_{TFL} of a layer between two media:

$$A_{\text{TFL}} = \frac{4adnn_0}{(n_0 + n_2 + adn)^2} \qquad (3)$$

$$R_{\text{TFL}} = \frac{(n_0 - n_2 - adn)^2}{(n_0 + n_2 + adn)^2} \qquad (4)$$

$$T_{\text{TFL}} = \frac{4n_0 n_2}{(n_0 + n_2 + adn)^2} \qquad (5)$$

Here, n_0, n_2 indicate respectively the refractive indices of the media over- and underlying the graphene layer. These equations can be converted to the ones typically found in literature, by normalization to the transmittance of the bare substrate[11,14], by setting $n_2 = 1$, using sheet conductance *G* and vacuum impedance $Z_0 = \sqrt{\mu_0/\varepsilon_0}$[12,13] or by setting $n_0 = n_2 = 1$ (i.e. a freestanding layer in air)[3,4].

Results

We first numerically investigate the range of validity of the TFL by comparison to rigorous Fresnel formulae. Figure 1 shows contour plots between which the error of TFL is less than 10% or 1%. The abscissae display the spectral dependence in photon energy; its logarithmic scale deliberately extended to 10 eV to show more complete picture. The ordinates show the absorption coefficient of a hypothetical material with thickness corresponding to 3 or 30 monolayers (ML) of graphene and with constant refractive index $n = n_{graphite}$.

In a first case we analyze 30 monolayers (ML) on glass and investigate regions of validity within 10% accuracy. The validity regions are in general limited by high energy and high absorption coefficient thresholds stemming from the above mentioned assumptions: $k << n$, $ad << 1$, $dn << \lambda$. Additionally, there is a tendency to limit the region to the area close to a line satisfying approximately the relation $n \approx k$, approaching the case of a purely imaginary permittivity. Considering the transmittance (violet) and absorptance (red, yellow) only, the TFL is—for reference data of $a_{graphene}$ taken from ref. 27 (dashed line)—valid in whole its range from 1.6 eV to 5 eV. When additionally the reflectance (green, blue) is considered, the validity region shrinks, yet only the range from 1.8 eV to 3.6 eV falls outside this region and only for glass-side incidence.

In a second case we consider a 10× thinner sample (3 ML), 10× better accuracy (1%) and we obtain slightly broader regions of TFL validity than in the previous case. In this case, the reference data of $a_{graphene}$ fall completely into the region of validity. This implies that when measuring less than 3 graphene monolayers on glass under perpendicular incidence, in the range up to 5 eV with 1% relative accuracy, one *cannot* distinguish between absorption coefficient, refractive index and thickness. This is valid in the near-infrared to visible range for any material with absorption coefficient below 10^5cm^{-1}.

In a third case, we remove the glass substrate, assuming thus a freestanding layer. The region of TFL validity for transmittance and absorptance changes slightly, but for reflectance, conversely, the validity of TFL shrinks to a negligible region around the $n \approx k$ line. The reference $a_{graphene}$ satisfies the validity only in the range from 4.2 eV to 4.6 eV. This means that measuring the reflectance of freestanding layer is a way to avoid the TFL, enabling improved distinction between *a*, *d* and *n*. For oblique incidence, additional simulations (not shown here) prove a similar difficulty to distinguish between *a*, *d* and *n*, for thin
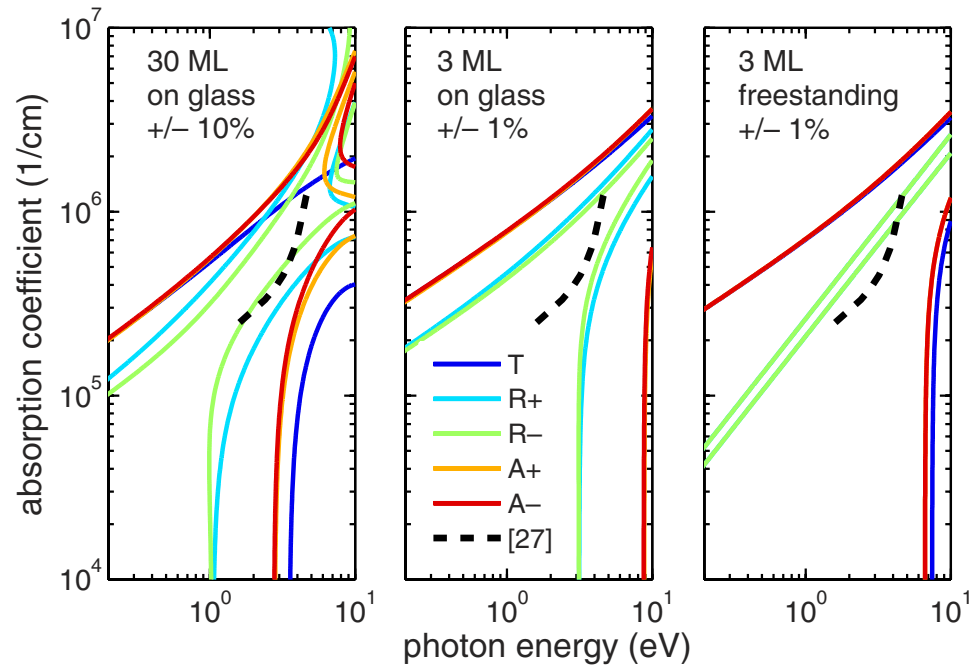
Figure 1. Lines represent contours between which the TFL differ from rigorous calculation less than 10% or 1% relatively. R+, A+, refer to incidence from layer side, conversely R−, A−, refer to glass side. Note the difference between freestanding layer and layer on glass. Dashed line between 1.6 eV and 5 eV indicates the absorption coefficient taken from ref. 27.
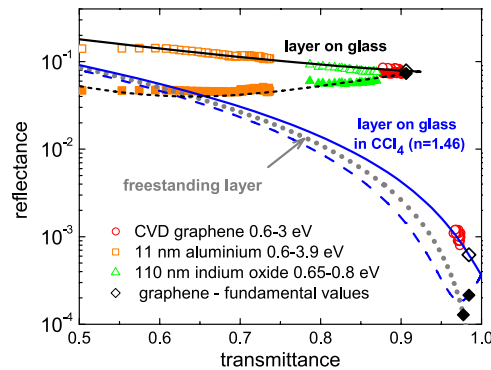
Figure 2. Lines: universal relationship between T_{TFL} and R_{TFL} in the range 0.7–3 eV of a freestanding layer (dotted line) and of a layer on glass in air or in CCl$_4$ (full and dashed lines are for layer-side and glass-side, respectively). Symbols: theoretical and experimental values for different materials (full and empty symbols are for glass-side and layer-side, respectively).

layers on a substrate. However, angles far from normal incidence, as in ellipsometry, always increase significantly the ability to distinguish between these parameters.

Experimentally, the validity of the TFL can be verified independently from the actual value of the *adn* product, thanks to one of the consequences of the TFL: The values A_{TFL}, R_{TFL} and T_{TFL} are mutually dependent in such a way that by measuring only one of them we can calculate the remaining two. By combining equations (4) and (5), one obtains for a layer on an interface:

$$R_{TFL} = \left(1 - \sqrt{\frac{n_0 T_{TFL}}{n_2}} \right)^2$$

(6)

Knowing R_{TFL} and T_{TFL}, A_{TFL} is calculated as $1 - R_{TFL} - T_{TFL}$. Noteworthy, this yields a 'universal' relation that applies to materials beyond graphene.

For any value of the *adn* product, we simulate in Fig. 2 the relationship between R_{TFL} and T_{TFL}: according to (6) for a freestanding layer, and according to (4) and (5), while accounting multiple reflections for
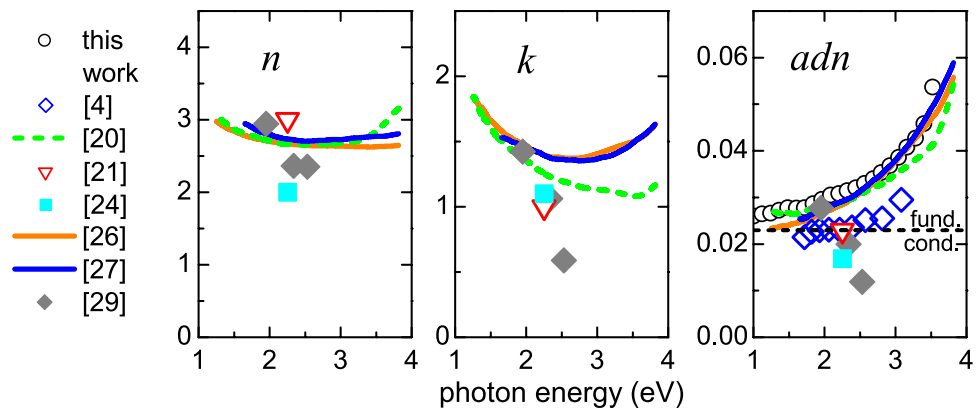
Figure 3. Different values of *n* and *k* spectra of graphene found in the literature (references in square brackets) and the respective calculated *adn* products. The dashed line on the right shows the fundamental value given by equation (2) from fundamental conuctivity. Circles represent the data experimentally obtained on the sample of CVD graphene.

the case of the layer on glass. The latter is also simulated for the case of immersion in carbon tetrachloride (CCl_4). The advantage of the CCl_4 is that at room temperature its refractive index is similar to the one of glass. As such, the situation of freestanding layers can be approached. Black symbols show the theoretical *T* vs. *R* relations, when graphene's fundamental conductivity (2) is taken. To compare with experiments, the pairs of transmittance and reflectance values represent points in the graph, plotted by symbols. We see that the symbols for graphene fall well on the theoretical curves. In addition, the TFL was equally well fulfilled for an 11-nm-thick layer of evaporated aluminum over a broad spectral range, and also for a 110-nm-thick indium oxide layer, but only in the infrared region (<0.8 eV).

The absorptance of graphene monolayer, measured with high accuracy by photothermal deflection spectroscopy was then used to evaluate the *adn* product from equation (3). This *adn* product is shown in Fig. 3 together with *n* and *k* spectra of single-layer graphene, taken from literature[4,20,21,24,26,27,29]. This graph demonstrates that there is a larger discrepancy among the published *n* and *k* values of graphene samples, compared to their respective *adn* products. This is consistent with the fact that graphene on a substrate (measured in transmission and reflection) and freestanding graphene (when measured in transmission only) always fulfills the TFL over a broad wavelength range (see Fig. 1), and that the separation of the optical constants is difficult. Measurement of reflectance of a freestanding or embedded layer is therefore recommended.

Finally, we evaluate, based on the TFL, the losses or gains of using graphene as transparent functional layer. It follows from equation (3) that the absorptance of any ultrathin layer can be reduced by embedding it into a high-refractive-index medium or by depositing it on high-refractive-index substrate. However, in the latter case, as expected, the transmittance will also be reduced due to the increased reflectance at such a substrate. So, in order to assess how the absorptance is reduced due to the TFL, it is convenient to normalize *A* by *T*. The ratio *A/T* then characterizes the fraction of light that is absorbed during transmission, establishing a useful measure for the window-material performance. It follows from (3) and (5) that for an ultrathin layer on a substrate or a freestanding layer:

$$\frac{A_{\mathrm{TFL}}}{T_{\mathrm{TFL}}} = \frac{adn}{n_2} \tag{7}$$

Moreover, the *A/T* ratio is also a good parameter for evaluating macroscopically-thin layers, because for a layer on a substrate the *A/T* ratio is virtually free from interference effects and free from direct wavelength dependencies[30], being therefore perfect for comparison to equation (7).

In Fig. 4 we simulated for a single photon energy (2.25 eV) the *A/T* ratio of a layer on a finite substrate by TFL and rigorously. In both cases the effect of multiple reflections in the substrate is accounted for by the Fresnel equations. We tested a set of thicknesses and absorption coefficients while keeping the value of *adn* product fixed to 0.0229. Three cases were considered: the embedded layer, the layer-on-substrate for layer-side incidence and the layer-on-substrate for substrate-side incidence. We see that for the embedded layer, as well as for the layer-on-substrate, the increase of refractive index of the surrounding medium or the substrate can indeed significantly reduce the ratio *A/T*. As long as the TFL describes well this phenomenon (well up to a film thickness of 10 nm) it is advantageous to embed graphene in, or place it on top of, a high-refractive-index medium. For macroscopically-thin layers (e.g. in our case 335 nm) this trend is weakened, and importantly, for lower values of refractive index of the surrounding the *A/T* ratio of macroscopically-thin layer is lower than that of ultrathin layer. This implies, that thinning down a
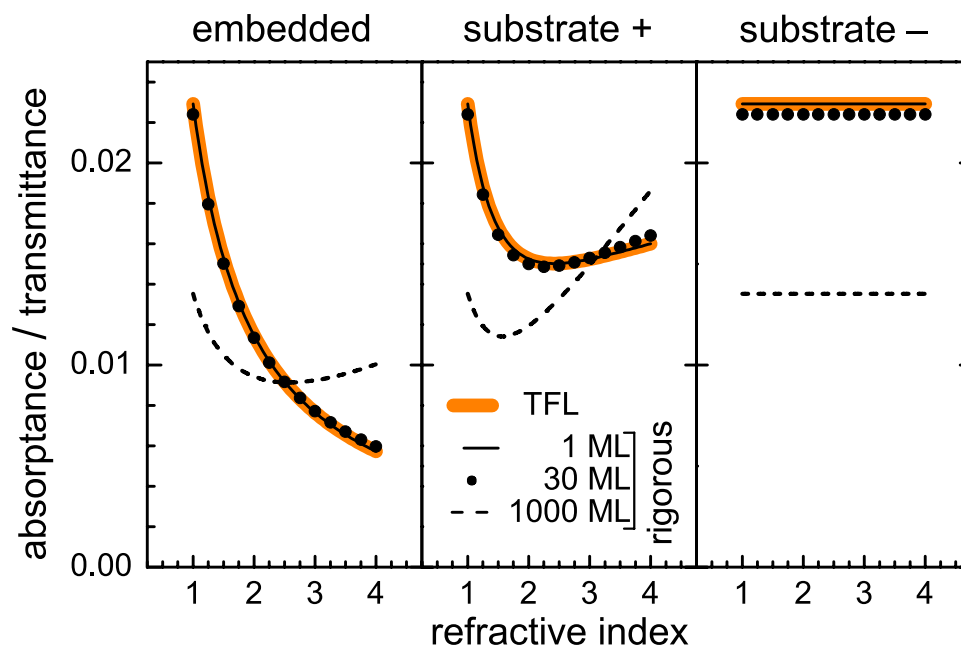
Figure 4. The effect of increase of refractive index of surrounding medium or substrate on the *A/T* ratio at photon energy 2.25 eV. "+" refers to incidence from layer-side, conversely, "−" refers to substrate-side. The cases with different thicknesses have the same *adn* product.

layer while keeping the *adn* product constant is not favorable, unless a high-refractive-index surrounding medium, e.g. silicon, is used. Interestingly, for the substrate-side incidence the refractive index has no effect on *A/T* ratio. These effects are crucial when comparing optoelectronic applications of graphene with usual macroscopically-thin window layers.

Discussion

Within a given spectral region and depending on the substrate and incidence angle, thin layers may satisfy the thin-film limit when their measurable optical properties are given only by the product of *a*, *d*, and *n*. Graphene satisfies this limit over a broad spectral range and it makes the separate determination of its optical constants difficult, especially when graphene is on a substrate. The layer thickness, as a condition of the limit, should rather be compared to the vacuum wavelength; in the infrared and upon perpendicular incidence, the limit can be satisfied even by a 100-nm-thick layer on glass (e.g. of indium oxide below 0.8 eV). Within the thin-film limit, the plot of reflectance versus transmittance is, for a given surrounding medium, a universal curve, which was also used here for experimental verification. Another interesting quantity is the absorptance normalized to transmittance, which is perfectly suitable for comparing absorption losses in graphene and other window layers. It shows that if the thin-film limit is satisfied, the performance is strongly enhanced by the high refractive index of the underlying medium.

Methods

The transmittance-reflectance spectroscopy was done either in air by Perkin-Elmer Lambda 900 or in a carbon tetrachloride (CCl_4) in a custom-made setup. Our custom-made setup also allows photothermal deflection spectroscopy (PDS)[31] measurements of absorptance with sensitivity down to 10^{-4} through heating of immersion liquid, e.g. CCl_4. The refractive index of CCl_4 is around 1.46 in our spectral range (0.6–3 eV)[32]. For our tests, we used a single layer of chemical-vapor-deposited (CVD) graphene on borosilicate glass obtained from https://graphene-supermarket.com/Transparent-Conductive-Coatings/. We also used a layer of aluminum, thermally evaporated at pressure 5×10^{-5} mbar and a layer of indium oxide, sputtered in DC regime at 6 mbar[33]. In both cases the Schott AF45 low-alkaline borosilicate glass served as a substrate.

References

1. Novoselov, K. S. Electric Field Effect in Atomically Thin Carbon Films. *Science* **306,** 666–669 (2004).
2. Geim, A. K. & Novoselov, K. S. The rise of graphene. *Nature Materials* **6,** 183–191 (2007).
3. Kuzmenko, A., van Heumen, E., Carbone, F. & van der Marel, D. Universal Optical Conductance of Graphite. *Physical Review Letters* **100,** (2008).
4. Nair, R. R. *et al.* Fine Structure Constant Defines Visual Transparency of Graphene. *Science* **320,** 1308–1308 (2008).
5. Castro Neto, A. H., Peres, N. M. R., Novoselov, K. S. & Geim, A. K. The electronic properties of graphene. *Reviews of Modern Physics* **81,** 109–162 (2009).

6. Bae, S. *et al.* Roll-to-roll production of 30-inch graphene films for transparent electrodes. *Nature Nanotechnology* **5,** 574–578 (2010).
7. Bonaccorso, F., Sun, Z., Hasan, T. & Ferrari, A. C. Graphene photonics and optoelectronics. *Nature Photonics* **4,** 611–622 (2010).
8. Novoselov, K. S. *et al.* A roadmap for graphene. *Nature* **490,** 192–200 (2012).
9. Khrapach, I. *et al.* Novel Highly Conductive and Transparent Graphene-Based Conductors. *Advanced Materials* **24,** 2844–2849 (2012).
10. Chen, X., Jia, B., Zhang, Y. & Gu, M. Exceeding the limit of plasmonic light trapping in textured screen-printed solar cells using Al nanoparticles and wrinkle-like graphene sheets. *Light: Science & Applications* **2,** e92 (2013).
11. Dawlaty, J. M. *et al.* Measurement of the optical absorption spectra of epitaxial graphene from terahertz to visible. *Applied Physics Letters* **93,** 131905 (2008).
12. Dawlaty, J. M., Shivaraman, S., Chandrashekhar, M., Rana, F. & Spencer, M. G. Measurement of ultrafast carrier dynamics in epitaxial graphene. *Applied Physics Letters* **92,** 042116 (2008).
13. Lee, C. *et al.* Optical response of large scale single layer graphene. *Applied Physics Letters* **98,** 071905 (2011).
14. Weber, J. W., Bol, A. A. & van de Sanden, M. C. M. An improved thin film approximation to accurately determine the optical conductivity of graphene from infrared transmittance. *Applied Physics Letters* **105,** 013105 (2014).
15. McIntyre, J. D. E. & Aspnes, D. E. Differential reflection spectroscopy of very thin surface films. *Surface Science* **1971,** 417–434.
16. Brendel, R. The concept of effective film thickness for the determination of bond concentrations from IR spectra of weakly absorbing thin films on silicon. *Journal of Applied Physics* **69,** 7395 (1991).
17. Chabal, Y. J. Surface infrared spectroscopy. *Surface Science Reports* **8,** 211–357 (1988).
18. Kim, I. K. & Aspnes, D. E. Toward nκd spectroscopy: Analytic solution of the three-phase model of polarimetry in the thin-film limit. *Applied Physics Letters* **88,** 201107 (2006).
19. Holovský, J. & Ballif, C. Thin-film limit formalism applied to surface defect absorption. *Optics Express* **22,** 31466 (2014).
20. Weber, J. W., Calado, V. E. & van de Sanden, M. C. M. Optical constants of graphene measured by spectroscopic ellipsometry. *Applied Physics Letters* **97,** 091904 (2010).
21. Bruna, M. & Borini, S. Optical constants of graphene layers in the visible range. *Applied Physics Letters* **94,** 031901 (2009).
22. Blake, P. *et al.* Making graphene visible. *Applied Physics Letters* **91,** 063124 (2007).
23. Skulason, H. S., Gaskell, P. E. & Szkopek, T. Optical reflection and transmission properties of exfoliated graphite from a graphene monolayer to several hundred graphene layers. *Nanotechnology* **21,** 295709 (2010).
24. Ni, Z. H. *et al.* Graphene Thickness Determination Using Reflection and Contrast Spectroscopy. *Nano Letters* **7,** 2758–2763 (2007).
25. Casiraghi, C. *et al.* Rayleigh Imaging of Graphene and Graphene Layers. *Nano Letters* **7,** 2711–2717 (2007).
26. Nelson, F. J. *et al.* Optical properties of large-area polycrystalline chemical vapor deposited graphene by spectroscopic ellipsometry. *Applied Physics Letters* **97,** 253110 (2010).
27. Kravets, V. G. *et al.* Spectroscopic ellipsometry of graphene and an exciton-shifted van Hove peak in absorption. *Physical Review B* **81,** (2010).
28. Drude, P. Lehrbuch der optik, p. 266. (1900).
29. Wang, X., Chen, Y. P. & Nolte, D. D. Strong anomalous optical dispersion of graphene: complex refractive index measured by Picometrology. *Optics Express* **16,** 22105 (2008).
30. Ritter, D. & Weiser, K. Suppression of interference fringes in absorption measurements on thin films. *Optics Communications* **57,** 336–338 (1986).
31. Boccara, A. C., Fournier, D. & Badoz, J. Thermo-optical spectroscopy: Detection by the "mirage effect". *Applied Physics Letters* **36,** 130 (1980).
32. Andersson, A. M., Niklasson, G. A. & Granqvist, C.-G. Temperature-dependent transmittance of luminous and solar radiation for quartz fibers immersed in carbon tetrachloride. *Applied Optics* **26,** 2164 (1987).
33. Barraud, L. *et al.* Hydrogen-doped indium oxide/indium tin oxide bilayers for high-efficiency silicon heterojunction solar cells. *Solar Energy Materials and Solar Cells* **115,** 151–156 (2013).

Acknowledgements

Author Contributions

J.H. performed calculations, spectrophotometric experiments and prepared the manuscript; S.N. initiated the study and supplied samples; S.D.W. provided advice and edited the manuscript; C.B. provided advice and edited the manuscript.

Additional Information

Competing financial interests: The authors declare no competing financial interests.

How to cite this article: Holovský, J. *et al.* Effect of the thin-film limit on the measurable optical properties of graphene. *Sci. Rep.* **5**, 15684; doi: 10.1038/srep15684 (2015).

Thin-film limit formalism applied to surface defect absorption

Jakub Holovský[1,2]* and Christophe Ballif[3]

[1]Institute of Physics of the Academy of Sciences of the Czech Republic, Cukrovarnická 10, 162 00 Prague
[2]CTU Faculty of Electrical Engineering, Technická 2, 166 27 Prague, Czech Republic
[3]École Polytechnique Fédérale de Lausanne (EPFL), Institute of Microengineering (IMT),
Photovoltaics and Thin-Film Electronics Laboratory, Maladière 71, CH-2000 Neuchâtel, Switzerland
*jholovsky@gmail.com

Abstract: The thin-film limit is derived by a nonconventional approach and equations for transmittance, reflectance and absorptance are presented in highly versatile and accurate form. In the thin-film limit the optical properties do not depend on the absorption coefficient, thickness and refractive index individually, but only on their product. We show that this formalism is applicable to the problem of ultrathin defective layer e.g. on a top of a layer of amorphous silicon. We develop a new method of direct evaluation of the surface defective layer and the bulk defects. Applying this method to amorphous silicon on glass, we show that the surface defective layer differs from bulk amorphous silicon in terms of light soaking.

References and links

1. R. Brendel, "The concept of effective film thickness for the determination of bond concentrations from IR spectra of weakly absorbing thin films on silicon," J. Appl. Phys., **69**(11), 7395 (1991).
2. Y. J. Chabal, "Surface infrared spectroscopy," Surf. Sci. Rep., 8(5–7), 211–357 (1988).
3. P. Drude, *Lehrbuch der optik.* p. 266 (Leipzig 1900).
4. J. D. E. McIntyre and D. E. Aspnes, "Differential reflection spectroscopy of very thin surface films," Surf. Sci., **24**(2), 417–434 (1971).
5. I. K. Kim and D. E. Aspnes, "Toward nκd spectroscopy: Analytic solution of the three-phase model of polarimetry in the thin-film limit," Appl. Phys. Lett., **88**(20), 201107 (2006)
6. A. Kuzmenko, E. van Heumen, F. Carbone, and D. van der Marel, "Universal Optical Conductance of Graphite," Phys. Rev. Lett., **100**(11), 117401 (2008).
7. J. W. Weber, A. A. Bol, and M. C. M. van de Sanden, "An improved thin film approximation to accurately determine the optical conductivity of graphene from infrared transmittance," Appl. Phys. Lett., **105**(1), 013105 (2014).
8. J. M. Dawlaty, S. Shivaraman, J. Strait, P. George, M. Chandrashekhar, F. Rana, M. G. Spencer, D. Veksler, and Y. Chen, "Measurement of the optical absorption spectra of epitaxial graphene from terahertz to visible," Appl. Phys. Lett., **93**(13), 131905 (2008).
9. R. R. Nair, P. Blake, A. N. Grigorenko, K. S. Novoselov, T. J. Booth, T. Stauber, N. M. R. Peres and A. K. Geim, "Fine Structure Constant Defines Visual Transparency of Graphene," Science, **320**(5881), 1308 (2008).
10. W. Jackson and N. Amer, "Direct measurement of gap-state absorption in hydrogenated amorphous silicon by photothermal deflection spectroscopy," Phys. Rev. B, **25**(8), 5559–5562 (1982).
11. H. Curtins and M. Favre, "Surface and bulk states determined by photothermal deflection spectroscopy," in *Amorhpous silicon and related materials*, H. Fritzsche, ed. (World Sci. Publ. Comp., 1988) pp. 329–363.
12. M. Vaněček, M. Kočka, J. Stuchlík, and J. Tříska, "Direct measurement of the gap states and band tail absorption by constant photocurrent method in amorphous silicon," Solid State Commun., **39**(11), 1199–1202 (1981).
13. M. Vanecek and A. Poruba, "Fourier-transform photocurrent spectroscopy of microcrystalline silicon for solar cells," Appl. Phys. Lett., **80**(5), 719–721 (2002).
14. R. C. Frye, J. J. Kumler, and C. C. Wong, "Investigation of surface passivation of amorphous silicon using photothermal deflection spectroscopy," Appl. Phys. Lett., **50**(2) 101–103 (1987).
15. A. Asano and M. Stutzmann, "Depth profiling of nonuniform optical absorption in thin films: Application to hydrogenated amorphous silicon," J. Appl. Phys., **70**(9), 5025–5034 (1991).
16. G. Grillo and L. Deangelis, "Surface states and in-depth inhomogeneity in a-Si:H thin films: Effects on the shape of the PDS sub-gap spectra," J. Non-Cryst. Solids, **114**(2), 750–752 (1989).

17. F. Becker, R. Carius, J.-T. Zettler, J. Klomfass, C. Walker, and H. Wagner, "Photothermal Deflection Spectroscopy on Amorphous Semiconductor Heterojunctions and Determination of the Interface Defect Densities," Mat. Sci. Forum, **173–174**, 177–182 (1995).
18. J. Holovský, M. Schmid, M. Stuckelberger, M. Despeisse, C. Ballif, A. Poruba, and M. Vaněček, "Time evolution of surface defect states in hydrogenated amorphous silicon studied by photothermal and photocurrent spectroscopy and optical simulation," J. Non-Cryst. Solids, **358**(17), 2035–2038 (2012).
19. J. Holovsky, Institute of Physics of the Academy of Sciences of the Czech Republic, Cukrovarnická 10, 162 00 Praha, S. Nicolay, S. De Wolf, and C. Ballif are preparing a manuscript to be called "Effect of thin-film limit on measurable properties of graphene"
20. D. Ritter and K. Weiser, "Suppression of interference fringes in absorption measurements on thin films," Optics Commun., **57**(5), 336–338 (1986).
21. M. Vaněček, J. Kočka, A. Poruba, and A. Fejfar, "Direct measurement of the deep defect density in thin amorphous silicon films with the absolute constant photocurrent method," J. Appl. Phys., **78**(10), 6203 (1995).
22. P. Yeh, *Optical Waves in Layered Media*. (Wiley, 1988).
23. N. Wyrsch, F. Finger, T. Mcmahon, and M. Vanecek, "How to reach more precise interpretation of subgap absorption spectra in terms of deep defect density in a-Si:H," J. Non-Cryst. Solids, **137–138**, 347–350 (1991).

1. Introduction

The so-called thin-film limit (TFL) or thin-film approximation is consistent with the concept of effective thickness that does not distinguish between thickness and absorption coefficient [1]. The thickness d and dielectric function ε of an atomic monolayer lose their usual physical meaning and are rather defined as tensors, related to each other as $(\vec{\varepsilon} - 1) \cdot \vec{d} = 4\pi N \vec{\rho}$, where N and $\vec{\rho}$ is the density of dipoles and the vector of polarizability [2]. Similarly, Drude theory of inhomogenous ultrathin films predicts optical properties depending only on integral values of dielectric function over the film thickness [3]. Importantly, if the layer is parameterized by its absorption coefficient α, thickness d and refractive index n, the measurable optical properties A, R and T do not – in the FTL – depend on the parameters α, d or n individually, but only on their product αdn. Neither do they depend directly on the wavelength.

The derivation of the TFL is usually based on a linear approximation of the Fresnel equations in the limit of thickness going to zero [1,2,4–7]. These equations have appeared recently in a simple form for transmittance of freestanding graphene [6,8], but their general derivation also for reflectance is lacking in literature [7,9]. Here we show a new, simple and instructive derivation of these equations in an accurate and useful form that will be used to a new method of surface defect absorption, e.g. in hydrogenated amorphous silicon (a-Si:H).

Samples of a-Si:H are usually deposited as thin layers. Low absorptance measurements such as photothermal deflection spectroscopy (PDS) [10,11], constant photocurrent method (CPM) or Fourier-transform photocurrent spectroscopy [12,13] (FTPS) are used to evaluate defect absorption. Defect absorption may be elevated at the surfaces [11,14] enhancing interference pattern of absorptance (and hindering its smoothening by normalization by transmittance), depending on the side of illumination [15–17]. The evaluation of surface defect is complex and may be done either by varying sample thickness [11] or by comparison of absorptance measurements from layer and substrate side and complex simulations as done in our previous work [18]. However, under conditions of the TFL the defective layer can be parameterized only by only one "effective product" comprising of the product of its (virtual) thickness, refractive index and absorption coefficient. This significantly reduces the number of unknowns and the equations under TFL are also much simpler. Hence, the surface and bulk defects can be calculated directly without fitting.

2. Thin-film limit

We base our derivation on the conservation of energy, the continuity of the parallel components of an electric field across the layer and the assumptions of a low-absorbing medium ($n \gg k$) and a small thickness ($\alpha d \ll 1$, $dn \ll \lambda$). These approximations imply a linear dependence of the absorbed energy I_A in a layer of an absorbing medium of thickness d,

$$I_A \approx I_{\text{eff}} \alpha d, \tag{1}$$

where I_{eff} is the "effective" energy flux. Note that the flux I_{eff} is treated as a constant because Eq. (1) neglects its attenuation. The energy flux is related to its respective electric field through the time-averaged Poynting vector S, defined by Eq. (2).

$$I = \langle S \rangle_{\text{time}} = \frac{1}{2}\sqrt{\frac{\varepsilon_0}{\mu_0}}|E|^2 n \tag{2}$$

From this, it follows that also the effective electric field E_{eff} is constant inside the layer. We define the measurable optical absorptance A as $A = I_A/I_0$ by normalization to the energy flux of the incident wave I_0 propagating in the overlayer (refractive index n_0):

$$A \equiv \frac{I_A}{I_0} = \frac{|E_{\text{eff}}|^2 \alpha d n}{|E_0|^2 n_0} \tag{3}$$

To calculate the absorptance A, the value of E_{eff} has to be known. In the same manner reflectance and transmittance are defined as $R=I_R/I_0$ and $T=I_T/I_0$. Employing the law of energy conservation $1=A+R+T$ for the whole system, we can then write:

$$1 = \frac{|E_{\text{eff}}|^2}{|E_0|^2}\frac{\alpha d n}{n_0} + \frac{|E_R|^2}{|E_0|^2} + \frac{|E_T|^2}{|E_0|^2}\frac{n_2}{n_0} \tag{4}$$

Again, based on our assumptions we neglect the evolution of the electric field throughout the ultrathin layer and assume the continuity of parallel components of electric fields:

$$E_0 + E_R \cong E_{\text{eff}} \cong E_T \tag{5}$$

This derivation does not rely on the electric field attenuation between two distinct borders of the thin film, but assumes only the presence of an "absorbing interface" where the value of the effective field E_{eff} has to fulfill the conditions of Eqs. (4) and (5). Assuming $n \gg k$, it follows that the Fresnel coefficients E_R/E_0 and E_T/E_0 are real and the absolute-value brackets in Eq. (4) can be omitted. From Eqs. (4) and (5), we obtain a quadratic equation for E_T/E_0 featuring only one non-zero root, from which we obtain the transmittance T_{TFL}:

$$T_{\text{TFL}} = \frac{4n_0 n_2}{(n_0 + n_2 + \alpha d n)^2} \tag{6}$$

Once E_T is known, combining Eqs. (5) and (3), one obtains the absorptance A_{TFL}:

$$A_{\text{TFL}} = \frac{4\alpha d n n_0}{(n_0 + n_2 + \alpha d n)^2} \tag{7}$$

Reflectance then follows from energy conservation:

$$R_{\text{TFL}} = \frac{(n_0 - n_2 - \alpha d n)^2}{(n_0 + n_2 + \alpha d n)^2} \tag{8}$$

To test of the TFL validity, especially in the case of graphene, is interesting as it points to the difficulty to directly measure its optical parameters. More detailed discussion as well as an experimental validation of the new TFL on graphene is published elsewhere [19].
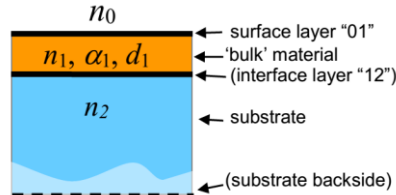

Fig. 1. Sample of layer with surface defective layer at the top surface or at the interface with substrate.

4. Surface defect correction method

The surface defect correction method is based on the same set of approximations as the thin-film limit. The situation is sketched in Fig. 1. A layer with optical parameters, indexed by α_1, d_1, n_1, is deposited on glass with refractive index n_2. The ultrathin defective surface layer, labeled '01', is described only by value of the effective product $(\alpha dn)_{01}$.

The absorptance in the defective layer can be calculated by Eq. (3) where we have to insert field E_{eff} calculated by (5). We calculate E_{eff} from reflected electric field for the top illumination and we calculate E_{eff} from transmitted electric filed for the bottom illumination. To distinguish between E_{eff} for surface and interface – will be discussed later – we use labeling E_{01} and E_{12} respectively. When the layer is illuminated from top we use labeling "+", conversely we use "−" for illumination from the substrate side. Assuming that the effect of the defective surface absorption has magnitude below 1% (usually it is much less) we can as well neglect the effect of the defective layer on the transmittance t_{210} and reflectance t_{210} of the whole stack. Symbols r_{012} and t_{210} indicate the amplitude (Fresnel) coefficients. The ascending order of the indices indicate the "+" direction of illumination and vice versa.

For the electric field at the interface E_{01} we get

$$E_{01+} \cong E_{0+}\left(1+r_{012}\right) \tag{10}$$

$$E_{01-} \cong E_{2-}\, t_{210} \quad, \tag{11}$$

where E_{0+} and E_{2-} are electric fields outside the stack, to which everything is normalized. By application of formula (3) we obtain A_{01+} and A_{01-}, describing the absorptance of the interface layer for light incident from top and bottom respectively:

$$A_{01+} \cong \left|1+r_{012}\right|^2 \frac{(\alpha dn)_{01}}{n_0} \tag{12}$$

$$A_{01-} \cong \left|t_{210}\right|^2 \frac{(\alpha dn)_{01}}{n_2} = \left|t_{012}\right|^2 \frac{n_2}{n_0^2}(\alpha dn)_{01} = T_{012}\frac{(\alpha dn)_{01}}{n_0}, \quad \text{where} \quad T_{012} = \left|t_{012}\right|^2 \frac{n_2}{n_0} \tag{13}$$

The total measured absorptances $A_{\mathrm{tot+}}$ and $A_{\mathrm{tot-}}$ include both the absorptances of the bulk layer and the surface defective layer. The back reflectance $R_{02}=(n_0-n_2)^2/(n_0+n_2)^2$ of the back side of the substrate is also taken into account:

$$A_{tot+} \cong A_{1+} + A_{01+} + \frac{T_{012}R_{02}}{1-R_{02}\left|r_{210}\right|^2}\left(A_{1-} + A_{01-}\right) \tag{14}$$

$$A_{tot-} \cong \frac{1-R_{02}}{1-R_{02}\left|r_{210}\right|^2}\left(A_{1-} + A_{01-}\right) \tag{15}$$

In the low and medium absorption region, we can, assuming $k^2/n^2 \ll 1$ and $1-e^{-\alpha d} \approx \alpha d$, use Eq. (4) from Ritter and Weiser [20], to calculate:

$$A_{1+}/A_{1-} \cong (n_0 n_1^2 + n_0 n_2^2)/(n_1^2 n_2 + n_0^2 n_2) \equiv b \tag{16}$$

Then, if we calculate the difference $A_{\mathrm{tot+}}$ and $cA_{\mathrm{tot-}}$, where c fulfills equation

$$b\left(1-R_{02}\left|r_{210}\right|^2\right)+T_{012}R_{02}-c\left(1-R_{02}\right)=0, \tag{17}$$

we obtain simple relation:

$$A_{\mathrm{tot+}} - cA_{\mathrm{tot-}} \cong A_{01+} - bA_{01-} \tag{18}$$

Using Eqs. (12) and (13) we can access the effective product $(\alpha dn)_{01}$ as follows:

$$A_{\text{tot}+} - cA_{\text{tot}-} \cong (\alpha dn)_{01} \left(\frac{1}{n_0} \left| 1 + r_{012} \right|^2 - b \frac{n_2}{n_0^2} \left| t_{012} \right|^2 \right), \tag{19}$$

where $\quad r_{012} = \dfrac{r_{01} + r_{12}e^{2i\beta}}{1 - r_{10}r_{12}e^{2i\beta}} \quad , \quad t_{012} = \dfrac{t_{01}t_{12}e^{i\beta}}{1 - r_{10}r_{12}e^{2i\beta}} \quad , \quad \beta = 2\pi N_1 d / \lambda \quad , \quad N_1 = n_1 + \alpha_1 \lambda / 4\pi$

and t_{ij}, r_{ij} are intensity Fresnel coefficients for perpendicular incidence on i/j interface. Once knowing $(\alpha dn)_{01}$, we can get to A_{01-} from Eq. (13) and to A_{1-} from Eq. (15):

$$A_{1-} = A_{tot-}^* \frac{1 - R_{02} \left| r_{210} \right|^2}{1 - R_{02}} - T_{012} \frac{(\alpha dn)_{01}}{n_0} \tag{20}$$

The absorptance in bulk A_{1-} divided by transmittance (an interference-free quantity), can be used to calculate the absorption coefficient α_1 by Eq. (6) in [20]. The evaluation is two-step: Standard evaluation [20,21] gives α_1 (n_1 is simulated by Cauchy formula) in high absorption region, neglecting surface defects; then α_1 n_1 are inserted into c and the right side of Eq. (19).

4. Interface defects correction method

In [18] we have shown that, if the defect density is both at top surface and at the interface with substrate, the surface correction is practically impossible. However, when the defective layer is only at the interface (labeled "12"), represented by effective product $(\alpha dn)_{12}$, the Eqs. (21), (22) analogical to (19), (20) can be derived:

$$A_{\text{tot}+} - cA_{\text{tot}-} \cong (\alpha dn)_{12} \left(\frac{1}{n_0} \left| t_{012} \right|^2 - \frac{b}{n_2} \left| 1 + r_{210} \right|^2 \right) \quad , \text{where} \quad r_{210} = \frac{r_{21} + r_{10}e^{2i\beta}}{1 - r_{10}r_{12}e^{2i\beta}} \tag{21}$$

$$A_{1-} = A_{tot-}^* \frac{1 - R_{02} \left| r_{210} \right|^2}{1 - R_{02}} - \left| 1 + r_{210} \right|^2 \frac{(\alpha dn)_{12}}{n_2} \tag{22}$$

Note that the Eqs. (16), (17), (19) − (22) simplify when the substrate back surface can be neglected ($R_{02}=0$). This is the case of PDS where refractive index of ambient is close to 1.5.
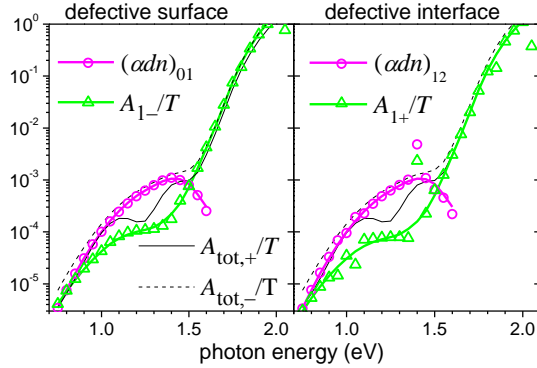
Fig. 2. Absorption in bulk material – represented by A_1/T ratio, and in 3nm thick defective layer – represented by $(\alpha dn)_{ij}$, either on surface or on glass-layer interface. Lines are directly simulated, symbols are extracted by the correction method presented here from rigorously simulated data of $A_{\text{tot}+}/T$, $A_{\text{tot}-}/T$ (thin black lines).

4. Results and discussion

We simulated the complete situation by the transfer-matrix method [22]. We first defined the structure as in the Fig. 1 with d_1=360nm, n_1=$n_{\text{a-Si:H}}$, the thickness of the defective layer was 3nm and its refractive index was the same as the layer. We calculated $A_{\text{tot}+}$, $A_{\text{tot}-}$ and T by

transfer matrix method. Then we extracted back the absorption of bulk A_{1-} and A_{1+} and surface effective products $(\alpha dn)_{01}$ and $(\alpha dn)_{12}$ by Eqs. (19) – (22), see Fig. 2.

The accuracy and robustness of the calculation depends on how far from zero are the values on left and right side of the Eq. (19) and (21). This depends on the refractive index n_2: When we are in the region of low absorptance and if $n_2=n_1$ then, every time the T is in maximum, right sides of (19) and (21) go to zero, which is a singularity in the calculation. On the other hand, when $n_2>n_1$ no singularity occurs in the right side of (19) whereas the right side of (21) has even more singularities because it crosses zero many times. That is why the correction performs better for defective surface than defective interface, as we see in Fig. 2.

We applied the correction method to the experiment described in [18], where we had identified defective layer on the top surface. A 360 nm thick hydrogenated amorphous silicon was deposited on glass by plasma-enhanced chemical vapor deposition. The spectra of A_{tot+}, A_{tot-} and T were measured by FTPS and PDS. The measurements were repeated in time and as the last step, the sample was light soaked. A significant evolution was observed in the curves around energy 1.2 eV where absorptance corresponds to defect density [12,21,23], see Fig. 3. The A_{tot-} curves were multiplied by c and all curves were put into absolute scale to fit to PDS results at region around 1.7eV (FTPS is not an absolute method). This gave the left side of the Eq. (19) and $(\alpha dn)_{01}$ was calculated. From Eq. (20) A_{1-} was obtained and absorption coefficient α_1 was calculated by [20] and bulk defect states assessed by [23] assuming density of atoms in bulk $\sim 4\times10^{22}\text{cm}^{-2}$. Surface defects were calculated by dividing $(\alpha dn)_{01}$ by refractive index of bulk ($n_1\sim3.5$) and assuming density of surface atoms $\sim10^{15}\text{cm}^{-2}$. We can observe similar trend of decrease of bulk and surface states in time. After the light soaking step bulk defect density increases significantly whereas the surface defects keep decreasing.
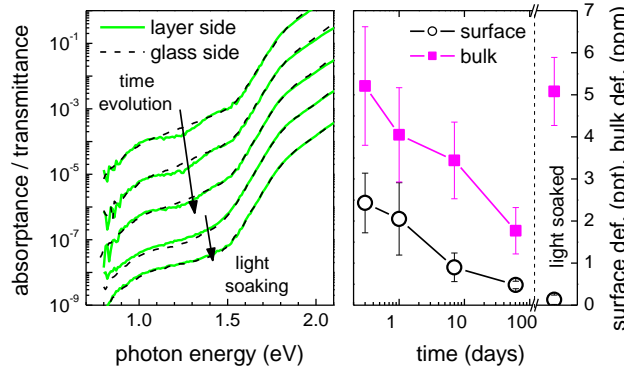
Fig. 3. Left part – FTPS spectra, measured from layer side and glass side, divided by transmittance, multiplied by c. Lower curves are consecutively shifted by a factor 1/10 form the one on top. Right part – surface defects in part per thousand of surface atoms and bulk defects in part per million of bulk atoms, extracted by our method.

4. Conclusion

Together with a new way of thin-film limit derivation we developed a simple and direct method of evaluation of defective layer at surface of thin layer or at interface of the layer with substrate. This method compares absorption measurement from layer side and glass side and works well if only one (either at the surface or at the interface with glass) defective layer thinner than 3nm is present. Separate evaluation of surface and bulk defect states is crucial. Here it helped to reveal different behavior of bulk and surface during light soaking.

SCIENTIFIC REP😊RTS

Experimental quantification of useful and parasitic absorption of light in plasmon-enhanced thin silicon films for solar cells application

Seweryn Morawiec[1,2], Jakub Holovský[3], Manuel J. Mendes[1,4], Martin Müller[3], Kristina Ganzerová[3], Aliaksei Vetushka[3], Martin Ledinský[3], Francesco Priolo[1,2,5], Antonin Fejfar[3] & Isodiana Crupi[1,6]

A combination of photocurrent and photothermal spectroscopic techniques is applied to experimentally quantify the useful and parasitic absorption of light in thin hydrogenated microcrystalline silicon (μc-Si:H) films incorporating optimized metal nanoparticle arrays, located at the rear surface, for improved light trapping via resonant plasmonic scattering. The photothermal technique accounts for the total absorptance and the photocurrent signal accounts only for the photons absorbed in the μc-Si:H layer (useful absorptance); therefore, the method allows for independent quantification of the useful and parasitic absorptance of the plasmonic (or any other) light trapping structure. We demonstrate that with a 0.9 μm thick absorber layer the optical losses related to the plasmonic light trapping in the whole structure are insignificant below 730 nm, above which they increase rapidly with increasing illumination wavelength. An average useful absorption of 43% and an average parasitic absorption of 19% over 400–1100 nm wavelength range is measured for μc-Si:H films deposited on optimized self-assembled Ag nanoparticles coupled with a flat mirror (plasmonic back reflector). For this sample, we demonstrate a significant broadband enhancement of the useful absorption resulting in the achievement of 91% of the maximum theoretical Lambertian limit of absorption.

Light trapping[1] is an essential aspect in the design of solar cells based on thin absorbers, including both amorphous/microcrystalline thin films[2–4] and the recently emerging thin mono-crystalline silicon technologies[5,6], as it allows for the absorption of the long-wavelength (near-bandgap) photons due to the extended path-length of light inside the thin semiconductor. Among a broad range of approaches proposed to realize light trapping, the scattering of light from subwavelength metallic nanoparticles, due to the localized surface plasmon resonance (LSPR) effect, is often considered a promising route[7,8], with a theoretical possibility to overcome the $4n^2$ limit[9]. In addition, the solid-state dewetting technique, commonly used for the fabrication of the metallic nanostructures[10,11], gives additional advantages of low-cost, simplicity, direct scalability and compatibility with the industrial manufacturing processes. It has been demonstrated that such nanoparticles (NPs) incorporated in the so-called plasmonic back reflector (PBR) configuration – consisting of flat silver mirror, aluminum doped zinc oxide (AZO) spacer layer and the NPs – used as a substrate for the deposition of the photovoltaic absorber, can provide efficient light trapping comparable to state-of-art random texturing[12,13].

[1]MATIS IMM-CNR, via S. Sofia 64, I-95123 Catania, Italy. [2]Dipartimento di Fisica e Astronomia, Università di Catania, via S. Sofia 64, I-95123 Catania, Italy. [3]Institute of Physics, Academy of Sciences of the Czech Republic, Cukrovarnicka 10, Prague, Czech Republic. [4]i3N/CENIMAT, Department of Materials Science, Faculty of Science and Technology, Universidade NOVA de Lisboa and CEMOP/UNINOVA, Campus de Caparica, 2829-516 Caparica, Portugal. [5]Scuola Superiore di Catania, Università di Catania, via Valdisavoia 9, 95123 Catania, Italy. [6]Department of Energy, Information Engineering and Mathematical Models (DEIM), University of Palermo, Viale delle Scienze, Building 9, I-90128 Palermo, ITALY. Correspondence and requests for materials should be addressed to S.M. (email: seweryn.morawiec@ct.infn.it) or I.C. (email: isodiana.crupi@unipa.it)

In a solar cell structure, all the supporting layers and scattering elements additional to the photovoltaic material are sources of parasitic absorption, meaning that part of the incident sunlight absorbed by the device does not contribute to the obtainable photocurrent. The proper design of the device, and in particular the metallic nanostructures, is therefore an essential issue for the suppression of the optical losses. Valuable information on the distribution of absorption within the device can be provided by optical simulations using dielectric functions determined experimentally for each material[14–16]. However, for the optical response of self-assembled plasmonic NPs, notable discrepancies between computation and experiments have been observed[11,17,18]. This is often attributed to the presence of small particles in the nanostructures, the irregular shapes of the NPs, the inter-particle interactions, the sulfidation of NPs in atmospheric air, as well as to the polycrystalline nature, defects and impurities in the material forming the NPs[11,19]. In addition, particularly for plasmonic-based light trapping, the trade-off between the beneficial effects of scattering and the deteriorating effects of parasitic absorption can severely limit the overall photocurrent enhancement that can be produced in solar cells[20–22].

Importantly, the contribution of useful and parasitic absorption cannot be measured separately with commonly used optical spectrophotometry. Therefore, in this paper we implement a combination of two absorption spectroscopy techniques, namely photothermal deflection spectroscopy (PDS)[23] and Fourier-transform photocurrent spectroscopy (FTPS)[24–26] in order to independently quantify the useful and parasitic absorption of light in plasmon-enhanced thin silicon films. The total absorption, contributed by the silicon, the silver NPs, all supporting layers and the substrate, is evaluated from the photothermal effect (PDS); while the fraction of light absorbed only in silicon (useful absorption) is measured based on the photoconductivity effect (FTPS). Although the proposed characterization method is not able to discriminate between the distinct sources of parasitic absorption – which is evaluated as the difference between the total and the useful absorption – it provides useful insights into the physical mechanisms of plasmonic light trapping as well as a first order prediction of the light trapping efficiency without the need to fabricate and process the entire device.

This method is used to determine the useful absorption enhancement in 0.9 μm thick films of hydrogenated microcrystalline silicon (μc-Si:H) provided by the distinct elements of the plasmonic back reflector configuration, at different stages of completion. It is demonstrated that the optical losses related to plasmonic light trapping in such structures are insignificant below 730 nm, beyond which they increase rapidly with increasing illumination wavelength. Furthermore, a significant broadband useful absorption enhancement of 90% is demonstrated, which resulted in achievement of 91% of the classical Lambertian limit of absorption. The improvements can be attributed to both the random front surface texture, originated from the conformal growth of Si on top of the NPs, and to the scattering of light by the plasmonic NPs.

Experimental Details

Sample preparation.
In order to investigate the light trapping in substrate-configuration thin film solar cells, self-assembled silver nanoparticles were incorporated in three distinct arrangements, depicted schematically in Fig. 1(a,c,e), which are considered as different stages of completion of a plasmonic back reflector. The NPs were fabricated by solid-state dewetting (SSD) of 12 nm thick Ag films annealed at 400°C for 1 h in nitrogen atmosphere on: (i) bare soda-lime glass (sample G_{NPs}), (ii) 50 nm thick aluminum doped zinc oxide (AZO) coated glass (sample G_{AZO_NPs}), and (iii) a stack of 100 nm thick flat Ag back reflector (BR) and 50 nm thick AZO spacer layer (sample G_{BR_NPs}). The reference samples without NPs (G_{AZO} and G_{BR}, respectively) were fabricated in the same processes. The depositions of Ag and AZO films were carried out with RF magnetron sputtering at a working pressure of 2.5×10^{-3} mbar in Ar atmosphere with RF power density of 1 and 2.16 W/cm^2, respectively. More details can be found in our previous works[11,20].

The surface morphologies were investigated by Field Emission Scanning Electron Microscopy (SEM - Zeiss Supra 25 microscope) and Atomic Force Microscopy (AFM - Bruker Dimension Icon microscope in PeakForce mode). The optical properties of the NPs, in terms of total and diffuse reflectance (R_{Total} and R_{Diff}, respectively), were measured using a Varian Cary 500 double-beam scanning UV-Vis-NIR spectrophotometer equipped with a 4-inch integrating sphere. A 0.9 μm thick μc-Si:H layer was deposited on top of the five structures shown in Fig. 1 by Plasma Enhanced Chemical Vapor Deposition (PECVD) with a power density of 0.06 W/cm^2, a working pressure of 70 Pa, a SiH$_4$ flow of 4 sccm, and a dilution ratio H$_2$/SiH$_4$ of 32, while keeping the samples' surface at 310°C. The Si film thickness was verified with an Alpha-step 100 profilometer. The Raman spectra of the μc-Si:H films were acquired at 785 nm, with a low excitation intensity of 10 mW and accumulation time of 1 s, using a Renishaw InVia Raman spectrometer.

Absorption spectroscopy.
The absorption of light in the investigated structures was measured by highly sensitive photothermal deflection spectroscopy (PDS)[23] and Fourier-transform photocurrent spectroscopy (FTPS)[24–26]. Both techniques exhibit superior sensitivity over transmittance/reflectance spectrophotometry and have been extensively used to analyze electronic defects in semiconductors.

The PDS accounts for all absorption processes that result in the generation of heat. For the investigated samples (negligible luminescence quantum yield of μc-Si:H at room temperature) and measurement condition (no collection of photo-generated carriers), all photo-generated carriers thermalize and recombine non-radiatively generating heat. When the sample is immersed in liquid, the amount of generated heat can be measured precisely by the deflection of the laser beam caused by the local change of the refractive index of the surrounding liquid due to heating. Therefore, the PDS signal is proportional to the total absorption within the sample. The experimental setup used for PDS is depicted in Fig. 2(a). The sample is immersed in Fluorinert™ Electronic Liquid FC-72 with a low refraction index of 1.25 to simulate conditions similar to ambient atmosphere. The sample is then illuminated with chopped monochromatic light from a monochromator with separate grating for UV, visible and IR coupled to a 150 W Xe lamp. A part of light is deflected by the beamsplitter into the integrating sphere equipped with Si and InGaAs photodiodes to monitor the light intensity. The probe beam from a He-Ne laser is
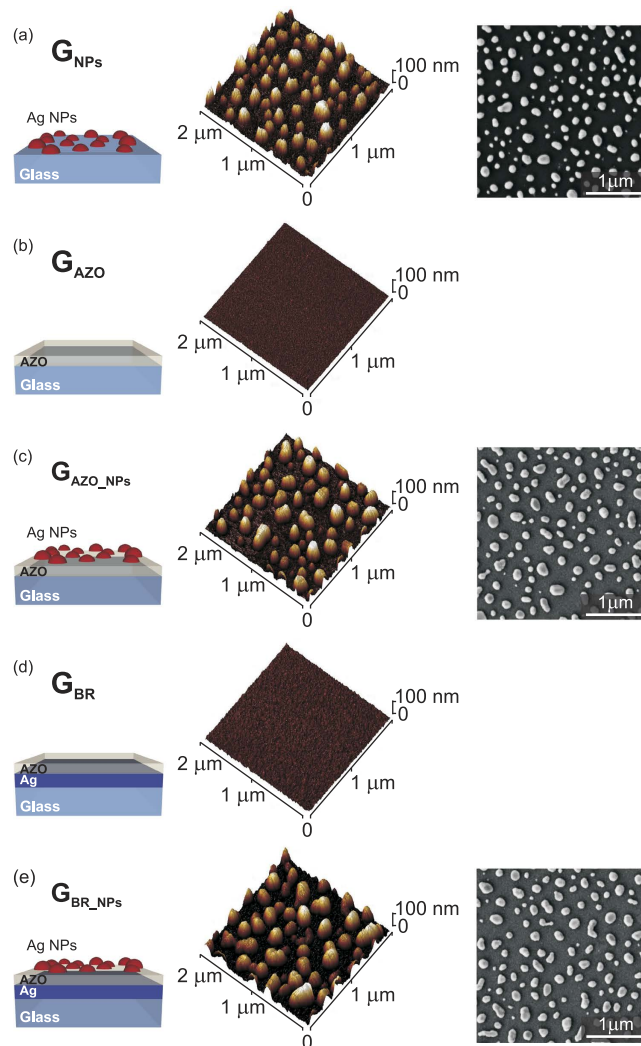
Figure 1. Schematic illustrations (*left*) and corresponding surface morphologies characterized by AFM (*center*) and SEM (*right*), of the five distinct substrate configurations used for the investigation of light trapping in μc-Si:H thin films deposited on top. G_{NPs} – Ag NPs on bare soda-lime glass; G_{AZO} – reference AZO-coated glass; G_{AZO_NPs} – NPs on AZO-coated glass; G_{BR} – reference Ag back reflector coated with AZO; G_{BR_NPs} – NPs on Ag back reflector coated with AZO (plasmonic back reflector). The NPs were fabricated in the same deposition process, from 12 nm thick Ag precursor films annealed at 400 °C for 1 h. The thicknesses of all AZO films is 50 nm.

directed parallel to the sample's surface and focused in the heating spot. The amplitude of deflection is monitored by a position detector. The signal from the detector is coupled via the multiplexer to a current preamplifier and a lock-in amplifier referenced to the chopper frequency (13 Hz). The chopped illumination generates periodical thermal waves in the liquid surrounding the sample causing the periodical deflection of the laser beam. The amplitude of the deflection normalized to the reference black sample, such as a carbon nanotubes film on glass, gives the optical absorption spectrum of the investigated sample.

The FTPS signal is derived from the number of photo-carriers generated in the photovoltaic absorber and collected on external electrodes using applied bias. Therefore, it is proportional to the useful absorption, i.e. to the maximum photocurrent extractable from the photovoltaic material. The experimental setup used for FTPS is depicted in Fig. 2(b) and the theoretical principles of this method are described in detail elsewhere[24]. The setup is based on a Michelson interferometer and was built on a customized Fourier Transform Infrared (FTIR) Spectrometer (Thermo Nexus 8700) coupled with an external high intensity light source (100 W Halogen lamp) for better stability and higher signal. To collect an electrical signal from the sample, a specific arrangement was used comprising: (1) a top electrode made of a transparent conductive oxide window, (2) an electrolyte (glycerol) spacer, and (3) a sample with conductive AZO and/or silver mirror used as a bottom electrode. The voltage source and current preamplifier are connected in series with the electrodes. The interferogram is recorded in terms of current extracted from the sample. The use of Fourier-transform method is advantageous for the improved signal-to-noise (S/N) ratio by the high illumination intensity and high measurement speed that typically allows to collect and average few hundred of scans for one sample. FTPS can be understood as a standard FTIR method
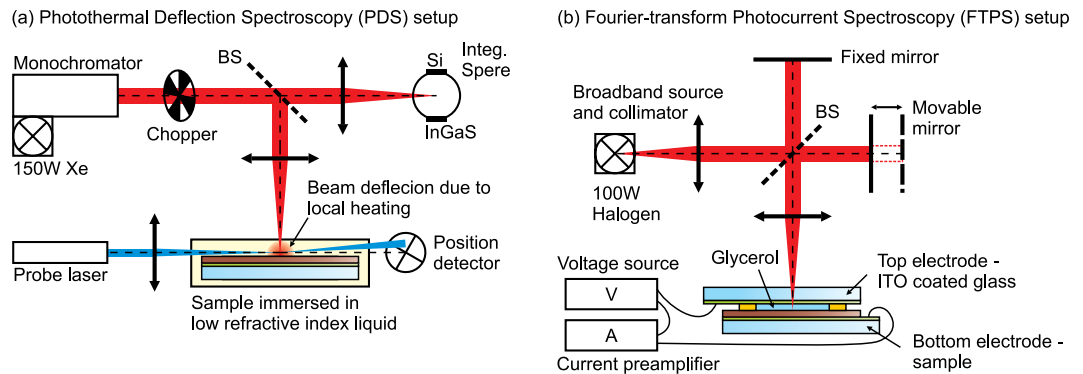
Figure 2. Schematic illustrations of the (**a**) photothermal deflection spectroscopy (PDS) and (**b**) Fourier-transform photocurrent spectroscopy (FTPS) setups. BS – beam splitter.

in which the investigated sample plays the role of a photodetector. Thus, the comparison with a calibrated detector having a known spectral response allows to determine the electrical response spectrum of the sample.

The FTPS method is valid generally provided that the photo-carriers are generated and collected homogeneously. The accuracy of FTPS is also affected by the band bending which is the limiting factor for the collection depth of the photo-carriers. Therefore, the method of signal collection becomes less accurate with increasing absorption coefficient, hence decreasing illumination wavelength, which causes inhomogeneous generation of carries and pronounced band bending. The accuracy of FTPS depends also on the sample thickness, conductivity of ohmic contacts and type of electrolyte. In our case of glycerol spacer and relatively thick sample, the relative error in the medium absorption range (600–800 nm) was estimated below 20%. The measurement conditions improve with increasing illumination wavelength providing improvements of the accuracy in the low absorption spectral region (800–1200 nm). As such, for our samples the FTPS was determined in the medium-low absorption range only.

The useful absorption of the Si film is equal to the FTPS absorption in the medium-low absorption range, while the total absorption is determined by the PDS. Therefore, the difference between the two measurements performed sequentially on the same sample determines the total parasitic absorption, which receives a contribution from all supporting layers and scattering elements. As such, the combination of PDS and FTPS spectroscopy allows for the independent quantification of the useful and total parasitic absorption, as attained by the conventional 1-R and EQE measurements usually performed in photovoltaic devices. The key advantage of the PDS + FTPS characterization approach is that it can be performed on the absorber layer alone, without requiring the full solar cell structure. Thus, it can be particularly interesting to evaluate the performance of light trapping structures coupled to the absorbers, without the interference of the additional elements (e.g. doped regions, contacts, window layers, etc.) required for the device completion.

Results and Discussion

Structural and optical characterization. The morphology of NPs fabricated in each configuration, analyzed by SEM and AFM, is depicted in Fig. 1. The average size of the NPs, determined from SEM images as the mean value of the Gaussian peak fitting to the distribution of NPs' sizes, is found to be 139 ± 2 nm for glass and 169 ± 2 nm for the glass and AZO substrate. As a result of having the same underlying layer in the SSD process, the NPs' morphologies of samples G_{AZO_NPs} and G_{BR_NPs} are fairly similar, though the NPs shapes were found to be slightly less uniform for the case of G_{BR_NPs}. The AFM analyses reveal that the NPs have approximately hemispherical shape when formed on glass and tend to flatten out on AZO. The maximum heights were in both cases close to 100 nm. The SSD fabrication parameters employed in this work for the NPs formation resulted from thorough investigations performed by the authors aimed at optimizing the nanostructures' optical properties[11] and photocurrent enhancement that they produce in a-Si:H solar cells[20].

Figure 3 depicts the optical properties, in terms of total and diffuse reflectance, measured in the front-side illumination configuration, of the five different substrates. An important parameter determining the optical performance of a sample for light trapping is the diffuse reflectance, as it corresponds to the amount of scattered photons which have an increased probability to be absorbed in the solar cell, relative to unscattered photons traversing the cell along the illumination direction. As expected, the two reference samples without NPs, G_{AZO} and G_{BR}, show negligible R_{Diff}. The NPs deposited on glass and AZO provide maximum diffuse reflectance of about 10 and 8% at 550 and 680 nm, respectively. The R_{Diff} is substantially enhanced in the wavelength range suitable for light trapping in μc-Si:H solar cells (500–1100 nm) when the NPs are coupled with a flat back reflector (sample G_{BR_NPs}). This reveals that the mirror not only reflects the transmitted diffuse light coming from the NPs, but also originates a constructive interaction, which increases the intensity of the driving field of the NPs and therefore increases their scattered power relative to the case when they are immersed in a homogeneous medium[27,28]. Nevertheless, the dissipative interaction of the light with the NPs (parasitic absorption) is also substantially enhanced, resulting in the decrease of the total reflectance with respect to the R_{Total} of the reference mirror (sample G_{BR}).

Figure 4 presents electromagnetic calculations of the normalized scattering (Q_{SCA}) and absorption (Q_{ABS}) cross sections obtained with a Mie theory formalism[29]. Such analytical method is based on a spherical particle surrounded by a homogeneous medium. Even though this condition is not satisfied in our samples, Mie theory
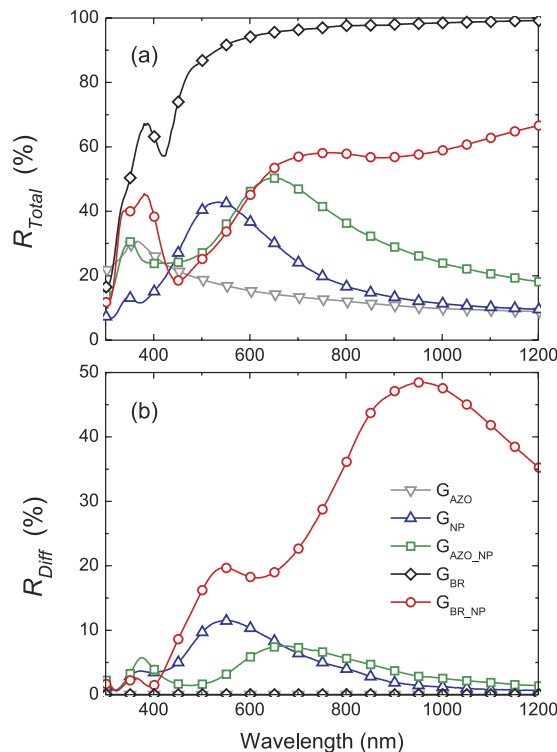
Figure 3. (**a**) Total and (**b**) diffuse reflectance of the five distinct substrate configurations depicted in Fig. 1.

can still be used for a first-order analytical prediction of the optical properties of Ag NPs embedded in different media, as performed in several previous studies related with plasmonic light trapping[7,28–31]. For the calculations in Fig. 4, we consider a single Ag nanosphere, with 131 nm diameter (the average volume-equivalent sphere diameter of the fabricated NPs) embedded in three different media with effective refractive indexes taken as the average between air and glass, air and AZO, and silicon and AZO. The spectral position and extension of the R_{Diff} peaks in Fig. 3, corresponding to G_{NP} and G_{AZO_NP}, are similar to those of Q_{SCA} of a Ag NP in glass/air and AZO/air, respectively. As such, the inter-particle effects do not influence significantly the optical properties of the nanostructures. Furthermore, for such particle size, the parasitic absorption in the NPs arrays is expected to be small relative to their scattering effects as the Q_{ABS} peaks are much smaller compared to the Q_{SCA} ones. When the substrates of Fig. 1 are covered by the μc-Si:H thin films, the high refractive index of the Si medium causes the plasmonic modes of the Ag NPs to pronouncedly red-shift and broaden, as shown by the AZO/Si Q_{SCA} curve in Fig. 4. Therefore, when coupled to a Si layer, the three samples with NPs analyzed in this work should yield light scattering peaks overlapping with the preferential light trapping wavelength range (500–1100 nm) for thin film Si cells.

Absorption enhancement in thin μc-silicon films. The five samples described in the previous section were used as substrates for the deposition of 0.9 μm thick μc-Si:H, with the aim of investigating plasmonic light trapping for substrate-configuration thin film Si solar cells. The selected deposition conditions assure high degree of crystallinity required for the narrow bandgap, which allow for the optical absorption to extend up to 1100 nm in the near-infrared. On the other hand, it was measured that the light is fully extinct in the film only for wavelengths below 500 nm. Thus, light trapping can provide absorption enhancement within the 500–1100 nm spectral window.

Figure 5 depicts the Raman spectra of μc-Si:H films deposited on the five different substrates. The high degree of crystallinity allows the clear identification of the Si band in the Raman spectra at approximately $520 \, cm^{-1}$. As discussed by Ledinský *et al.*[32], the absolute intensity of the Raman signal is proportional to the path-length of the excitation light inside the silicon layer and to the in/out-coupling efficiency. Furthermore, the spectrum acquired for the configuration of sample G_{AZO_NPs}, containing an additional 50 nm thick AZO layer covering the NPs (dashed line in Fig. 5) and separating them from the silicon layer, remains practically unchanged. This proves that surface enhanced Raman scattering (SERS)[33], originated from the high near field enhancement in the NPs' vicinity at the plasmon resonance, has a practically negligible impact on the measured increase of Raman intensity. Therefore, the observed enhancements of Raman signal for samples containing the NPs, over the flat Si film, can be attributed to the efficient far-field light trapping at the excitation wavelength; thereby providing an important insight into the enhancement of useful absorption in the Si material.

A crucial issue in plasmon-induced light trapping is to scrutinize between the absorption produced in the solar cell absorber layer (useful) and in the metallic NPs and supporting layers (parasitic), as the contributions of useful and parasitic absorption are inseparable with conventional optical spectrophotometry. To address that,
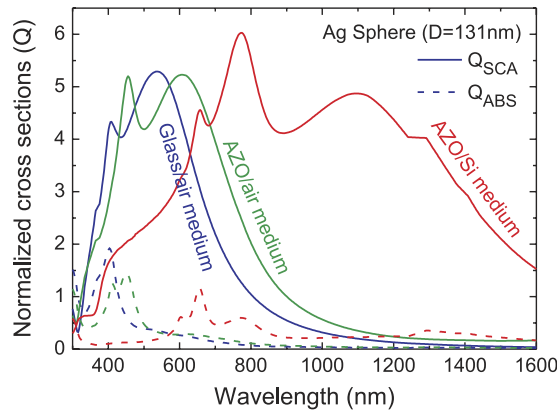
Figure 4. Calculated scattering (Q_{SCA}) and absorption (Q_{ABS}) cross sections, normalized by the physical area, of an Ag nanosphere embedded in different media. The particle diameter (D = 131 nm) is the average volume-equivalent sphere diameter of the Ag NPs fabricated in this work. The refractive index of each medium considered in the computations was taken as the average between that of the two materials surrounding the NPs in the structures of Fig. 1. These results were computed analytically with a Mie theory formalism[29].
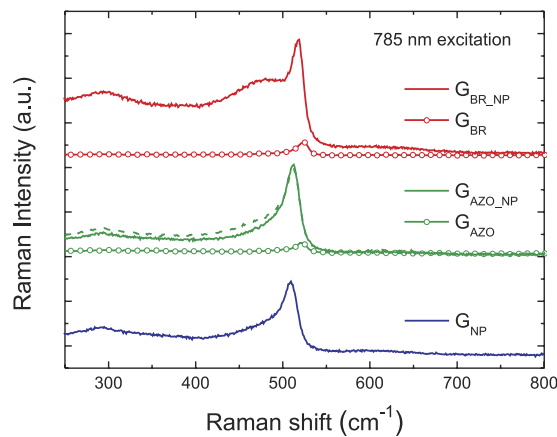
Figure 5. Raman spectra, measured with excitation at 785 nm, of 0.9 μm thick μc-Si:H deposited on the five different substrates depicted in Fig. 1. The peak at approximately 520 cm^{-1} originates from the microcrystalline phase of the films. The dashed curve refers to the sample G_{AZO_NPs} with an additional 50 nm thick AZO layer covering the NPs. The curves are displaced vertically in the graph for better visualization.

an innovative procedure involving a combination of opto-electronic spectroscopic techniques, namely PDS and FTPS, was employed in this work. As described in the Experimental details, the PDS signal accounts for all types of light absorption which result in generation of heat, so it effectively measures the total absorption in the entire investigated structure. On the other hand, the FTPS absorption is determined from the number of photo-carriers generated in the photovoltaic absorber, thus accounting only for the useful absorption. Hence, the difference between the two measurements determines the total parasitic absorption.

The PDS and FTPS absorption spectra of 0.9 μm thick μc-Si:H deposited on samples G_{AZO}, G_{AZO_NPs}, and G_{BR_NPs} are plotted in Fig. 6. In the reference G_{AZO} sample, both PDS and FTPS signals overlap, indicating that practically all absorption occurs in silicon and almost none in its AZO-coated glass substrate (only a small discrepancy, on the order of 1%, is apparent above 950 nm when plotting in logarithmic scale). It should be noted that the relatively low absolute values of absorption below 80% originate from the lack of the transparent contact deposited on top of silicon, which plays an important role of an antireflection coating.

The deposition of μc-Si:H on the substrates containing the NPs resulted in a considerable enhancement of the useful absorption in the investigated wavelength range. The parasitic losses, calculated as the difference between PDS and FTPS spectra, start to play a role only for wavelengths above 730 nm, which are poorly absorbed in flat Si films, and increase significantly towards the bandgap of μc-Si:H. The total parasitic absorption arises from multiple interactions between the light trapped in the silicon slab and the NPs, depicted schematically in the inset of Fig. 6. The number of such interactions for weakly absorbed near-infrared light increases substantially with decreasing absorption coefficient, hence increasing illumination wavelength. Consequently, the large number of interactions results in significant overall losses even though, as predicted by theoretical calculations[11,30], the absorption cross-section of each single interaction is small compared to its scattering cross-section (shown in
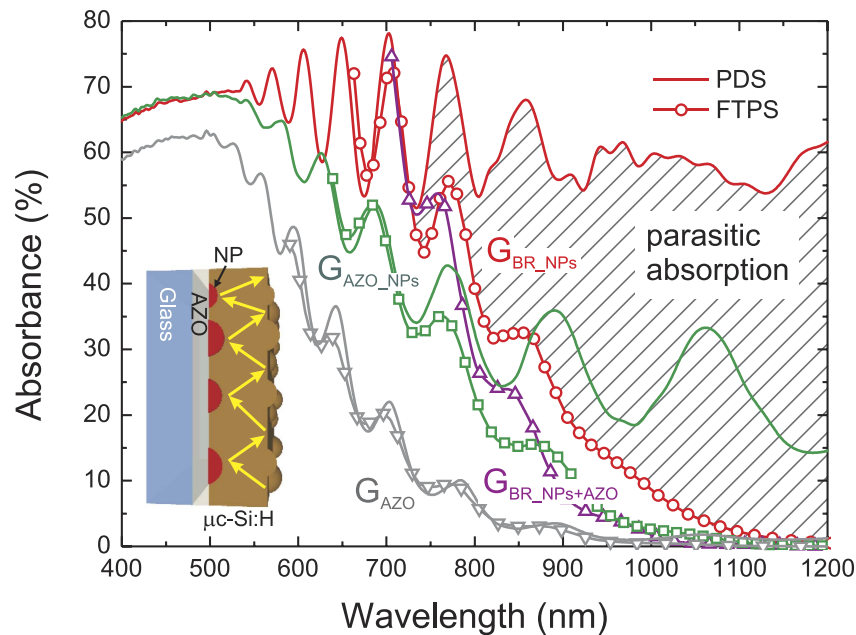
Figure 6. Total (PDS) and useful (FTPS) absorption spectra of 0.9 μm thick μc-Si:H films deposited on the samples G$_{AZO}$, G$_{AZO\_NPs}$, and G$_{BR\_NPs}$ depicted in Fig. 1. The FTPS absorption for sample G$_{BR\_NPs}$, with an additional 50 nm thick AZO layer separating NPs and silicon (labeled G$_{BR\_NPs+AZO}$), is shown for comparison. The marked area is the difference between the PDS and FTPS spectra, which represents the parasitic absorption of sample G$_{BR\_NPs}$. The inset illustrates schematically the light trapped in the silicon layer by total internal reflection and scattering events on both interfaces, redirecting the light back to the silicon.

Fig. 4). As such, in the wavelength range below 730 nm, in which most light is absorbed in the first pass through the μc-Si:H (the 100% extinction of light occurs for wavelengths below 500 nm) and the remaining photons have high probability of being absorbed after only a few scattering events, the parasitic absorption plays only a minor role.

The main sources of parasitic losses can be attributed to the dissipative interactions of light with the NPs, the Ag mirror and AZO spacer layer. It should be noted that, even though no significant parasitic absorption is observed in Fig. 6 for the sample with only the AZO layer (G$_{AZO}$), the losses in this layer or in the flat Ag mirror will necessarily increase with the presence of the nearby NPs. Although the exact values of the losses in each of these elements cannot be determined experimentally, they are all related to the plasmonic back reflector structure; thus, they should be accounted as the overall cost of the plasmonic light trapping implementation.

The deposition of μc-Si:H on self-assembled Ag NPs coupled with a flat mirror (sample G$_{BR\_NPs}$) resulted in an average useful absorption of 43% and an average parasitic absorption of 19%, calculated by integrating along the wavelength range of interest (400–1100 nm) for thin film Si solar cells. However, as observed in Fig. 6, the contribution of the parasitic absorption is only relevant for wavelengths above 730 nm for which the AM1.5G solar photon flux decreases markedly with increasing wavelength. Therefore, if we consider that our structure is a solar cell with unitary internal quantum efficiency, the attainable short-circuit current density (J$_{sc}$) calculated from useful absorption (FTPS signal) would be 19.1 mA/cm^2. This is 95% higher than that of the reference sample G$_{AZO}$ without PBR (J$_{sc}$ = 9.8 mA/cm^2) and close to the maximum theoretical current of approximately 21 mA/cm^2 that would be achieved for perfect Lambertian light diffusion on both front and rear interface[34]. The limit was calculated using dielectric functions of μc-Si:H form Jun et al.[35] without antireflection coating. The significant broadband enhancement of the useful absorption achieved for sample G$_{BR\_NPs}$ resulted in the achievement of 91% of the classical Lambertian limit of absorption.

The scattering properties of particles are strongly dependent on the dielectric function of the embedding medium[30], therefore also on the distance between the NPs and high refractive index material[31,36]. The FTPS signal of sample G$_{BR\_NPs}$ with an additional 50 nm thick AZO layer separating NPs and silicon (curve labeled G$_{BR\_NPs+AZO}$ in Fig. 6), exhibits a significant blue-shift of the absorption edge and thus a clearly lower enhancement of useful absorption in the near infrared region. This can be attributed to the decrease of the overlap between the NPs' near field and the silicon, which results in lower absorption induced by the near field as well as the narrowing of the angular distribution function of scattered light, hence lower light coupling efficiency[31,36]. As such, from the optical point of view, the NPs-Si separation should be kept as thin as possible. Nonetheless, in a complete solar cell structure the spacer layer is required as a barrier for the diffusion of metal atoms into the silicon, thus preventing the deterioration of the electrical properties of the doped layer and degradation of the p-i-n junction. In addition, a sufficiently thick spacer is also required to prevent strong absorption in the n-type layer of the cell originating from the NPs' near-field, which would result in high parasitic losses caused by the significant number of defects
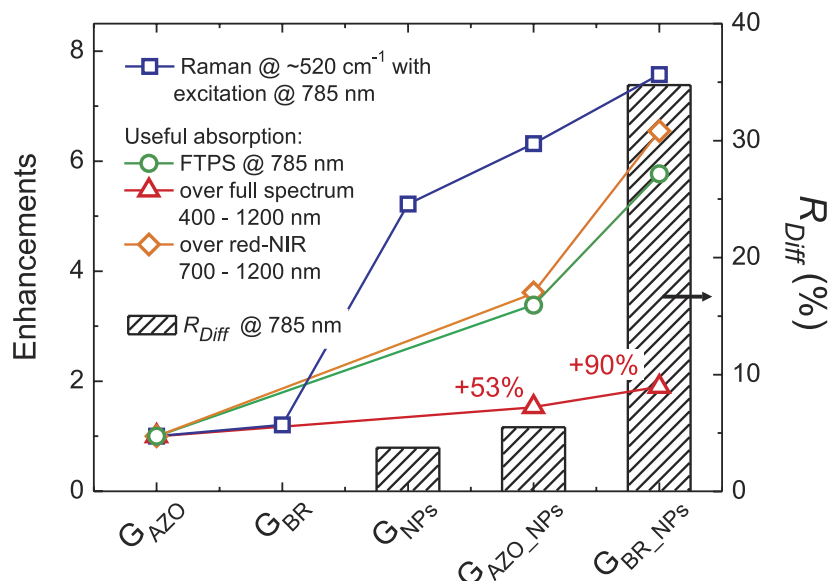
Figure 7. Enhancements (*left axis*) relative to the reference flat film (G$_{AZO}$) of the Raman Si-band peak at ~520 cm^{-1}, the FTPS useful absorption at 785 nm, the overall useful absorption integrated over 400–1200 nm, and the red-NIR part of useful absorption integrated over 700–1200 nm, provided by the different substrates depicted in Fig. 1. The enhancements are correlated with the diffuse reflectance (*right axis*) at 785 nm measured prior to the deposition of μc-Si:H.

and low carrier mobility in the doped layers. This sets up a limit for the minimum thickness of the spacer layer, as discussed in detail by Tan *et al.*[37].

The conformal growth of μc-Si:H films on top of the NPs results in a random texturing of their front surface. The surface morphologies were found to be fairly similar for the three films deposited on substrates containing NPs (G$_{NPs}$, G$_{AZO\_NPs}$, and G$_{BR\_NPs}$), having root mean square (RMS) roughness ranging from 20 to 24 nm. As such, distinct light trapping mechanisms are contributing to the overall useful absorption and Raman enhancements: (i) antireflection action and surface scattering provided by the surface texture, and (ii) scattering of light by the plasmonic nanoparticles. The high energy photons (<500 nm wavelength) are entirely absorbed in their first pass through the μc-Si:H film and therefore do not reach the back side of the film and have no possibility to interact with the NPs. Therefore, the higher absorption measured at wavelengths shorter than 500 nm for samples with NPs can only be attributed to the front surface texture. In the light trapping window (500–1100 nm), both mechanisms can originate the observed enhancement of useful absorption and their contributions cannot be directly discriminated. Nonetheless, the computational study by Kowalczewski *et al.*[38] shows that small RMS surface roughness affects predominantly the high energy photons, and its antireflection/scattering effectiveness decreases with increasing illumination wavelength. On the other hand, plasmonic scattering has impact at longer wavelengths, in the red and near-infrared part of the spectrum, due to the pronounced red-shift of the NPs resonance when placed in the vicinity of a high refractive index material[12,13,20].

Although the two light trapping mechanisms are inseparable by the spectroscopic techniques used in this work, two main conclusions can be drawn. First, the significant difference of R$_{Diff}$ between G$_{AZO\_NPs}$ and G$_{BR\_NPs}$ (see Fig. 3) indicates that the enhancement of useful absorption provided by the G$_{AZO\_NPs}$ sample should predominantly result from the textured front surface. Second, as the antireflection action provided by the surface texture is expected to contribute equally to light trapping in all samples containing NPs, and since the plasmonic scattering increases significantly in presence of a flat back mirror[27,28], the increase of useful absorption between samples G$_{AZO\_NPs}$ and G$_{BR\_NPs}$ should mainly originate from the plasmonic light trapping. The latter claim is also supported by the blue-shift of the useful absorption edge observed for sample G$_{BR\_NPs}$ with a 50 nm thick AZO layer separating NPs and silicon.

Figure 7 depicts the enhancements in selected quantities, provided by the different substrates, over the reference flat film (sample G$_{AZO}$). The FTPS (useful absorption) enhancements are compared to the diffuse reflectance at 785 nm, measured prior to the deposition of μc-Si:H films, which corresponds to the laser excitation wavelength used for Raman spectroscopy. The flat back reflector (sample G$_{BR}$) can effectively double the path-length of light inside the flat μc-Si:H film, which is meaningful only in the range 500–700 nm where specularly reflected light has still a high probability of being absorbed in the second pass through Si. Thus, the Ag mirror of sample G$_{BR}$ has been found to provide minor, 1.25, enhancement of the Raman signal acquired at 785 nm. On the other hand, much higher Raman enhancements of 6.3 and 7.6 were found for the films deposited on substrates G$_{AZO\_NPs}$ and G$_{BR\_NPs}$, respectively, due to the redirection of scattered light to more horizontal paths inside the films.

The deposition of μc-Si:H on self-assembled Ag NPs coupled with a flat mirror (sample G$_{BR\_NPs}$) resulted in a pronounced 90% enhancement of the useful absorption, in the entire investigated spectral range (triangular symbols in Fig. 7). Importantly, the enhancements of the red-NIR part of useful absorption and of the FTPS

signal at 785 nm correlate reasonably well with the diffuse reflectance provided by the substrates containing NPs. Therefore, the results demonstrate that: (1) the experimentally-measured absorption enhancements occurring in the Si, in the red-NIR range, originated in fact from the light scattering caused by the NPs; and (2) the measurements of R_{Diff} can serve as a first approximation of the light trapping performance, while the combined PDS and FTPS spectroscopy method can be applied to obtain the refined quantities of absorption.

Conclusions

A novel procedure employed in this work, involving a combination of opto-electronic spectroscopic techniques, namely PDS and FTPS, allowed for the quantification of useful and parasitic absorption in 0.9 μm thick μc-Si:H deposited on a plasmonic back reflector. It has been found that the optical losses related to the plasmonic light trapping for such structure are insignificant in the wavelength range below 730 nm, beyond which they increase rapidly with increasing illumination wavelength. This is explained by the substantial increase of the number of interactions between the NPs and the long-wavelength photons, due to the multiple internal reflections of light inside the Si film as a consequence of the rapid drop of the semiconductor's absorption coefficient, which accounts for the overall losses. Nonetheless, a significant broadband useful absorption enhancement of +90% has been demonstrated, which results in achievement of 91% of the classical Lambertian limit of absorption. The improvements can be attributed to both the random front surface texture, originated from the conformal growth of Si on top of the NPs, and to the scattering of light by the plasmonic NPs. In addition, the experiment gives new insights into the field of light trapping and associated characterization tools; proving that optical R_{Diff} measurements are a reasonable first order approximation of the performance of scattering structures, while combined PDS and FTPS spectroscopy can be a more refined optoelectronic prediction of their light trapping efficiency when applied to actual devices such as thin film solar cells.

References

1. Priolo, F., Gregorkiewicz, T., Galli, M. & Krauss, T. F. Silicon nanostructures for photonics and photovoltaics. *Nat. Nanotechol.* **9,** 19–32 (2014).
2. Battaglia, C. *et al.* Light trapping in solar cells: Can periodic beat random? *ACS Nano* **6,** 2790–2797 (2012).
3. Zhu, J., Hsu, C.-M., Yu, Z., Fan, S. & Cui, Y. Nanodome solar cells with efficient light management and self-cleaning. *Nano Lett.* **10,** 1979–1984 (2010).
4. Vanecek, M. *et al.* Nanostructured three-dimensional thin film silicon solar cells with very high efficiency potential. *Appl. Phys. Lett.* **98,** 163503 (2011).
5. Mavrokefalos, A., Han, S. E., Yerci, S., Branham, M. S. & Chen, G. Efficient light trapping in inverted nanopyramid thin crystalline silicon membranes for solar cell applications. *Nano Lett.* **12,** 2792–2796 (2012).
6. Petermann, J. H. *et al.* 19%-efficient and 43 μm-thick crystalline Si solar cell from layer transfer using porous silicon. *Prog. Photovolt.* **20,** 1–5 (2012).
7. Atwater, H. A. & Polman, A. Plasmonics for improved photovoltaic devices. *Nat. Mater.* **9,** 205–213 (2010).
8. Green, M. A. & Pillai, S. Harnessing plasmonics for solar cells. *Nat. Photonics* **6,** 130–132 (2012).
9. Callahan, D. M., Munday, J. N. & Atwater, H. A. Solar cell light trapping beyond the ray optic limit. *Nano Lett.* **12,** 214–218 (2012).
10. Thompson, C. V. Solid-state dewetting of thin films. *Ann. Rev. Mater. Res.* **42,** 399–434 (2012).
11. Morawiec, S. *et al.* Self-assembled silver nanoparticles for plasmon-enhanced solar cell back reflectors: correlation between structural and optical properties. *Nanotechnology* **24,** 265601 (2013).
12. Mendes, M. J. *et al.* Broadband light trapping in thin film solar cells with self-organized plasmonic nano-colloids. *Nanotechnology* **26,** 135202 (2015).
13. Tan, H., Santbergen, R., Smets, A. H. M. & Zeman, M. Plasmonic light trapping in thin-film silicon solar cells with improved self-assembled silver nanoparticles. *Nano. Lett.* **12,** 4070–4076 (2012).
14. Zeman, M., Isabella, O., Solntsev, S. & Jäger, K. Modelling of thin-film silicon solar cells. *Sol. Energ. Mat. Sol. Cells.* **119,** 94–111 (2013).
15. Beck, F. J. & Mokkapati, S. & Catchpole, K. R. "Light trapping with plasmonic particles: beyond the dipole model. *Opt. Express* **19,** 25230–25241 (2011).
16. Deceglie, M. G., Ferry, V. E., Alivisatos, A. P. & Atwater, H. A. Design of nanostructured solar cells using coupled optical and electrical modeling. *Nano Lett.* **12,** 2894–2900 (2012).
17. Pennanen, A. M. & Toppari, J. J. Direct optical measurement of light coupling into planar waveguide by plasmonic nanoparticles. *Opt. Express* **21,** A23–A35 (2013).
18. Schuster, C. S. *et al.* Plasmonic and diffractive nanostructures for light trapping – an experimental comparison. *Optica* **2,** 194–200 (2015).
19. Pahud, C. *et al.* Plasmonic silicon solar cells: impact of material quality and geometry. *Opt. Express* **21,** A786–A797 (2013).
20. Morawiec, S. *et al.* Broadband photocurrent enhancement in a-Si:H solar cells with plasmonic back reflectors. *Opt. Express* **22,** A1059–A1070 (2014).
21. Zhou, K. *et al.* The tradeoff between plasmonic enhancement and optical loss in silicon nanowire solar cells integrated in a metal back reflector. *Opt. Express* **20,** A777 (2012).
22. Zhang, Y., Jia, B., Ouyang, Z. & Gu, M. Influence of rear located silver nanoparticle induced light losses on the light trapping of silicon wafer-based solar cells. *J. Appl. Phys.* **116,** 124309 (2014).
23. Jackson, W. B., Amer, N. M., Boccara, A. C. & Fournier, D. Photothermal deflection spectroscopy and detection. *Appl. Opt.* **20,** 1333–1344 (1981).
24. Vanecek, M. & Poruba, A. Fourier-transform photocurrent spectroscopy of microcrystalline silicon for solar cells. *Appl. Phys. Lett.* **80,** 719–721 (2002).
25. Holovský, J. *et al.* Time evolution of surface defect states in hydrogenated amorphous silicon studied by photothermal and photocurrent spectroscopy and optical simulation. *J. Non-Cryst. Solids* **358,** 2035–2038 (2012).
26. Holovský, J. *et al.* Fourier transform photocurrent measurement of thin silicon films on rough, conductive and opaque substrates. *Phys. Status Solidi A* **207,** 578–581 (2010).
27. Santbergen, R., Tan, H., Zeman, M. & Smets, A. H. M. Enhancing the driving field for plasmonic nanoparticles in thin-film solar cells. *Opt. Express* **22,** A1026 (2014).
28. Mendes, M. J., Morawiec, S., Simone, F., Priolo, F. & Crupi, I. Colloidal plasmonic back reflectors for light trapping in solar cells. *Nanoscale* **6,** 4796–4805 (2014).
29. Fu, Q. & Sun, W. Mie theory for light scattering by a spherical particle in an absorbing medium. *Appl. Opt.* **40,** 1354–1361 (2001).

30. Temple, T. L. & Bagnall, D. M. Broadband scattering of the solar spectrum by spherical metal nanoparticles. *Prog. Photovolt.* **21,** 600–611 (2013).
31. Catchpole, K. R. & Polman, A. Design principles for particle plasmon enhanced solar cells. *Appl. Phys. Lett.* **93,** 191113 (2008).
32. Ledinský, M. *et al.* Light trapping in thin-film solar cells measured by Raman spectroscopy. *Appl. Phys. Lett.* **105,** 111106 (2014).
33. Araújo, A. *et al.* Highly efficient nanoplasmonic SERS on cardboard packaging substrates. *Nanotechnology* **25,** 415202 (2014).
34. Green, M. A. Lambertian light trapping in textured solar cells and light-emitting diodes: analytical solutions. *Prog. Photovoltaics* **10(4),** 235–241 (2002).
35. Jun, K. H., Carius, R. & Stiebig, H. Optical characteristics of intrinsic microcrystalline silicon. *Phys. Rev. B* **66,** 115301 (2002).
36. Pillai, S., Beck, F. J., Catchpole, K. R., Ouyang, Z. & Green, M. A. The effect of dielectric spacer thickness on surface plasmon enhanced solar cells for front and rear side depositions. *J. Appl. Phys.* **109** (2011).
37. Tan, H., Santbergen, R., Yang, G., Smets, A. H. M. & Zeman, M. Combined Optical and Electrical Design of Plasmonic Back Reflector for High-Efficiency Thin-Film Silicon Solar Cells. *IEEE J PHOTOVOLT* **3,** 53–58 (2013).
38. Kowalczewski, P., Liscidini, M. & Andreani, L. C. Light trapping in thin-film solar cells with randomly rough and hybrid textures. *Opt. Express* **21,** A808–A820 (2013).

Acknowledgements

Author Contributions

S.M. fabricated and characterized the nanoparticles and wrote the main manuscript text. J.H. performed PDS and FTPS measurements. M.J.M. conducted the Mie calculations and contributed to the writing of the manuscript. M.M. conducted the deposition of μc-Si:H. K.G. and M.L. performed Raman characterization. A.V. performed AFM measurements. F.P., A.F. and I.C. planned and supervised the experiment. All authors reviewed the manuscript.

Additional Information

Competing financial interests: The authors declare no competing financial interests.

How to cite this article: Morawiec, S. *et al.* Experimental quantification of useful and parasitic absorption of light in plasmon-enhanced thin silicon films for solar cells application. *Sci. Rep.* **6**, 22481; doi: 10.1038/srep22481 (2016).

Fourier transform photocurrent measurement of thin silicon films on rough, conductive and opaque substrates

Jakub Holovský [*,1], **Űmit Dagkaldiran**[2], **Zdeněk Remeš**[1], **Adam Purkrt**[1,3] **Tibor Ižák**[1,4] **Aleš Poruba**[1,5] **and Milan Vaněček**[1]

[1] Institute of Physics of the ASCR v. v. i. , Cukrovarnicka 10, 162 53 Prague 6, Czech Republic

[2] Institute of Energy Research - Photovoltaik, Forschungszentrum Jülich, D-52425 Jülich, Germany

[3]Czech Technical University in Prague, Fac. of Nucl. Sciences and Phys. Eng., Trojanova 13, CZ-12000 Praha 2, Czech Republic

[4] FEI Slovak University of Technology, Ilkovicova 3, 812 19 Bratislava Slovak Republic

[5] Solartec s.r.o., Televizní 2618, 756 61 Rožnov p. R., Czech Republic

* Corresponding author: e-mail holovsky@fzu.cz, Phone: +420 220 318 516, Fax: + 420 233 343 184

Fourier transform photocurrent spectroscopy (FTPS) is used as an inspection method for hydrogenated amorphous silicon (a-Si:H) thin films deposited on aluminium foil and aluminium foil coated with rough SnO_2. These structures are part of roll-to-roll solar cell fabrication process. Measurement technique utilizes transparent electrode in a sandwich arrangement. An elaborate calculation procedure is used to correct the measurement for the optical effects in order to obtain spectra of optical absorption coefficient. Correction procedure is based partly on analytical formulae and partly on Monte-Carlo simulations. Quality of thin a-Si:H layers deposited by PECVD on glass and aluminium foil with and without rough layer of SnO2 were compared. Positive effect of aluminium and SnO2 on layer quality and effect of bandgap shift was observed.
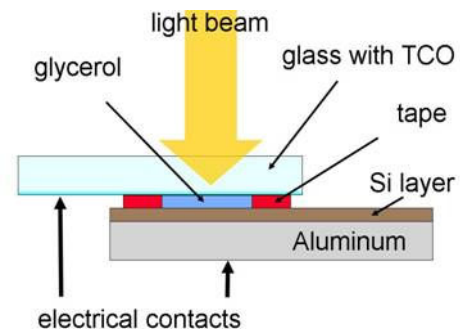
Figure 1 Sandwich arrangement of photocurrent measurement of layers on opaque and conductive substrates.

1 Introduction Thin films in recent photovoltaic applied research are often deposited on substrates that make evaluation of optical properties rather difficult. Substrates used in the roll-to-roll approach [1] are rough, conductive and even non transparent. Typical inspection methods used for thin film amorphous or nanocrystalline silicon are Constant photocurrent method (CPM) [2] and Fourier transform photocurrent spectroscopy (FTPS) [3,4]. Both have been applied mostly on films on smooth, transparent and non-conductive substrates. Now we present measurement technique and numerical correction procedure for FTPS measurement and evaluation of layers deposited on aluminium with or without rough conductive oxide. We compare the quality of such layers with those grown on low alkaline glass.

2 Samples
We conduct our experiment on the series of a-Si:H layers co-deposited onto four different substrates, see Table 1. Samples called 2A and 2B differ in the type of Al foil. All a-Si:H layers were deposited in one deposition run by using the PECVD technique at 13.56MHz excitation fre-

quency. The films were prepared at substrate temperatures below 200 °C.

Table 1 List of samples.

sample 0	sample 1	sample 2A	sample 2B
a-Si:H on glass	a-Si:H on bare Al	a-Si:H on Al "A" + SnO_2	a-Si:H on Al "R" + SnO_2

3 Measurement

3.1 Photocurrent Photocurrent spectroscopy was carried out by the setup based on FTIR spectrophotometer Thermo Nexus 8700. For better stability and higher signal the setup was equipped with external 100W halogen source. The method principle is referred e.g. in [5]. The sample on glass is in coplanar electrodes arrangement, while the samples on Al foil are in special sandwich arrangement similar as the one used for in-situ photoluminescence [6]. The back contact is realized by conductive substrate while the front contact is made by glass with conductive ZnO layer and a tape spacer with 2x8mm^2 hole filled with glycerol serving as an electrolyte, see Fig. 1.

The structure glycerol/a-Si:H/substrate exhibits some band bending and surface recombination effects, unwanted in the photocurrent measurement. In the FTPS spectroscopy the whole spectrum can be seen in every moment and many such effects can be observed directly. We observed three effects: a) Signal non-linearity that manifested itself as a nonzero signal in UV range, where the light source intensity was zero. b) Phase inhomogeneity due to the weak internal field that exhibits as interferogram without one central maximum. See example in Fig. 2. 3) Suppression/enhancement of signal from the front surface (blue response) due to the strong band bending.
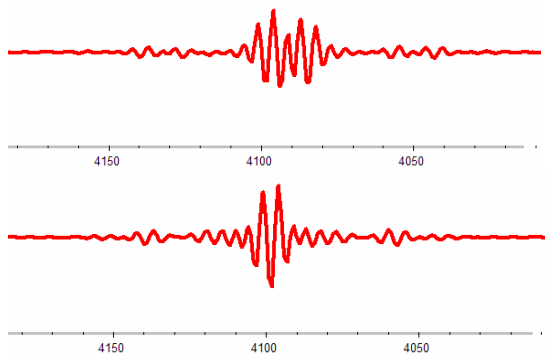
Figure 2 Observed interferogram (i.e. record of FTPS signal in time and also Fourier image of spectrum in time domain). Upper part: low internal field (zero bias), large phase inhomogeneity. Lower part: Sufficient internal field (-1.5V bias on glycerol.), signal in phase, interferogram with one central maximum.

The effects are strong for voltage biases close to zero. We found out that bias voltage (we used -1.5Volts on glycerol contact) suppressed the last two effects, although some

effect of surface recombination always persisted. The intensity of modulated beam in high absorption region had to be lowered 100-1000 times, to reduce non-linearities.

In our technique each spectrum is measured in two steps: first with white light and then with a set of glass filters that flattens out the spectrum in sub-gap region. In this region the condition of constant small quasi-Fermi level splitting is fulfilled and under conditions described in [2], photocurrent spectrum is proportional to the optical absorptance in the a-Si:H layer.

3.2 Total reflectance Quantification of reflectance of the rough aluminium foil is rather difficult due to the effects of both geometrical (macroscopic) and diffractive (microscopic) light scattering. In this case we cannot precisely define conditions of "specular reflectance" and so only the total reflectance can be measured. The FTIR spectrophotometer can be used for this task as well. The sample is placed inside the integration sphere equipped with Si photodiode. Since the sample is not transparent, the total reflectance is then directly measured.

4 Calculation In the case of thin layers on glass the Ritter-Weiser [7] approach for interference-free absorption coefficient evaluation can be used. The information about thickness and index of refraction is obtained from fit of standard reflectance spectra measured from glass side while the refraction index of refraction is analytically modelled by Cauchy formula $n(\lambda) = n_0 + n_1 / \lambda(\mu m)^2$.

In the case of layers on rough Al foil, the situation is complicated due to the scattering that cannot be easily treated by analytical formulae as in the first case. From the measured total reflectance R_{TOT} and absorptance A_{FTPS} (in relative units) spectra the absorption coefficient of a-Si:H layer has to be obtained. The spectrum of refraction index is assumed to be the same as in the case of layer on glass. We further proceed in three steps:

1) Total reflectance of bare substrates is measured and interface roughnesses and thicknesses of oxide layers (SnO_2, Al_2O_3) are estimated in order to reach accurate representation of the substrates in the optical model.

2) The total reflectance of a-Si:H layers is then measured and the thickness d, root mean square roughness σ_{RMS} and thickness of effective-medium layer (EMA) d_{EMA} is gained from the fit of the experimental values by numerical simulations. The use of the effective-medium layer, described e.g. in [8] is important to simulate reflectance reduction due to the nano-rough surfaces and have to be included especially in the case of reflectance on rough medium with high refraction index. Complex refraction index of EMA layer was calculated from simplified formula [8] from complex refraction indices of surrounding media as $\hat{n}_{EMA}^2 = (\hat{n}_1^2 + \hat{n}_2^2)/2$. Parameter σ_{RMS} is on the other hand used for simulation of light scattering (Scalar theory [9,10]) and elongation of light path and is therefore able to simulate also effects of roughness of larger dimensions. Some typical values of absorption coefficient together with

the refraction index of the sample on glass have to be taken also as the input into the simulation.

3) In the third step new values of d, σ_{RMS}, d_{EMA} are then used to obtain the true absorption coefficient from fit of measured A_{FTPS}. Semi-analytical formulae were used for absorption coefficient $(\alpha=4\pi k/\lambda)$: In the region of high absorption ($E>1.8$eV) Tauc-Lorentz formula [11] was used

$$2nk(E) = \frac{AE_0C(E-E_G)^2E^{-1}}{(E^2-E_0^2)^2+C^2E^2} ,$$

where parameters A, E_0, C, E_G are in units of energy. Parameter E_G comes from Tauc model and for correct fit can be attributed to standard parameter E_{OV}. Moreover the effect of saturation and also effect of recombination in blue range has to be considered.

The exponential ($\sim\exp(E/E_{Urbach})$) together with some hump attributed to defect absorption located around 1.2eV was used to describe the sub-gap region.

The simulation itself is realized by using numerical model CELL [9] that combines analytical calculations for non-scattered light with Monte-Carlo simulation for light scattered at rough interfaces. Recently we adapted the model for calculations of absorptance as low as 10^{-5}. Parameter variations are done manually.
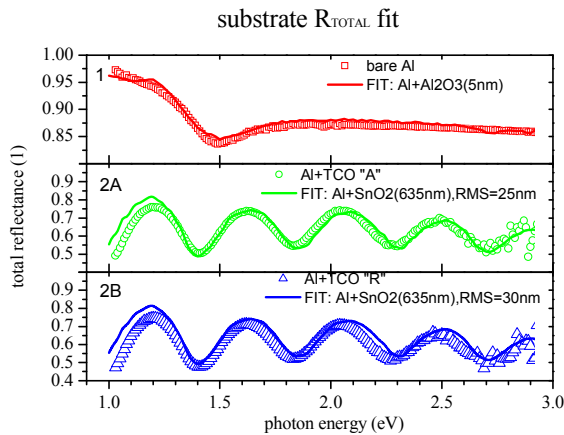
Figure 3 Numerical fit of total reflectances of bare aluminium and two types of aluminium foil covered with rough SnO$_2$. Symbols: experimental data, lines: numerical fit.

5 Results and discussions

5.1 Reflectance of substrates The parameters of SnO$_2$ layer were already known from preceding PDS measurements of the same layer deposited on rough Al and then transferred to glass. For substrate of sample 1 we found the best fit for tabulated data of Al plus 5nm layer of Al2O3 (represented by constant index of refraction $n=1.77$). For samples 2A and 2B only Al with SnO$_2$ layer was used and only σ_{RMS} was varied. We found the best fits for $\sigma_{RMS}=25$nm for Al foil "A" and $\sigma_{RMS}=30$nm for Al foil "R", see Figure 3. Thickness of SnO$_2$ layer was 635nm.

5.2 Reflectance of a-Si:H layers For samples 1, 2A and 2B we found the best reflectance fit for thicknesses 438nm, 390nm and 325nm respectively. The index of refraction was taken from measurement on glass, its Cauchy parameters are $n_0=3.43$, $n_1=0.36$. Thickness of EMA layer was 3nm for sample 1 and 10nm for samples 2A and 2B. See fitted curves in Figure 4. In the case of samples 2A, 2B the modelled curves have shallower interference minima compared to the experiment. We saw that such effect could be modelled by increase of SnO$_2$ refraction index that might happen as the effect of hydrogen plasma on SnO$_2$.
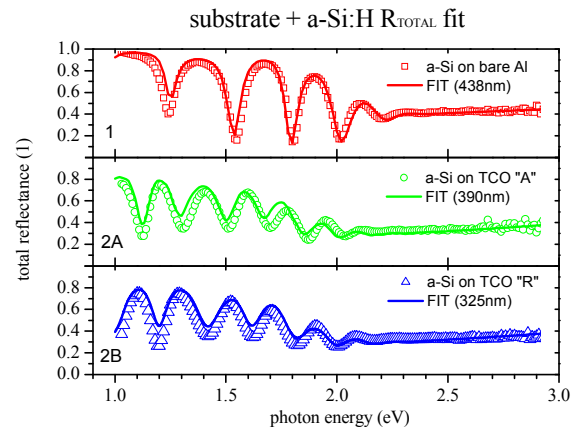

Figure 4 Numerical fit of a-Si:H layers on bare aluminium foil and two types of aluminium foil covered with rough SnO$_2$. Symbols: experimental data, lines: numerical fit.

5.3 FTPS spectra Fitted FTPS spectra are in Figure 5, resulting absorption coefficient curves are in Figure 6. Noise below 1.5eV in modelled curves is given by the effect of low absorption in the Monte-Carlo method.
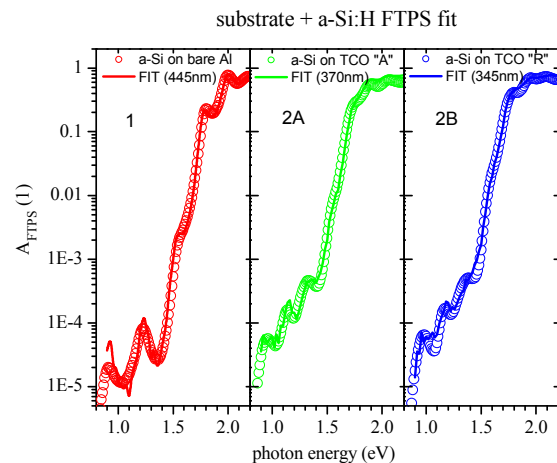
Figure 5 Numerical fit of absorptance (A_{FTPS}) of a-Si:H layers on bare aluminium foil and two types of aluminium foil covered with rough SnO$_2$. Symbols: experimental data, lines: numerical fit.

We also find a slightly different thicknesses, because FTPS and reflectance were not measured in the same spot. The curves were plotted only up to 2.2 eV where the saturation already occurs and the shape of absorption coefficient has practically no effect on FTPS spectra. Only the parameter E_G in Tauc-Lorentz formula was changed while keeping the other parameters at their typical values: A=27eV, E_0=3.92eV, C=2.81 eV.

calculated absorption coefficients
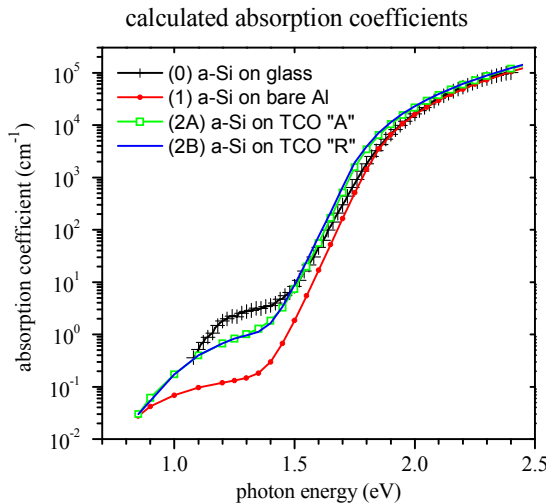
Figure 6 Comparison of calculated absorption coefficient of materials grown on glass, bare aluminium foil and two types of aluminium foils covered with SnO_2.

5.4 Sample comparison The resulting curves of absorption coefficient for all samples are compared in Figure 6. Some characteristic parameters of the curves are in Table 2. Parameter $\alpha_{1.2}$ is proportional to the defect density (N_{def}=2.4-5*10^{16}cm^{-2} *$\alpha_{1.2}$) [12], parameter E_{Urbach} is a measure of disorder.

Table 2 The fitted characteristic parameters of the absorption coefficient of a-Si:H fitted from FTPS measurement.

Sample no.	E_G (eV)	E_{1000} * (eV)	E_{Urbach} (meV)	$\alpha_{1.2}$ ** (cm^{-1})	thickness (nm)
0	1.71	1.77	52	1.8	328
1	1.71	1.78	44	0.12	445
2A	1.66	1.73	45	0.67	370
2B	1.65	1.72	46	0.67	345

* Photon energy at the point where α=1000cm^{-1}.

** absorption coefficient at 1.2eV

We conclude that in our experiment the a-Si:H had highest defect concentration and lowest growth rate when grown on bare glass compared to the quickest growth with the lowest defect concentration observed on bare aluminium. The aluminium itself is not that microscopically rough (nano-roughness is only in order of nm). Growth on

aluminium with substantially rougher TCO is something in between in terms of defect density and growth rate, but it gives material with substantially lower gap E_G.

6 Conclusion
First results of quality evaluation of thin a-Si:H films grown on aluminium foils and aluminium foils covered with rough SnO_2 by means of sub-gap photoconductivity measurement have been presented.

The difficulties with rough, conductive and non transparent substrate had been overcome by sandwich configuration with the use of electrolyte and by a numerical model of light propagation in the structure.

We have shown that optical properties, electronic quality and also growth rate of a-Si:H thin films grown under same conditions but on different substrates generally differ. The layer on glass showed the worst quality and slowest growth compared to other substrates. Best quality and fastest growth was observed on bare aluminium. We also observed noticeable shift in bandgap for rough SnO_2 compared to Al foil or glass.

References
[1] J. K. Rath et al., J. Non-Cryst. Solids 354, (2008) 2381
[2] M. Vanecek et al., Solid State Commun. **39**, pp. 1199-1202. (1981)
[3] M. Vanecek, A. Poruba, Appl. Phys. Lett. 80 (2002) 719.
[4] J. Melskens, G. van Elzakker, Y. Li, M. Zeman, Thin Solid Films 516 (2008) 6877
[5] M. Vanecek, A. Poruba, Thin Solid Films **515** pp. 7499–7503 (2007)
[6] R.B. Wehrspohn et al., Eur. Phys. J. B **8**, pp. 179 - 193 (1999)
[7] D. Ritter and K. Weiser, Opt. Commun. . **57** (5), pp. 336-338 (1986)
[8] D. Franta and I. Ohlídal, J. Opt. A: Pure Appl. Opt. **8**, pp. 763-774 (2006)
[9] J. Springer et al., J. Appl. Phys. **96**, (2004) 5329
[10] P. Beckmann, A. Spizzichino, The Scattering of Electromagnetic Waves from Rough Surfaces (London Pergamon 1963)
[11] G. E. Jellison, Jr. F. A. Modine, Appl. Phys. Lett. **69** (3), pp. 371-373 (1996)
[12] N. Wyrsch et al., J. Non-Cryst. Solids, **137-138**, pp. 347-350 (1991)

Organometallic Halide Perovskites: Sharp Optical Absorption Edge and Its Relation to Photovoltaic Performance

Stefaan De Wolf*†, Jakub Holovsky‡, Soo-Jin Moon§, Philipp Löper†, Bjoern Niesen†, Martin Ledinsky†‡, Franz-Josef Haug†, Jun-Ho Yum§, and Christophe Ballif†§

† Photovoltaics and Thin-Film Electronics Laboratory, Institute of Microengineering (IMT), Ecole Polytechnique Fédérale de Lausanne (EPFL), Maladière 71, Neuchâtel 2000, Switzerland

‡ Institute of Physics, Academy of Sciences of the Czech Republic, v. v. i., Cukrovarnická 10, 162 00 Prague, Czech Republic

§ PV Center, Centre Suisse d'Electronique et de Microtechnique (CSEM), Jacquet Droz 1, Neuchâtel 2000, Switzerland

*E-mail: stefaan.dewolf@epfl.ch.

Abstract
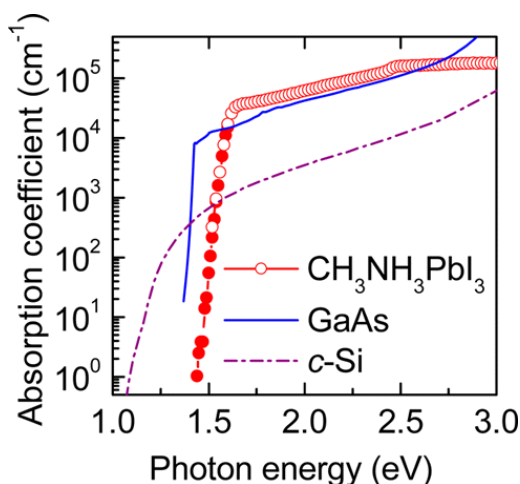
Solar cells based on organometallic halide perovskite absorber layers are emerging as a high-performance photovoltaic technology. Using highly sensitive photothermal deflection and photocurrent spectroscopy, we measure the absorption spectrum of $CH_3NH_3PbI_3$ perovskite thin films at room temperature. We find a high absorption coefficient with particularly sharp onset. Below the bandgap, the absorption is exponential over more than four decades with an Urbach energy as small as 15 meV, which suggests a well-ordered microstructure. No deep states are found down to the detection limit of ~1 cm^{-1}. These results confirm the excellent electronic properties of perovskite thin films, enabling the very high open-circuit voltages reported for perovskite solar cells. Following intentional moisture ingress, we find that the absorption at photon energies below 2.4 eV is strongly reduced, pointing to a compositional change of the material.

Keywords:

absorption; band edge; bandgap; perovskites; solar cells; stability; Urbach energy

Photocurrent Spectroscopy of Perovskite Layers and Solar Cells: A Sensitive Probe of Material Degradation

Jakub Holovský[*,†,‡] (iD), **Stefaan De Wolf**[§], **Jérémie Werner**[ǁ], **Zdeněk Remeš**[†], **Martin Müller**[†], **Neda Neykova**[†], **Martin Ledinský**[†], **Ladislava Černá**[‡], **Pavel Hrzina**[‡], **Philipp Löper**[ǁ], **Bjoern Niesen**[ǁ], **and Christophe Ballif**[ǁ]

[†] Institute of Physics, Czech Academy of Sciences, v. v. i., Cukrovarnická 10, 162 00 Prague, Czech Republic

[‡] Faculty of Electrical Engineering, Czech Technical University in Prague, Technická 2, 166 27 Prague, Czech Republic

[§] KAUST Solar Center (KSC), King Abdullah University of Science and Technology (KAUST), Thuwal 23955-6900, Saudi Arabia

[ǁ] Photovoltaics and Thin-Film Electronics Laboratory, Institute of Microengineering (IMT), École Polytechnique Fédérale de Lausanne (EPFL), Rue de la Maladière 71b, Neuchâtel 2000, Switzerland

*E-mail: holovsky@fzu.cz. Phone: +00420 220 318 516.

Abstract
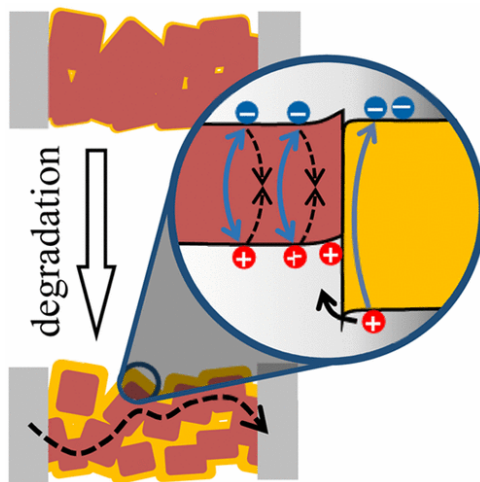
Optical absorptance spectroscopy of polycrystalline $CH_3NH_3PbI_3$ films usually indicates the presence of a PbI_2 phase, either as a preparation residue or due to film degradation, but gives no insight on how this may affect electrical properties. Here, we apply photocurrent spectroscopy to both perovskite solar cells and coplanar-contacted layers at various stages of degradation. In both cases, we find that the presence of a PbI_2 phase restricts charge-carrier transport, suggesting that PbI_2 encapsulates $CH_3NH_3PbI_3$ grains. We also find that PbI_2 injects holes into the $CH_3NH_3PbI_3$ grains, increasing the apparent photosensitivity of PbI_2. This phenomenon, known as modulation doping, is absent in the photocurrent spectra of solar cells, where holes and electrons have to be collected in pairs. This interpretation provides insights into the photogeneration and carrier transport in dual-phase perovskites.

Low-Temperature High-Mobility Amorphous IZO for Silicon Heterojunction Solar Cells

Monica Morales-Masis, Silvia Martin de Nicolas, Jakub Holovsky, Stefaan De Wolf, and Christophe Ballif

Abstract— **Parasitic absorption in the transparent conductive oxide (TCO) front electrode is one of the limitations of silicon heterojunction (SHJ) solar cells efficiency. To avoid such absorption while retaining high conductivity, TCOs with high electron mobility are preferred over those with high carrier density. Here we demonstrate improved SHJ solar cell efficiencies by applying high mobility amorphous indium zinc oxide (*a*-IZO) as the front TCO. We sputtered *a*-IZO at low substrate temperature and low power density, and investigated the optical and electrical properties as well as sub-band tail formation - quantified by the Urbach energy (E_U) – as a function of the sputtering oxygen partial pressure. We obtain an E_U as low as 128 meV for films with the highest Hall mobility of 60 cm²/Vs. When comparing the performance of *a*-IZO films with ITO and IO:H, we find that IO:H (115 cm²/Vs) exhibits a similar E_U of 130 meV, while ITO (25 cm²/Vs) presents a much larger E_U of up to 270 meV. The high film quality, indicated by the low E_U, the high mobility and low free carrier absorption of the developed *a*-IZO electrodes result in a significant current improvement, achieving conversion efficiencies over 21.5%, outperforming those with standard ITO.**

Index Terms—**amorphous indium zinc oxide, electron mobility, heterojunction, indium tin oxide, silicon, solar cells, transparent conductive oxides, Urbach energy.**

I. INTRODUCTION

Transparent conductive oxides (TCOs) used as front electrodes in solar cells should simultaneously feature high lateral electrical conductivity, low contact resistance with the adjacent layers, low optical absorption from the UV to the IR, and an appropriate refractive index for maximal light in-coupling. However, these properties may conflict with each other. For example, improving the conductivity by increasing the free carrier density inevitably leads to higher absorption in the IR. This explains the search for TCOs with high electron mobility [1-4]. Additionally, due to the presence of temperature sensitive layers in many solar cell designs (for example in thin-film silicon (Si) [5], Si heterojunction [6], CIGS [7], polymer [8] and perovskite solar cells [9]), low temperature deposition methods are needed, which might result in TCOs with amorphous structure. The intrinsic disorder of amorphous materials may, however, restrict the carrier mobility.

Several deposition techniques have been explored to fabricate high mobility TCOs at low temperatures, including, sputter deposition [10-12], chemical vapor deposition (CVD) [13], solution process [14] and atomic layer deposition (ALD) [15,16]. Among this variety of methods, sputtering is the most established deposition technique, despite the fact it can lead to damage of underlying layers [17]. 'Soft' sputtering can further mitigate this potential issue.

In this article, we study the properties of amorphous indium zinc oxide (*a*-IZO) thin films grown by RF sputtering as a high-mobility amorphous TCO. Using different oxygen partial pressures, we sputtered *a*-IZO films with a range of optoelectronic properties, and we study the correlations between its carrier mobility and Urbach energy, E_U. The latter parameter quantifies the combined broadening of conduction and valence band tails and scales directly with the degree of disorder or defects in a material [18-21].

To validate the use of *a*-IZO as front electrode, we also compared the performance of our *a*-IZO films with indium tin oxide (ITO) and hydrogenated indium oxide (IO:H), typically used as front electrodes in high efficiency *c*-Si heterojunction (SHJ) solar cells [6,22]. We found that the *a*-IZO films feature Urbach tails as low as the high-mobility (polycrystalline) IO:H. Furthermore, when applied as front electrodes in SHJ solar cells, the *a*-IZO front electrodes showed low contact resistance at the interface with the metal grids, representing an advantage over IO:H [22]. An improvement in the short-circuit current densities (J_{sc}) is also observed in comparison with the cells with polycrystalline ITO. In addition, whereas the ITO films require an annealing step of 200 °C to improve their optoelectronic properties, the *a*-IZO films present excellent properties already in the as-deposited state. This makes *a*-IZO attractive for a large range of temperature sensitive applications. Finally, we show that sputtered *a*-IZO

thin films, due to the high mobility, fulfill the requirements as a front electrode in SHJ solar cells enabling conversion efficiencies above 21.5%.

II. EXPERIMENTAL DETAILS

The *a*-IZO films were fabricated by RF sputtering of an IZO target (90 wt% In_2O_3 and 10 wt% ZnO) at a substrate temperature of 60 °C. The RF power density was 1.9 W/cm^2 and the oxygen to total flow ratio, $r(O_2)$ = $O_2/(Ar+O_2)$, introduced during the deposition was varied from 0.1% to 0.6%. All films were 100 ± 5 nm thick.

The ITO and IO:H samples were fabricated by DC and RF sputtering respectively under optimized oxygen conditions at room temperature. Details of the deposition parameters can be found in reference [22].

For the electrical and optical characterization of the films, the TCOs were deposited onto glass substrates, and for the photothermal deflection spectroscopy (PDS) measurements onto fused silica substrates. The TCOs were characterized before and after annealing (in air at 190 °C for 20 minutes), simulating the TCO properties after full SHJ solar cell fabrication [6].

The crystal structure of the films was analyzed by X-ray diffraction (XRD) using the grazing incidence (GI) mode. The electrical resistivity (ρ), carrier concentration (N_e) and Hall mobility (μ_{Hall}) were measured by Hall-effect in the van der Pauw configuration. The optical transmittance (T) and reflectance (R) of the films were measured by an UV-vis-NIR spectrometer with an integrating sphere, and the absorptance was determined from 100-T-R.

PDS was performed by an in-house developed system based on a 150W Xenon lamp. Fluorinert FC-72 was used as a temperature sensitive liquid. The principles of the PDS technique can be found in [23]. The transmittance and reflectance were measured simu

ltaneously, and the absorption coefficient was evaluated as described in [24], corrected for second order terms, whereas the refractive index was simulated by a Drude model in a form taken from [25]. The thickness and refractive index parameters were varied to obtain the best fit to the measured transmittance and reflectance data.

SHJ solar cells were fabricated on high quality n-type float zone (FZ) c-Si wafers (<100>; 250µm; 1-5 Ω•cm). The wafers were randomly textured in an alkaline solution, wet-chemically cleaned and dipped in hydrofluoric acid (HF) prior to plasma-enhanced chemical vapor deposition (PECVD) of intrinsic and doped hydrogenated amorphous silicon layers (*a*-Si:H). *a*-IZO or ITO films were used as the front electrode and deposited through a shadow mask (2×2 cm^2), defining the device size. On the rear side of the wafer a TCO layer was used in all devices, followed by a silver back reflector also sputtered immediately after the back TCO. A silver front grid was screen-printed on the front of the 4 TCO pads, and the solar cells were cured for 20 minutes at 190 °C. Further details about the fabrication process can be found elsewhere [6]. Finally, the complete solar cells were characterized by current-voltage (J-V) measurements on a sun simulator under Air Mass 1.5 global illumination.

III. RESULTS AND DISCUSSION

A. *a-IZO: Structural, Electrical and Optical Properties*

Figure 1 shows the GI-XRD patterns of the *a*-IZO films deposited with various $r(O_2)$. For all the samples, a broad peak centered at 2θ = 32° with an average full width at half maximum (FWHM) of 3.6° is observed. The large FWHM and the position of the peak indicate that the layers, as-deposited and annealed, are amorphous [11].

The electrical properties of the as-deposited and annealed *a*-IZO layers as a function of $r(O_2)$ are presented in Fig. 2a and b. As observed in Fig. 2a, the ρ does not change significantly except above $r(O_2)$ = 0.40%. This effect is given by the competing trends of N_e and μ_{Hall} (Fig. 2b). For the range of $r(O_2)$ studied, the N_e decreases with increasing $r(O_2)$, from 4.8 down to 0.2 x 10^{20} cm^{-3} for the as-deposited films. The annealed films follow the same trend. The μ_{Hall} reaches a maximum of 60 cm^2/Vs for $r(O_2)$ of 0.4%, above and below which it slightly drops. We furthermore plotted the dependence of μ_{Hall} with N_e in Fig. 2c. We observed an initial increase in μ_{Hall} with increasing N_e up to 2 x 10^{20} cm^{-3}. For N_e > 2 x 10^{20} cm^{-3}, μ_{Hall} decreases from 60 down to 40 cm^2/Vs. The rise and subsequent decrease of μ_{Hall} with N_e, could be explained by the presence of different scattering mechanisms. At low N_e (< 2 x 10^{20} cm^{-3}), possible μ_{Hall} limiting factors are potential barriers (percolation-type conduction) or lattice-scattering effects (phonon-like scattering) [26]. While for high N_e (> 2 x 10^{20} cm^{-3}) ionized impurity scattering is the main limiting factor of μ_{Hall} [10,27,28]. Lennheer *et al.* has shown that for *a*-IZO the maximum μ_{Hall} is achieved when carrier transport is mainly limited by phonon-scattering, i.e. metal-like transport and before ionized impurity scattering limits μ_{Hall} [28]. This maximum in μ_{Hall} is reached for a N_e of 1-2 x 10^{20} cm^{-3}, in accordance with our results. Fig. 2d displays the optical transmittance and absorptance of the *a*-IZO films with varying $r(O_2)$. All the films present a high transmittance (>75 %) in the visible and NIR region of the spectra. In the UV-Vis range we observe the well-known Burstein-Moss shift, i.e. a blue shift with increasing N_e (or decreasing $r(O_2)$) [29,30]. A clearer picture of the band-edge shift with increasing N_e is observed in the Tauc plot (Fig. 3a), discussed below. The optical absorptance of the films in the NIR strongly increases with decreasing $r(O_2)$. This is due to an increase in free carrier absorption associated with the increase in N_e. Note that the *a*-IZO $r(O_2)$ = 0.10% already shows higher absorptance in the Vis range compared to the rest of the layers.

Based on the previous measurements, we selected three *a*-IZO films with $r(O_2)$ = 0.10, 0.36 and 0.40% and measured by PDS. Results concerning their optical band gap (E_g), absorption coefficient (*a*) and Urbach energy (E_U) are presented in Fig. 3.

We evaluated E_g following the Tauc relation, $a \propto (hv-E_g)^x$, with *a* the absorption coefficient and *hv* the photon energy.

The value of the exponent x changes according to the nature of absorption transitions: $x = 1/2$ for allowed direct optical transitions, $x = 3/2$ for forbidden direct optical transitions, and $x = 2$ for indirect transitions [31]. For a-IZO, as well as several amorphous and crystalline TCOs, it has been demonstrated that electron momentum is largely conserved. Therefore, a direct band gap optical absorption model, with $a \propto (hv-E_g)^{1/2}$, closely describes the absorption edge of a-IZO [27,28,32,33].

The determined E_g values from the intercept of $a^2 = 0$ (Fig. 3a), for as-deposited as well as annealed films (the later indicated in parenthesis), are 3.6 eV (3.64 eV) for the sample with r(O$_2$) of 0.10%, 3.49 eV (3.52 eV) for r(O$_2$) of 0.36%, and 3.44 eV (3.48 eV) for r(O$_2$) of 0.40%. The measured E_g is in close agreement with values reported in the literature [10]. The band gap blue-shift with increasing N_e is described by the Burstein-Moss shift as commented earlier. There is no significant shift between the as-deposited and annealed samples, confirming the results from the Hall effect measurements. The refractive index (n) of the films show a shift towards lower n values with increasing N_e consistent with the Drude model.

We furthermore extracted E_U following the Urbach relation, $a=Aexp(-hv/E_U)$, where A and E_U are constants and E_U represents the width of the tail states. The fitted slope used to obtain E_U is indicated by points in Fig. 4a. It is clear from the plot that the slope steepens, and therefore E_U decreases, with increasing oxygen content in the film. The obtained E_U values range from 225 meV for the film with r(O$_2$) of 0.10% down to 128 meV for the film with r(O$_2$) of 0.4%.

Sub-band tails (quantified by E_U) are characteristic of disorder in amorphous semiconductors. For the specific case of TCOs, it is proposed that these tails are mainly caused at the valence band (VB) tail, and those tails at the conduction band (CB) are much smaller. The low tailing at the conduction band is explained by the spherical 4s or 5s orbitals of the metal atoms forming the CB, which are less sensitive to disorder than the O 2p orbitals forming the VB [26]. This contribution from CB and VB tails, though, cannot be separated from our optical measurements. Importantly, several recent reports [21,34,35] proposed that under-coordinated oxygen, formation of metal pairs (e.g. In-In, In-Zn) or even sub-nanometer metal inclusions in amorphous TCOs will induce tail-like optical absorptions as well as deep defect levels close to the VB and CB edge [21,35,36]. The formation of sub-nanometer scale metal clusters inside the amorphous matrix, might affect the average atomic coordination, i.e. locally modify the structural properties of the films [37] influencing E_U. The formation of metal pairs or inclusions within the amorphous TCO matrix will also limit the carrier mobility due to electron scattering. This could explain why with increasing oxygen content, the formation of metal inclusions is reduced and the mobility of the films improves. Increasing the oxygen content will then allow the μ_{Hall} improvement, as observed in Fig. 2.b for r(O$_2$) < 0.4, and the decrease in E_U as commented above. While this correlation is clearly observed in Fig. 4b, further studies are required to evaluate this preliminary conclusion and a complete analysis

on this topic will be presented elsewhere.

B. Comparison with ITO and IO:H

In this section we compare the studied a-IZO thin films to ITO and IO:H, typically used as front electrodes in SHJ solar cells [6,22].

For this comparison, all the films have similar N_e after the annealing step, optimized to achieve low optical absorptance in the IR (Fig. 5), and the same thickness (100 ± 5 nm on glass), optimized to reduce reflectance losses with a reflection minimum near 600 nm when used on our textured SHJ solar cells [38].

The sheet resistance (R_{sh}) of the layers is different for the three TCOs due to their different μ_{Hall}. The maximum μ_{Hall} after annealing is found for IO:H with 115 cm^2/Vs, followed by a-IZO (r(O$_2$) = 0.40%) with 60 cm^2/Vs and finally ITO with the lowest μ_{Hall} of 25 cm^2/Vs. The overview of the electrical properties of the ITO, IO:H and a-IZO films, before and after annealing, is presented in Table 1. Note that while ITO and IO:H are both polycrystalline after the annealing step, the IZO films remain amorphous (Fig. 6).

It is worth noting from Table 1 and Fig. 5 that a-IZO presents excellent optoelectronic properties already from the as-deposited step, presenting an advantage over IO:H and ITO. Considering also that the deposition is performed at substrate temperatures below 60 °C and at low power densities, a-IZO presents ideal properties for application in several temperature and damage sensitive technologies, like polymer and perovskite solar cells, flexible and paper electronics among others.

We furthermore performed PDS measurements of the ITO and IO:H samples, before and after annealing. The summary of the extracted E_g and E_U for each of the films and their comparison with the a-IZO films are presented in Fig. 7a and 7b respectively.

Starting with E_g, we observed a shift to larger gaps for both ITO and IO:H after annealing. While for ITO the shift of E_g to higher energies can be attributed to the Burstein Moss shift due to the increase in N_e with annealing (Table 1), in IO:H the shift of E_g to higher energies cannot be attributed to the same effect. Instead this shift may be caused by the amorphous to crystalline phase transition induced by the annealing step at 190 °C [12,39]. This phase change is clearly seen in the XRD data presented in Fig. 7. Note that for a-IZO and ITO no phase change is observed. Finally, the a-IZO films only present a small shift in E_g after annealing.

Following with the Urbach tail, we found the largest E_U for ITO in the as-deposited state, with only a small drop from 300 to 270 meV after annealing. As proposed previously by several groups, the incorporation of Sn into In$_2$O$_3$ leads to severely extended tail states in ITO [40], similar to the case of SnO$_2$ [41]. The extended tail states have been explained mainly as originating from ionized impurities, although other mechanisms like phonon scattering and excitonic effects have also been considered [40]. Remarkably, although the presence of the extended tail states has been widely commented in literature, to our knowledge, there are no reports of measured E_U values for sputtered ITO.

Contrary to ITO, we measured much lower E_U values for IO:H, which are very close to those measured for a-IZO with

r(O_2) = 0.40%. The lowest E_U achieved is 130 meV for IO:H and 128 meV for a-IZO. We note that IO:H does not present a strong shift in E_U before and after annealing regardless of the phase transition from the amorphous to the polycrystalline phase (Fig. 6), which may be surprising. The high mobility of IO:H and its crystallization after annealing suggest passivation of defects and/or decrease disorder in the films, and therefore a clear lowering of E_U was expected. More investigations would be required to explain these results. It is also important to note that we achieve similar E_U values for a-IZO and IO:H, although IO:H presents μ_{Hall} twice as large as that of the a-IZO at r(O_2) = 0.40%. This together with the advantage that a-IZO presents excellent optoelectronic properties already from the as-deposited state, confirms the strong potential of a-IZO as a replacement for ITO and/or IO:H as a front electrode for solar cells.

C. Application of a-IZO as Front Contact for SHJ Solar Cells

To validate the potential of a-IZO as transparent electrode for solar cells, we fabricated SHJ solar cells and used the a-IZO films with r(O_2) = 0.10; 0.36; 0.40% as the front TCO contact. The solar cell configuration is shown in Fig. 8a. The short-circuit current density (J_{sc}), open-circuit voltage (V_{oc}), fill factor (FF) and efficiency results are shown in Fig. 8. A reference device with front ITO is also shown for comparison.

The J_{sc} of the a-IZO-based devices, increases with increasing r(O_2). Indeed, as observed in Fig. 2d, the a-IZO layers with lower oxygen ratios feature higher free carrier absorption causing parasitic losses in the device. The observed Burstein-Moss effect does not compensate these J_{sc} losses in the final device. In spite of the enhanced optical properties of the a-IZO films with higher r(O_2), the electrical properties behave in the opposite direction, causing electrical losses in the device. FF decreases for the film with the higher oxygen content, r(O_2) = 0.40%, which is well correlated with the decreasing N_e trend presented in Fig. 2b. However, the FF values for the three cells are still high and suggest a good contact resistance between the a-Si and the metal grid. This is an advantage over IO:H-based devices as reported in [22]. In comparison with the ITO-based devices, the a-IZO devices present a clear advantage mainly on improved J_{sc} (Fig. 8b). In addition, the lower R_{sh} of a-IZO (35, 40 and 50 Ω/sq for the films with r(O2) = 0.1%, 0.36% and 0.4% respectively) as compared to that of ITO (100 Ω/sq), would allow a further increase of the pitch size of the front metal grid electrode and with it an even further improvement in J_{sc} is expected for the a-IZO devices [42,43].

Finally, the best J_{sc}-FF compromise is found with the device featuring an a-IZO film with r(O_2) = 0.36%, achieving an energy conversion efficiency of 21.5 %.

Comparing the results of the a-IZO cells with the record IO:H-based SHJ device reported by L. Barraud *et al.* [22], no marked difference is observed in the J_{sc} of both cells. This is expected due to the low optical absorptance of IO:H and a-IZO (Fig. 5). Both devices have the same configuration and were fabricated in the same laboratory. The reported IO:H cells have J_{sc} values of 38.9 mA/cm², while the maximum J_{sc} of the a-IZO cells reported in this work is of 38.6 mA/cm². The main advantage of the front a-IZO electrodes in

comparison with the IO:H-front electrodes is that the former can be deposited on a single step process, it doesn't require of a capping layer to achieve good contact resistance with the metal grid, and it presents higher stability under damp heat conditions [44].

These results clearly demonstrate that the a-IZO films developed within this work present excellent performance as a front TCO contact in high-efficiency SHJ solar cells.

IV. CONCLUSION

In summary, we have shown the influence on the carrier transport properties and sub-band tail formation of the oxygen partial pressure applied during sputtering deposition of a-IZO thin films. With increasing the oxygen partial pressure, the Hall mobility increases while E_U decreases. The highest mobility achieved for the a-IZO films is 60 cm²/Vs, corresponding to an E_U of 128 meV. Comparing to ITO and high mobility IO:H, a-IZO presents a much lower E_U and Hall mobility than ITO, while it presents similar E_U than IO:H, although IO:H is polycrystalline and has a higher mobility compared to a-IZO. When applied as front contact in SHJ solar cells, a-IZO presents the advantage of good contact resistance with the front metal grids contrary to the IO:H, and an improved J_{sc} as compared to the cells with ITO. The low temperature deposition and excellent optoelectronic properties of a-IZO already from the as-deposited state makes this an excellent front electrode for SHJ solar cells and a wide range of temperature sensitive devices like flexible OLEDs and perovskite solar cells.

REFERENCES AND FOOTNOTES

[1] H. Fujiwara and M. Kondo, "Effects of carrier concentration on the dielectric function of ZnO:Ga and In₂O₃:Sn studied by spectroscopic ellipsometry: Analysis of free-carrier and band-edge absorption", *Phys. Rev. B,* vol. 71, pp. 075109-1- 075109-10, Feb. 2005.
[2] S. Calnan and A. N. Tiwari, "High mobility transparent conducting oxides for thin film solar cells", *Thin Solid Films*, vol. 518, pp. 1839-1849, Jan. 2010.
[3] Z. C. Holman M. Filipic, A. Descoeudres, S. De Wolf, F. Smole, M. Topic, and C. Ballif, "Infrared light management in high-efficiency silicon heterojunction and rear-passivated solar cells", *J. Appl. Phys.*, vol. 113, pp. 013107-1 -013107-13, Jan. 2013.
[4] K. M. Yu, M. A. Mayer, D. T. Speaks, H. He, R. Zhao, L. Hsu, S. S. Mao, E. E. Haller, and W. Walukiewicz, "Ideal transparent conductors for full spectrum photovoltaics", *J. Appl. Phys.*, vol. 111, pp. 123505-1 -123505-5, Jun. 2012.

[5] A. Shah, P. Torres, R. Tscharner, N. Wyrsch, and H. Keppner, "Photovoltaic technology: The case for thin-film solar cells", *Science*, vol. 285, pp. 692-698, July 1999.

[6] S. De Wolf, A. Descoeudres, Z. C. Holman, and C. Ballif, "High-efficiency silicon heterojunction solar cells: a review", *Green*, vol. 2, pp. 7-24, Feb. 2012.

[7] H. Hagendorfer, K. Lienau, S. Nishiwaki, C. M. Fella, L. Kranz, A. R. Uhl, D. Jaeger, L. Luo, C. Gretener, S. Buecheler, Y. E. Romanyuk, and A. N. Tiwari, "Highly transparent and conductive ZnO:Al thin films from a low temperature aqueous solution approach", *Adv. Mater.,* vol. 26, pp. 632-636, 2014.

[8] G. Li, R. Zhu, and Y. Yang, "Polymer solar cells", *Nat. Photonics*, vol. 6, pp. 153-161, Feb. 2012.

[9] J. Burschka, N. Pellet, S. J. Moon, R. Humphry-Baker, P. Gao, M. K. Nazeeruddin, and M. Gratzel, "Sequential deposition as a route to high-performance perovskite-sensitized solar cells", *Nature,* vol. 499, pp. 316-319, Jul. 2013.

[10] R. Martins, P. Almeida, P. Barquinha, L. Pereira, A. Pimentel, I. Ferreira, and E. Fortunato, "Electron transport and optical characteristics in amorphous indium zinc oxide films", *J. Non-Cryst. Solids*, vol. 352, pp. 1471-1474, Jun. 2006.

[11] M. P. Taylor, D. W. Readey, M. van Hest, C. W. Teplin, J. L. Alleman, M. S. Dabney, L. M. Gedvilas, B. M. Keyes, B. To, J. D. Perkins, and D. S. Ginley, "The remarkable thermal stability of amorphous In-Zn-O transparent conductors", *Adv. Funct. Mater.,* vol. 18, pp. 3169-3178, Oct. 2008.

[12] T. Koida, M. Kondo, K. Tsutsumi, A. Sakaguchi, M. Suzuki, and H. Fujiwara, "Hydrogen-doped In_2O_3 transparent conducting oxide films prepared by solid-phase crystallization method", *J. Appl. Phys.*, vol. 107, pp. 033514 (2010).

[13] L. Ding, S. Nicolay, J. Steinhauser, U. Kroll, and C. Ballif, "Relaxing the Conductivity/Transparency Trade-Off in MOCVD ZnO Thin Films by Hydrogen Plasma", *Adv. Funct. Mater.*, vol. 23, pp. 5177–5182, May 2013.

[14] R. M. Pasquarelli, D. S. Ginley and R. O'Hayrea, "Solution processing of transparent conductors: from flask to film", *Chem. Soc. Rev.*, vol. 40, pp. 5406–5441, Mar. 2011.

[15] J. A. Libera, J. N. Hryn and J. W. Elam, "Indium Oxide Atomic Layer Deposition Facilitated by the Synergy between Oxygen and Water", *Chem. Mater*, pp. 2150-2158, Mar. 2011.

[16] B. Macco, Y. Wu, D. Vanhemel and W. M. M. Kessels, "High mobility In_2O_3:H transparent conductive oxides prepared by atomic layer deposition and solid phase crystallization", *Phys. Status Solidi RRL*, pp. 987-990, Oct. 2014.

[17] B. Demaurex, J. P. Seif, S. Smit, B. Macco, W. M. M. Kessels, J. Geissbuhler, S. De Wolf, and C. Ballif, "Atomic-Layer-Deposited Transparent Electrodes for Silicon Heterojunction Solar Cells", *IEEE J. Photovolt.*, vol. 4, pp. 1387-1396, Nov. 2014.

[18] J. I. Pankove, "Absorption edge of impure gallium arsenide", *Phys. Rev.*, vol. 140, pp. A2059-A2065, Dec. 1965.

[19] F. Urbach, "The long-wavelength edge of photographic sensitivity and of the electronic absorption of solids", *Phys. Rev.*, vol. 92, pp. 1324, Oct. 1953.

[20] S. Schonau, F. Ruske, S. Neubert, and B. Rech, "Analysis of Urbach-like absorption tails in thermally treated ZnO:Al thin films", *Appl. Phys. Lett.*, vol. 103, pp. 192108-1 - 192108-4, Nov. 2013.

[21] K. Nomura, T. Kamiya, H. Yanagi, E. Ikenaga, K. Yang, K. Kobayashi, M. Hirano, and H. Hosono, "Subgap states in transparent amorphous oxide semiconductor, In-Ga-Zn-O, observed by bulk sensitive x-ray photoelectron spectroscopy", *Appl. Phys. Lett.*, vol. 92, pp. 2202117-1 -2202117-3, May 2008.

[22] L. Barraud, Z. C. Holman, N. Badel, P. Reiss, A. Descoeudres, C. Battaglia, S. De Wolf, and C. Ballif, "Hydrogen-doped indium oxide/indium tin oxide bilayers for high-efficiency silicon heterojunction solar cells", *Sol. Energy Mater. Sol. Cells*, vol. 115, pp. 151-156, Aug. 2013.

[23] A. C. Boccara, D. Fournier, and J. Badoz, "Thermo-optical spectroscopy: Detection by the "mirage effect"", *Appl. Phys. Lett.*, vol. 36, pp. 130-132, Jan.1980.

[24] D. Ritter and K. Weiser, "Suppression of interference fringes in absorption measurements on thin films", *Opt. Commun.*, vol 57, pp. 336-338, Apr. 1986.

[25] K. Postava, H. Sueki, M. Aoyama, T. Yamaguchi, K. Murakami, and Y. Igasaki, "Doping effects on optical properties of epitaxial ZnO layers determined by spectroscopic ellipsometry", *Appl. Surf. Sci.*, vol. 175-176, pp. 543-548, May 2001.

[26] H. Hosono, "Ionic amorphous oxide semiconductors: Material design, carrier transport, and device application", *J. Non-Cryst. Solids*, vol. 352, pp. 851–858, Apr. 2006.

[27] T. Koida, H. Shibata, M. Kondo, K. Tsutsumi, A. Sakaguchi, M. Suzuki, and H. Fujiwara, "Correlation between oxygen stoichiometry, structure, and opto-electrical properties in amorphous In_2O_3:H films", *J. Appl. Phys.*, vol. 111, pp. 063721-1 -063721-7, Mar. 2012.

[28] A. J. Leenheer, J. D. Perkins, M. F. A. M. van Hest, J. J. Berry, R. P. O'Hayre, and D. S. Ginley, "General mobility and carrier concentration relationship in transparent amorphous indium zinc oxide films", *Phys. Rev. B.*, vol. 7, pp. 115215-1 – 115215-5, Mar. 2008.

[29] E. Burstein, "Anomalous optical absorption limit in InSb", *Phys. Rev.*, vol. 93, pp. 632-633, Dec. 1953.

[30] T. S. Moss, "The interpretation of the properties of indium antimonide", *Proc. Phys. Soc. B.*, vol. 67, pp. 775-782, Jun. 1954.

[31] J. I. Pankove, *Optical Processes in Semiconductors*, Dover, New York, 1971.

[32] J. R. Bellingham, W. A. Phillips, and C. J. Adkins, "Electrical and optical-properties of amorphous indium oxide", *J. Phys. Condens. Matter.*, vol. 2, pp. 6207-6221, Apr. 1990.

[33] A. Walsh, J. L. F. Da Silva, S.-H. Wei, C. Körber, A. Klein, L. F. J. Piper, A. DeMasi, K. E. Smith, G. Panaccione, P. Torelli, D. J. Payne, A. Bourlange, and R. G. Egdell, "Nature of the band gap of In_2O_3 revealed by first-principles calculations and x-ray spectroscopy", Phys. Rev. Lett., vol. 100, pp. 167402-1 – 167402-4, Apr. 2008.

[34] T. Kamiya, K. Nomura, M. Hirano, and H. Hosono, "Electronic structure of oxygen deficient amorphous oxide semiconductor a-InGaZnO$_{4-x}$: Optical analyses and first-

principle calculations", *Phys. Stat. Sol. (c)*, vol. 5, pp. 3098-3100, Jun. 2008.

[35] W. Korner, D. F. Urban, and C. Elsasser, "Origin of subgap states in amorphous In-Ga-Zn-O", *J. Appl. Phys.*, vol. 114, pp. 163704-1 -163704-6, Oct. 2013.

[36] W. Körner, D. F. Urban and C. Elsässer, "Generic origin of subgap states in transparent amorphous semiconductor oxides illustrated for the cases of In–Zn–O and In–Sn–O", *Phys. Status Solidi A*, pp. 1-6, Feb. 2015.

[37] R. Khanal, D. B. Buchholz, R. P. H. Chang, and J. E. Medvedeva, "Composition-dependent structural and transport properties of amorphous transparent conducting oxides", Phys. Rev. B, vol. 91, pp. 205203-1 – 205203-13, May 2015.

[38] Z. C. Holman A. Descoeudres, L. Barraud, F. Z. Fernandez, J. P. Seif, S. De Wolf, and C. Ballif, "Current losses at the front of silicon heterojunction solar cells", *IEEE J. Photovolt.*, vol. 2, pp. 7-15, Jan. 2012.

[39] H. F. Wardenga, M. V. Frischbier, M. Morales-Masis, A. Klein, "*In Situ* Hall Effect Monitoring of Vacuum Annealing of In$_2$O$_3$:H Thin Films," *Materials*, vol. 8, pp. 561-574, Feb. 2015.

[40] I. Hamberg and C. G. Granqvist, "Evaporated Sn-doped In$_2$O$_3$ films - Basic optical properties and applications to energy-efficient windows", *J. Appl. Phys.*, vol. 60, pp. R123-R159, Aug. 1986.

[41] F. J. Arlingha, "Energy-bands in stannic oxide (SnO$_2$)", *J. Phys. Chem. Solids*, vol. 35, pp. 931-935, May 1974.

[42] J. Geissbühler, S. De Wolf, A. Faes, N. Badel, Q. Jeangros, A. Tomasi, L. Barraud, A. Descoeudres, M. Despeisse, and C. Ballif, "Silicon heterojunction solar cells with copper-plated grid electrodes: status and comparison with silver thick-film techniques", *IEEE J. Photovolt.*, vol. 4, pp. 1055-1062, Jul. 2014.

[43] M. Bivour, S. Schröer, M. Hermle, and S. W. Glunz, "Silicon heterojunction rear emitter solar cells: Less restrictions on the optoelectrical properties of front side TCOs", *Sol. Energy Mater. Sol. Cells*, vol. 122, pp. 120-129, Mar. 2014.

[44] T. Thosophon, S. De Wolf, M. Morales-Masis, and C. Ballif, "Stability of sputtered indium-oxide based electrodes", in preparation.
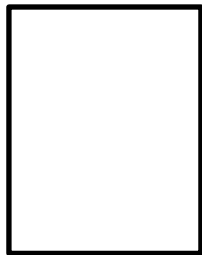
Monica Morales-Masis received the Ph.D. degree from Leiden University, Leiden, The Netherlands in January 2012, focusing on mixed conductor materials and resistive switching memories. In September 2012 she joined the Photovoltaics and Thin-Film Electronics Laboratory, Ecole Polytechnique Fédérale de Lausanne (EPFL), Neuchâtel, Switzerland. Nowadays she is Team Leader for activities on transparent conductive oxides. Her current research interests include the fundamental investigation, design, fabrication and application of transparent conductive oxides for optoelectronic devices, including solar cells and light emitting diodes.

Silvia Martin de Nicolas Agut received the M.Sc. and Industrial Engineering degree in 2009 from Universitat Politècnica de Catalunya, Barcelona, Spain, focusing on renewable energies engineering. From 2009 to 2012 she was with the French National Institute for Solar Energy (CEA-INES), Le-Bourget-du-Lac, France, where she carried out her Ph.D. on silicon heterojunction technology. In 2012 she received her Ph.D. degree in Physics from Université Paris XI, France. In 2013 she joined the Photovoltaics and Thin-Film Electronics Laboratory, École Polytechnique Fédérale de Lausanne, Neuchâtel, Switzerland, as a Postdoctoral Researcher, where she is working on high-efficiency silicon heterojunction devices.
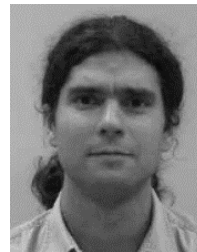
Jakub Holovsky received the Ph.D. degree in 2012 from Charles University in Prague, Czech Republic, while he pursued the scientific work at Institute of Physics, Academy of Sciences of The Czech Republic v. v. i. and at Photovoltaics and Thin-Film Electronics Laboratory, Ecole Polytechnique Fédérale de Lausanne, Neuchâtel, Switzerland, where he also spent one year as a SCIEX post-doc fellow. Since 2014 he teaches at Czech Technical University in Prague. He is focused on low absorption characterization methods for photovoltaic materials.

Stefaan De Wolf received the Ph.D. degree from the Catholic University of Leuven, Leuven, Belgium, while he was with Interuniversity Microelectronics, Leuven, focusing on crystalline silicon solar cells. From 2005 to 2008, he was with the National Institute of Advanced Industrial Science and Technology, Tsukuba, Japan, focusing on silicon heterojunction devices. In 2008, he joined the Photovoltaics and Thin-Film Electronics Laboratory, Ecole Polytechnique Fédérale de Lausanne, Neuchâtel, Switzerland, as a Team Leader for activities on such solar cells.

Christophe Ballif received the Graduate's degree in physics and Ph.D. degree from Ecole Polytechnique Fédérale de Lausanne (EPFL), Lausanne, Switzerland, in 1994 and 1998, respectively, focusing on novel photovoltaic materials. He was a Postdoctoral Researcher at National Renewable Energy Laboratory, Golden, CO, where he was involved in compound semiconductor solar cells (CIGS and CdTe). He then was with the Fraunhofer

Institute for Solar Energy Systems, Freiburg, Germany, where he was involved in crystalline silicon photovoltaics (monocrystalline and multicrystalline) until 2003. He then joined the Swiss Federal Laboratories for Materials Testing and Research, Thun, Switzerland, before becoming a Full Professor and Chair at the Institute of Microengineering, University of Neuchâtel, Neuchâtel, Switzerland, in 2004. In 2009, the Institute was transferred to EPFL. He is the Director of the Photovoltaics and Thin-Film Electronics Laboratory within the Institute as well as of the CSEM PV-center. His research interests include thin-film solar cells, high-efficiency heterojunction crystalline cells, and module technology, contributing to technology transfer and industrialization of novel devices.
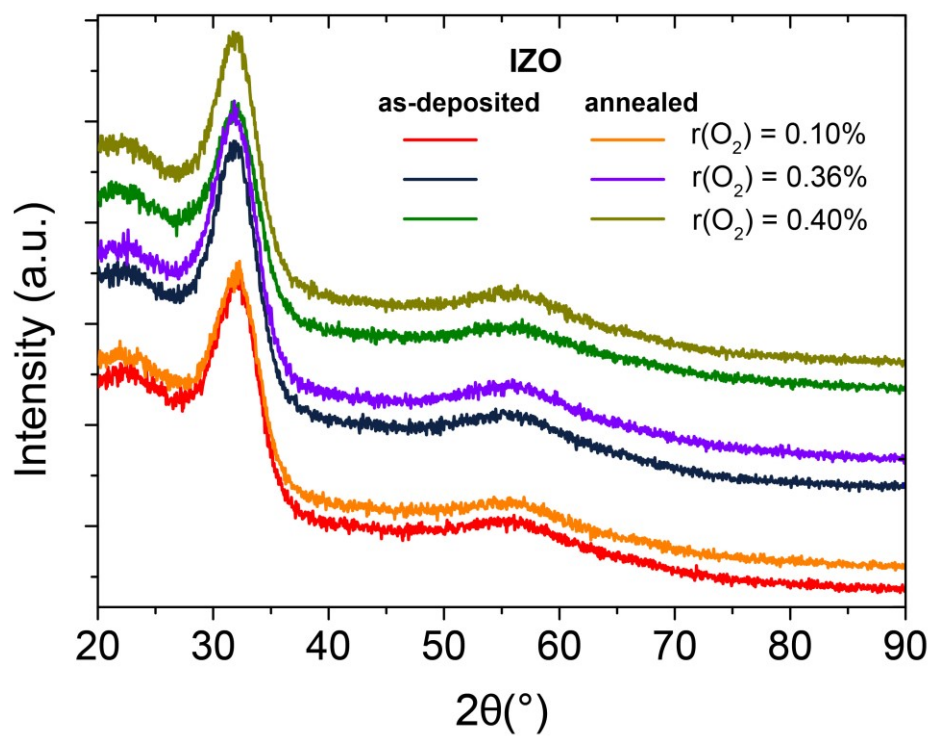
Fig. 1. GI-XRD patterns of *a*-IZO films on glass substrates with different oxygen partial pressures. Data is offset for clarity.
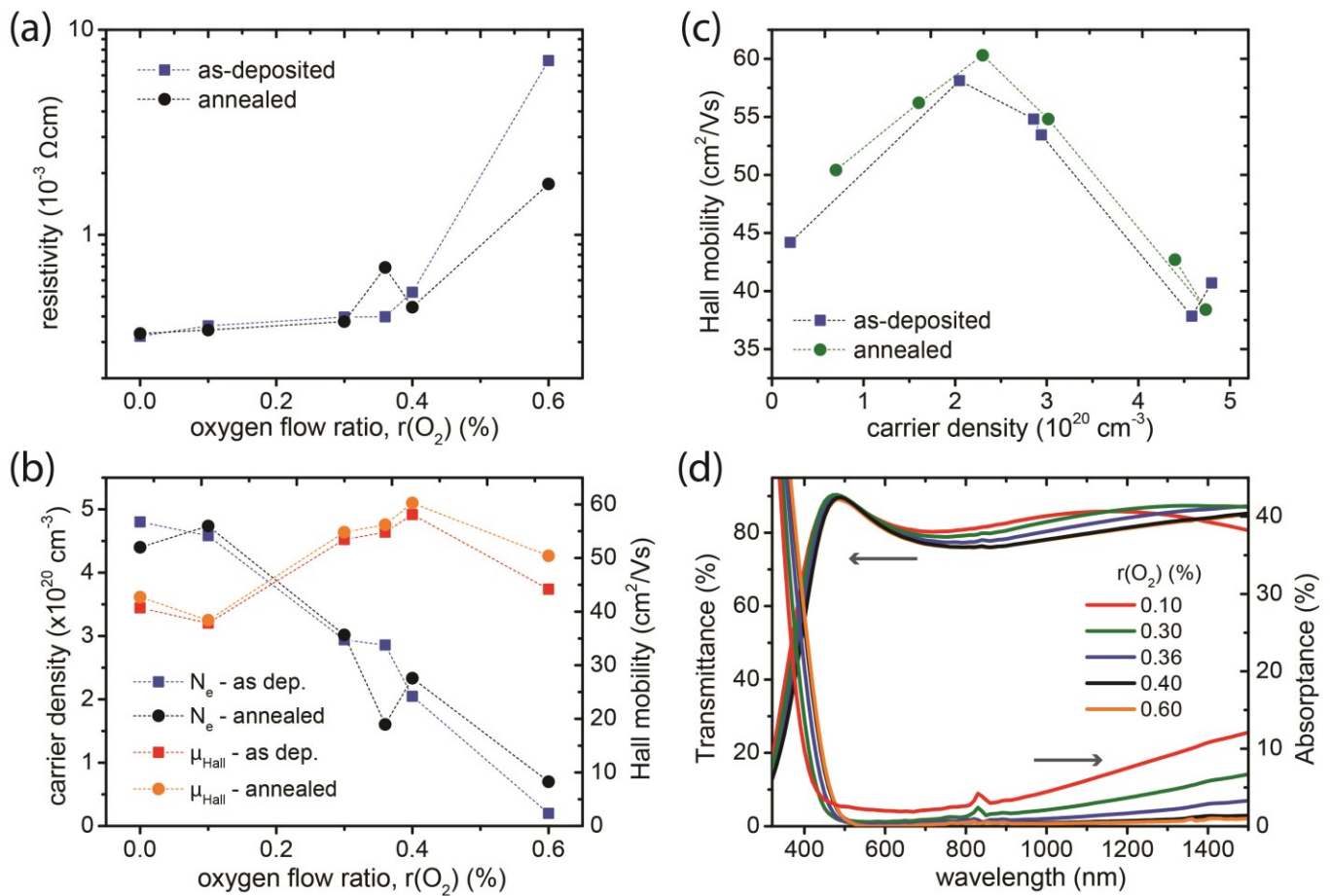
Fig. 2. a) Resistivity, b-c) carrier density and hall mobility and d) optical transmittance and absorptance of the *a*-IZO films with varying oxygen flow ratios r(O$_2$) during sputtering deposition.
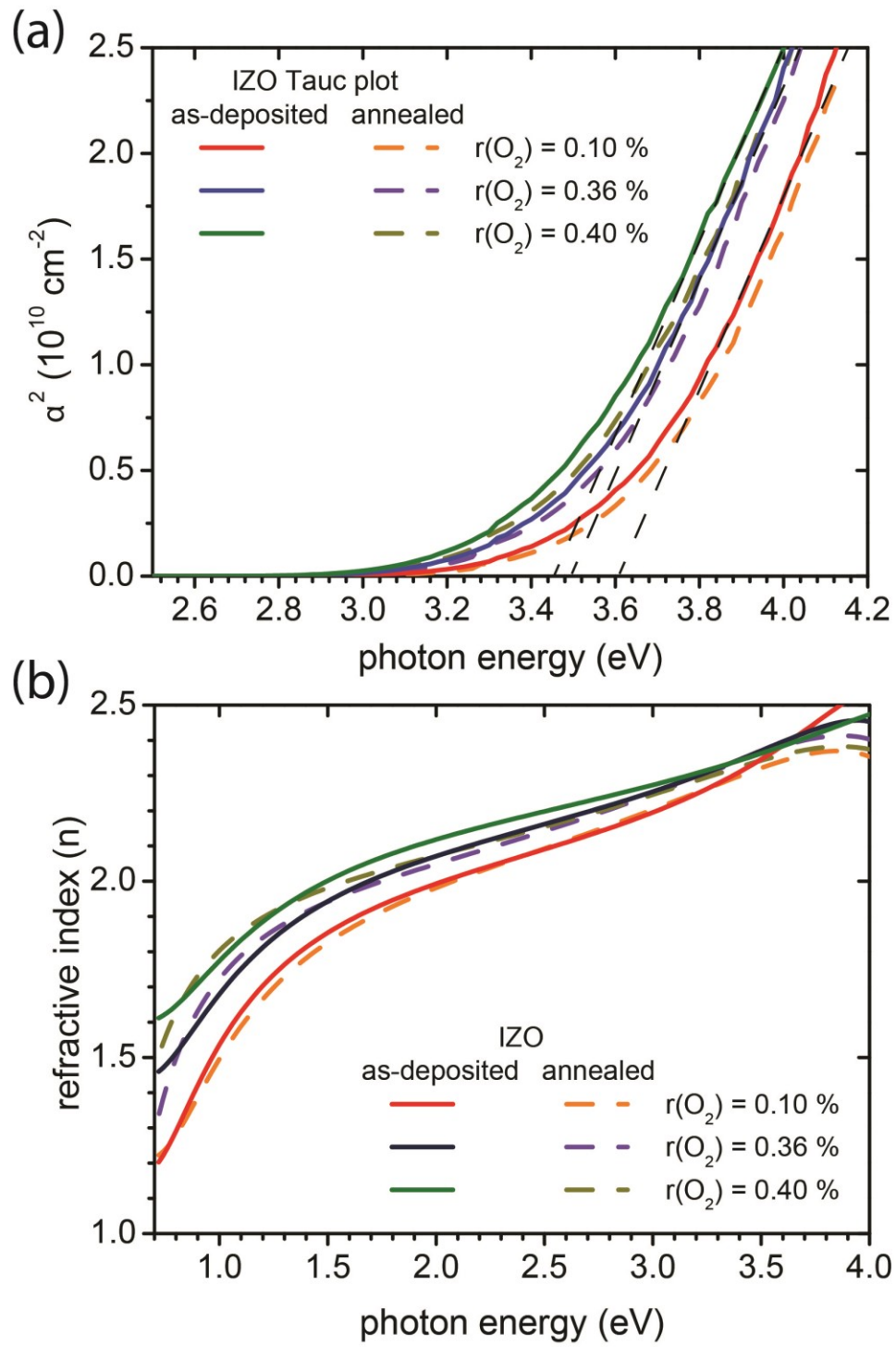
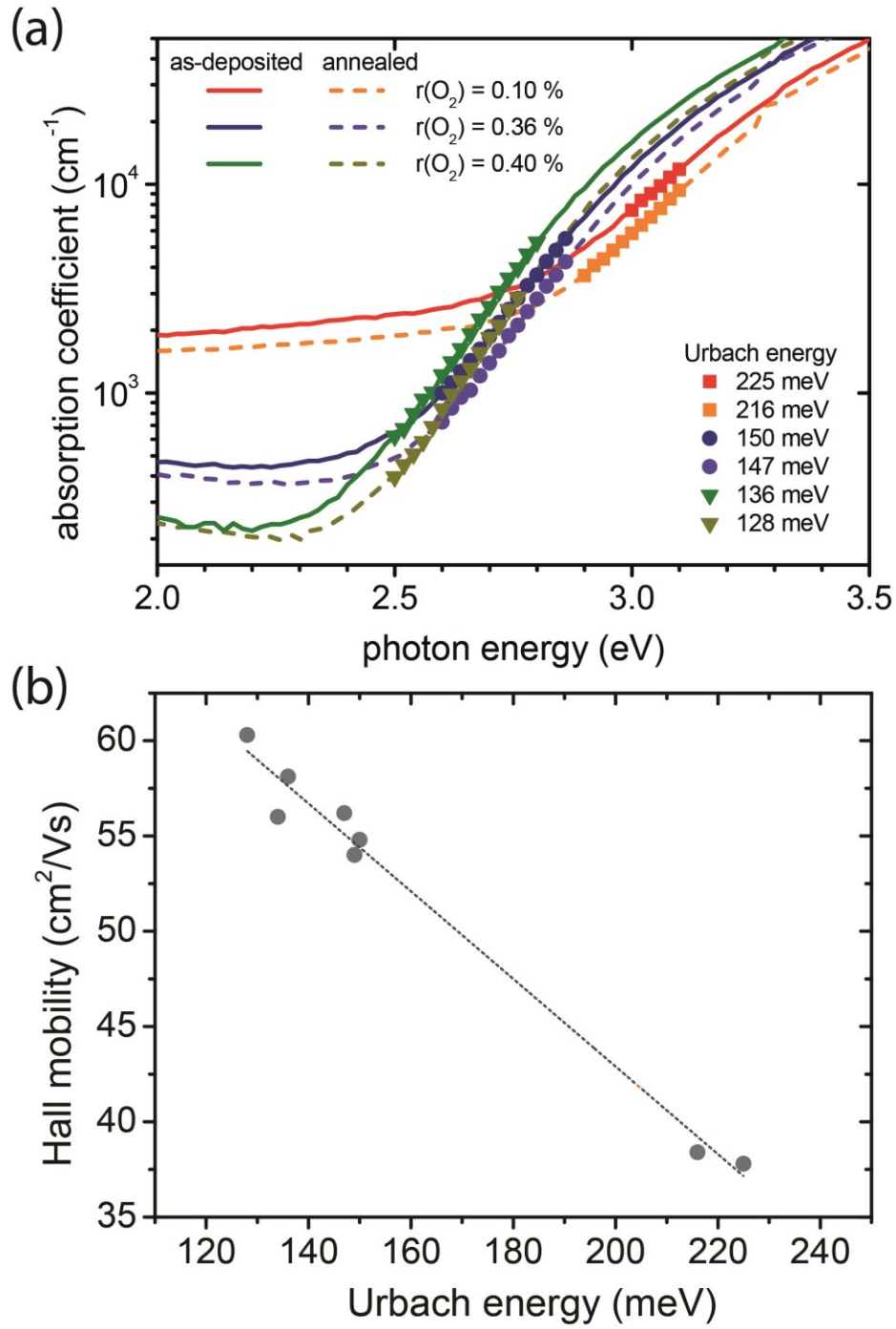Fig. 3. a) Tauc plot and b) refractive index of the *a*-IZO thin films with varying oxygen flow ratio r(O₂).

Fig. 4. a) Absorption band edge of *a*-IZO thin films with varying oxygen flow ratio r(O₂). The round symbols indicate the slope used to extract the Urbach energy values for each sample. b) Relation between the Hall mobility and Urbach energy for the *a*-IZO layer.
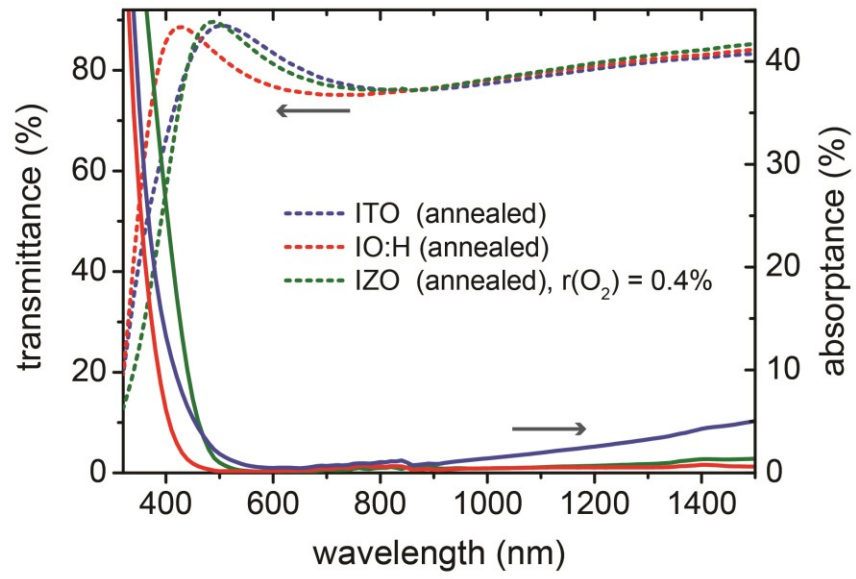
Fig. 5. Optical transmittance and absorptance of ITO, IO:H and *a*-IZO thin films.

Table 1 Electrical properties of ITO, IO:H and a-IZO thin films.

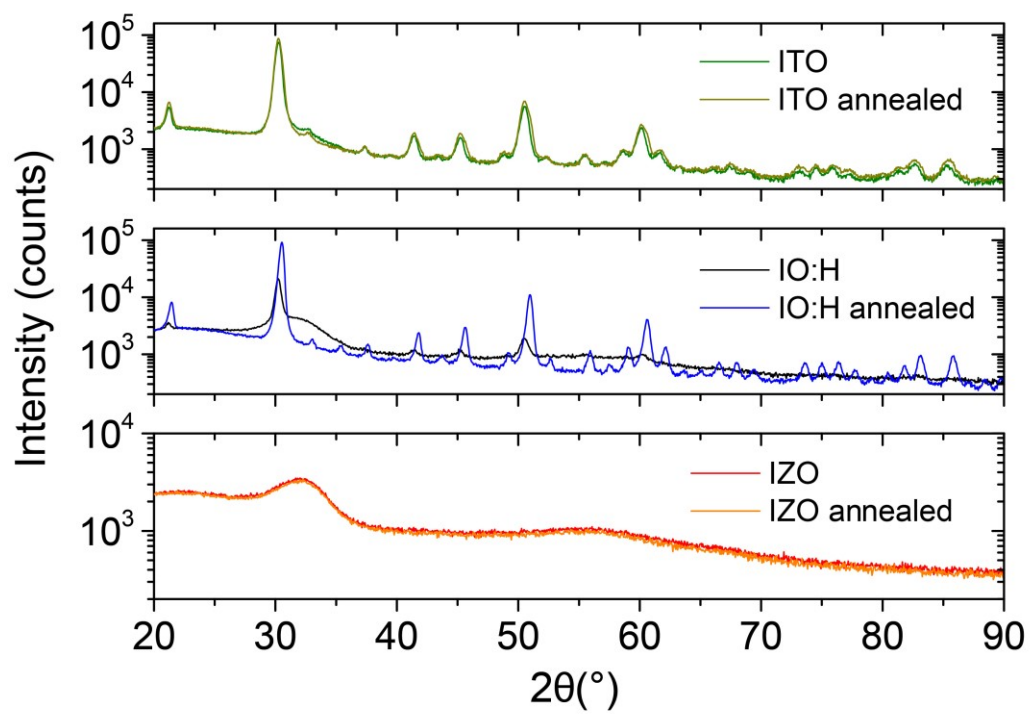| TCO	N $(10^{20}$ cm$^{-3})$	μ (cm^2/Vs)	ρ $(10^{-4}$ Ω cm)	σ $(\Omega^{-1}$ cm$^{-1})$	R_{sh} (Ω sq) d = 100 nm
ITO (as-dep)	0.5	47	24	414	240
ITO (annealed)	2.4	25	10	960	100
IO:H (as-dep)	3.8	54	3	3283	30
IO:H (annealed)	1.7	115	3.2	3128	32
IZO, r(O$_2$)=0.4% (as-dep)	2.1	58	5.1	1949	51
IZO, r(O$_2$)=0.4% (annealed)	2.3	60	4.5	2208	45

Fig. 6. GI-XRD data of the ITO, IO:H and *a*-IZO thin films as-deposited and annealed at 190 °C in air for 20 min.
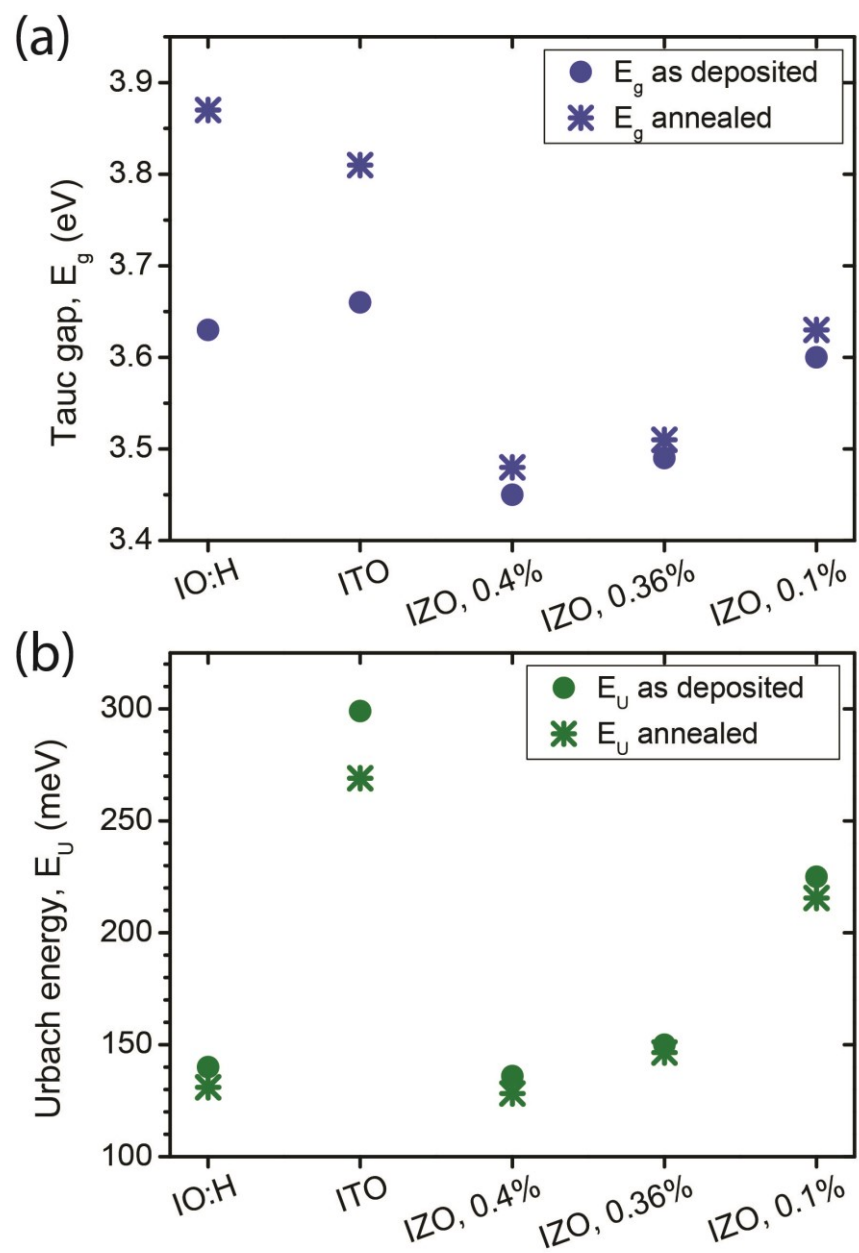
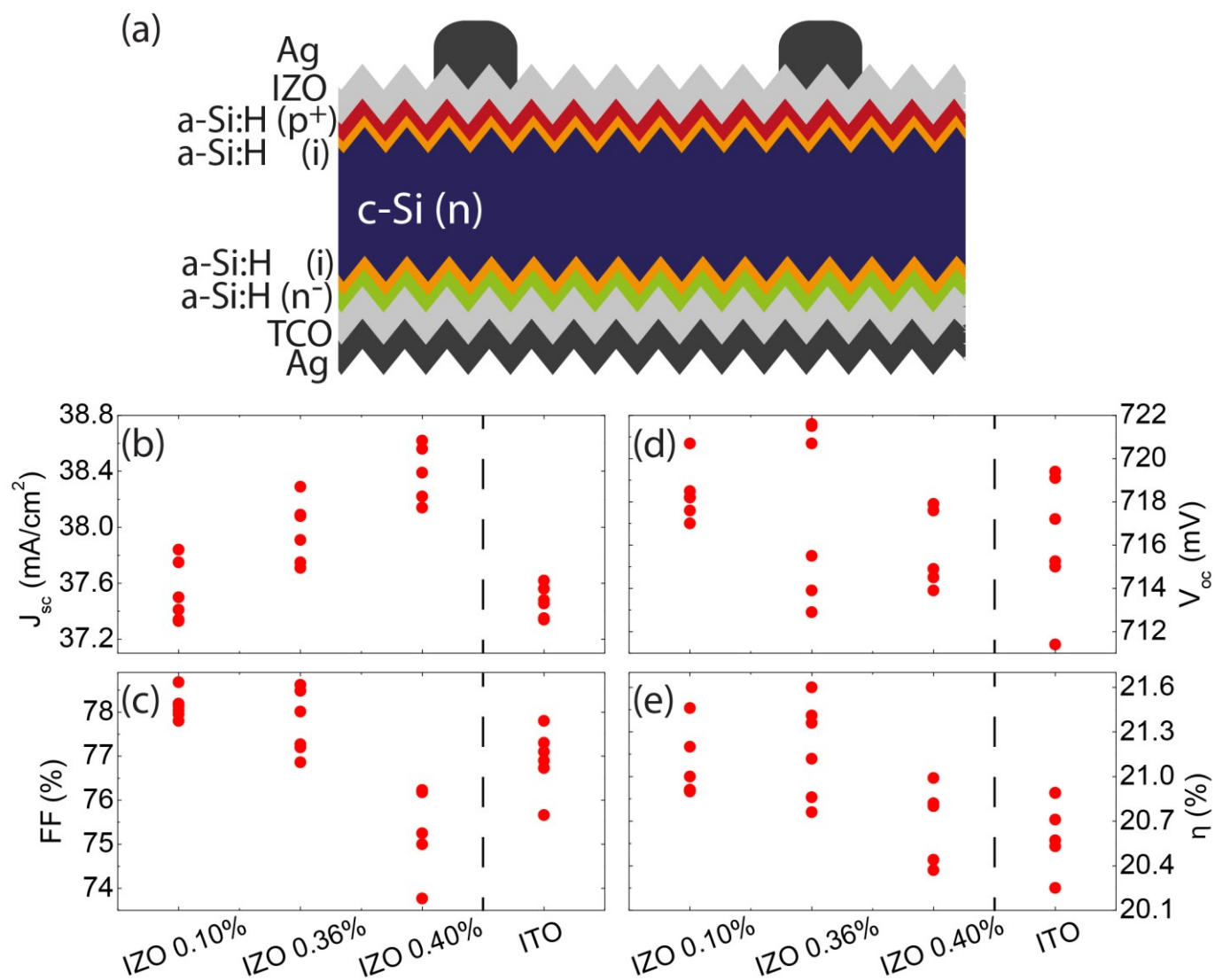Fig. 7. a) Tauc gap and b) Urbach energy of ITO, IO:H and *a*-IZO thin films.

Fig. 8. Output characteristics extracted from current-voltage measurements of 4 cm^2 solar cells with varying front TCO. (a) Short-circuit current density (J_{sc}), (b) open-circuit voltage (V_{oc}), (c) fill-factor (FF), and (d) conversion efficiency (η).